Universität Hamburg
DER FORSCHUNG | DER LEHRE | DER BILDUNG

High harmonic generation from solids with elliptically polarized laser pulses

Dissertation

zur Erlangung des Doktorgrades
an der Fakultät für Mathematik, Informatik und Naturwissenschaften
Fachbereich Physik
der Universität Hamburg

vorgelegt von

Nicolai Klemke

Hamburg
2020

Nicolai Klemke
Matrikelnummer: 6990014
Notkestraße 85, 22607 Hamburg

Gutachter der Dissertation:	Prof. Dr. Franz X. Kärtner *Universität Hamburg* Prof. Dr. Angel Rubio *Universität Hamburg*
Zusammensetzung der Prüfungskommission:	Prof. Dr. Franz X. Kärtner *Universität Hamburg* Prof. Dr. Angel Rubio *Universität Hamburg* Prof. Dr. Henry Chapman *Universität Hamburg* Prof. Dr. Nils Huse *Universität Hamburg* Prof. Dr. Daniela Pfannkuche *Universität Hamburg*
Vorsitzende der Prüfungskommission:	Prof. Dr. Daniela Pfannkuche *Universität Hamburg*
Datum der Disputation:	04.12.2020

Abstract

At the present day, high harmonic generation (HHG) from solids is an emerging field, rapidly maturing to a fundamental part of modern attosecond science. It promises wide-ranging applications, for instance as a compact solid-state source of ultrashort coherent extreme ultraviolet radiation, as a novel spectroscopic tool for the investigation of solids and as a cornerstone of petahertz optoelectronics. The precise dynamics underlying solid HHG are naturally complicated and so far no simple-mans model has been proven sufficient to describe the multitude of observed phenomena. One exciting aspect of solid HHG is its response to elliptically polarized excitation, which has been shown to behave very differently to what is known from HHG from gases. This thesis aims at exploring several facets of this, putting special emphasis on dissecting the polarization states of the emitted harmonics.

In experiments from Si, several key features are found for the first time. For instance, circularly polarized harmonics can be generated with circularly polarized laser pulses. Furthermore, with elliptical driving polarization, the harmonic ellipticities peak for certain driving conditions, enabling the generation of circular harmonics from elliptical laser pulses. Harmonic orders are shown to behave differently, demonstrating that different generation mechanisms can underlie different harmonics. The experiments are supported by an *ab-initio* time-dependent density functional theory framework (by N. Tancogne-Dejean, A. Rubio) which considers the full band structure and describes the experimental results convincingly.

To get further insights into the microscopic origin of some of the observed phenomena, a single-particle intraband-only model is developed and applied to a model-type tight-binding band structure as well as to the band structure of ZnS. In the latter case the results are also compared to experimental data. Several of the experimentally observed features can be reproduced in these simulations, e.g., sharply defined driving conditions that maximize the harmonic ellipticities with elliptical excitation, a rotation of the major axis of the harmonics as well as depolarization that increases with the peak electric field strength. By comparing simulations and experiments in ZnS, it is found that the intraband-only model provides a reasonable approximation for a below-band-gap harmonic but fails to describe a harmonic above the band gap, implying that there, the dynamics cannot be described sufficiently with a single band. Thus, the ellipticity response of solid HHG intrinsically carries information about its generation mechanism.

Finally, an extreme-ultraviolet beam line is set up in order to investigate high-order harmonics from MgO. These experiments confirm earlier results that the intensity of certain harmonics can be greatly enhanced with elliptical excitation. However in this case, and contrary to a previous theoretical prediction, the experiments do not show an extension of the cutoff with elliptical excitation.

The work described in this thesis can be expected to play a vital role in the further development of a microscopic understanding of the strong-field-driven charge dynamics in solids as well as in the construction of compact ultrafast circularly polarized HHG sources.

Zusammenfassung

Zum heutigen Zeitpunkt ist die Hohe Harmonische Erzeugung (HHG) von Festkörpern ein aufstrebendes Feld der ultraschnellen Optik und im Begriff, ein zentraler Bestandteil moderner Attosekundenphysik zu werden. Potenzielle Anwendungen reichen von der Nutzung als kompakter Quelle ultrakurzer kohärenter Pulse im extrem-ultravioletten Spektralbereich, über Nutzung als neues spektroskopisches Werkzeug zur Analyse von Festkörpern sowie als Bestandteil zukünftiger PHz-Optoelektronik. Verschiedene gekoppelte Dynamiken unterliegen der Erzeugung von HHG in Festkörpern und daher existiert bislang kein simples Modell, welches die vielfältigen, teils überraschenden Eigenschaften zuverlässig beschreibt. Dabei ist die Erzeugung Hoher Harmonischer mit elliptisch polarisierten Laserpulsen zu erwähnen, wo große Unterschiede zum bekannten Fall von HHG von Gasen aufgezeigt wurden. Diese Dissertation zielt darauf ab, dieses Verhalten und dabei speziell die Polarisationszustände der Harmonischen näher zu untersuchen.

In Experimenten an Si werden vielerlei Effekte zum ersten Mal gezeigt. Beispielsweise lassen sich zirkular polarisierte Harmonische mit zirkular polarisierten Laserpulsen erzeugen. Weiterhin gibt es auch Situationen, in denen mit elliptischer Laserpolarisation zirkular polarisierte Harmonische erzeugt werden. Es wird gezeigt, dass sich verschiedene Harmonische unterschiedlich verhalten, was als Beweis gelten kann, dass sie von verschiedenen Mechanismen erzeugt werden. Diese Experimente werden von Simulationen mittels *ab-initio* zeitabhängiger Dichtefunktionaltheorie unterstützt (N. Tancogne Dejean, A. Rubio), welche die gesamte Bandstruktur mit einbeziehen und die Experimente überzeugend beschreiben.

Um tiefere Einblicke in die Ladungsträgerdynamiken hinter diesen Beobachtungen zu gewinnen, wird ein einfaches Modell entwickelt, welches ein lasergetriebenes Elektron in einem Leitungsband beschreibt. Damit werden verschiedene Fälle simuliert und mit den Experimenten verglichen. Hierbei können entscheidene Beobachtungen reproduziert werden, beispielsweise die scharfdefinierten Laserparameter, für welche einzelne Harmonische zirkular polarisiert erzeugt werden. Auch eine Drehung der Hauptachse sowie Depolarisationsmechanismen werden von diesem einfachen Modell beschrieben und im Experiment gefunden. Für eine Harmonische oberhalb der Bandlücke stimmen die Simulationen nicht mit Experimenten überein, was verdeutlicht, dass hier noch andere Dynamiken relevant sind.

Zu guter Letzt wird ein Apparat aufgebaut, in dem sich Hohe Harmonische im extrem ultravioletten Spektralbereich erzeugen und detektieren lassen. An Experimenten von MgO können frühere Beobachtungen bestätigt werden, dass sich die Intensität von gewissen Harmonischen stark mit elliptisch polarisierten Laserpulsen vergrößern lässt. Eine theoretische Vorhersage, dass auch der Cutoff mit elliptischer Polarisation erhöht werden kann, wird nicht bestätigt.

Diese Arbeit leistet entscheidene Beiträge, um das mikroskopisches Verständnis der starkfeldgetriebenen Ladungsträgerdynamiken in Festkörpern weiterzuentwickeln und erlaubt die Konstruktion von kompakten HHG-Quellen mit beliebigen Polarisationszuständen.

Acknowledgements

I have had the chance to spend four delightful years at DESY in which I have not only learned a lot but have done so with the greatest sense of pleasure. This was in large part due to the amazing coworkers and colleagues I had and the following paragraphs should acknowledge their support and contribution.

First and foremost I would like to thank Prof. Dr. Franz Kärtner for his constant appreciation of my work, for some crucial ideas and for his trust in my decisions. I felt supported by one-hundred percent by Prof. Kärtner and I feel deep gratitude that he enabled me to have such an enjoyable and productive time at DESY.

I would also like to thank Dr. Oliver D. Mücke for bringing my attention to solid HHG and, especially in the beginning of the project, to support me with experimental ideas. Later on he let me follow my instincts freely which provided me with the freedom that led to the simulation part. I also learned some important lessons in problem solving from Dr. Mücke.

I am deeply grateful for the collaboration with Prof. Dr. Angel Rubio and Dr. Nicolas Tancogne-Dejean that helped a lot in providing fundamental insights into the ongoings of solid HHG. Prof. Dr. Rubio helped out when help was needed and fortunately is willing to act as a second reviewer to this thesis. Dr. Tancogne-Dejean offered many interpretations in cases where the experimental traces did not give a hundred percent certain answer and he supervised the simulation part of this thesis, with many critical questions and propositions for next steps.

On the daily work in the laboratory I am indebted to Dr. Giulio M. Rossi and Dr. Yudong Yang who introduced me to the laboratory, designed parts, helped to find quick and efficient solutions for a manifold of experimental problems. Dr. Rossi proposed to use his OPA for the experiments and I am very glad that I did. He also took care of the OPA- and the laser source whenever there were problems. At this point I would also like to thank Fabian Scheiba who made the spatiotemporal analysis of the 2DSI-trace possible, with whom it was a pleasure to work with and who also took care of maintaining the laser and numerous other things.

The close work with Giuseppe di Sciacca in the beginning of this project was a source of great happiness and of immense significance especially because he wrote the bulk of the experimental control software which was an important step towards the long-term measurements I got to do later on. I would also like to thank Dr. Haoyu Huang with whom working on the extreme ultraviolet beam line was a very productive time and with whom I enjoyed the philosophical coffee breaks.

Dr. Lu Wang has offered her brain capacities to support the simulation part whenever it was needed and the same is true for Miguel Angel Silva Toledo. Both of which were great discussion partners. Dr. Hüseyin Çankaya and Dr. Giovanni Cirmi also helped whenever help was needed, in all aspects of the day-to-day work.

I would also like to thank Felix Ritzkowski, Miguel Angel Silva Toledo, Fabian Scheiba, Dr. Giulio M. Rossi as well as my father for proof reading parts or - as in the latter case - even the complete thesis.

The engineering team, Andrej Berg and Thomas Tilp, provided quick and helpful engineering solution whenever they were needed. And last but not least I want to thank Christine Berber and Uta Freydank for taking care of the organizational work that is needed to keep the group running.

Overall I can say that many of my coworkers became good friends over the years and this feels like the greatest gift of these four years at DESY.

Contents

List of Abbreviations

2DSI	two-dimensional spectral shearing interferometry
BZ	Brillouin zone
CEP	carrier-envelope phase
CHCD	circularly polarized harmonics from circularly polarized driving pulses
CHED	circularly polarized harmonics from elliptically polarized driving pulses
CoM	center of mass
CPA	chirped pulse amplification
DoP	degree of polarization
FROG	Frequency-resolved optical gating
FWHM	full width at half maximum
HHG	high-harmonic generation
HHn	high-harmonic of order n
HWP	half-wave plate
JDOS	joint density of states
L(R)HCP	left(right)-handed circularly polarized
MCP	microchannel plate
OPA	optical parametric amplifier
QWP	quarter-wave plate
SNR	signal-to-noise ratio
TDDFT	time-dependent density-functional theory
WGP	wire-grid polarizer
XMCD	x-ray magnetic circular dichroism
XUV, EUV	extreme-ultraviolet

List of Publications

Peer-Reviewed Papers

[1] **N. Klemke**, N. Tancogne-Dejean, G. M. Rossi, Y. Yang, F. Scheiba, R. E. Mainz, G. Di Sciacca, A. Rubio, F. X. Kärtner, and O. D. Mücke, "Polarization-state-resolved high-harmonic spectroscopy of solids", Nature Communications 10, 1319 (2019).

[2] **N. Klemke**, N. Tancogne-Dejean, A. Rubio, F. X. Kärtner, and O. D. Mücke, "Role of intraband dynamics in the generation of circularly polarized high harmonics from solids", Physical Review B 10, 104308 (2020)

[3] M. Wagstaffe, L. Wenthaus, A. Dominguez-Castro, S. Chung, G. D. L. Semione, S. Palutke, G. Mercurio, S. Dziarzhytski, H. Redlin, **N. Klemke**, Y. Yang, T. Frauenheim, A. Dominguez, F. X. Kärtner, A. Rubio, W. Wurth, A. Stierle, and H. Noei, "Ultrafast Real-Time Dynamics of CO Oxidation over an Oxide Photocatalyst", ACS Catalysis 10, 13650 (2020)

International Conferences

[4] **N. Klemke**, G. Di Sciacca, Y. Yang, G. M. Rossi, R. E. Mainz, N. Tancogne-Dejean, A. Rubio, F. X. Kärtner, and O. D. Mücke, "Ellipticity dependence of higher-order harmonics in solids: unraveling the interplay between intraband and interband dynamics", Conference on Lasers and Electro-Optics, CLEO EU 2017, Munich, Germany, paper JTh5B.10

[5] **N. Klemke**, G. Di Sciacca, Y. Yang, G. M. Rossi, R. E. Mainz, N. Tancogne-Dejean, A. Rubio, F. X. Kärtner, and O. D. Mücke, "Circularly polarized high-order harmonics from solids driven by single-color infrared pulses", 6th International Conference on Attosecond Physics, ATTO 2017, Xi'an, China

[6] **N. Klemke**, G. Di Sciacca, Y. Yang, G. M. Rossi, R. E. Mainz, N. Tancogne-Dejean, A. Rubio, F. X. Kärtner, and O. D. Mücke, "Generation of circularly polarized high-order harmonics in solids driven by single-color infrared pulses", Frontiers in Optics 2017, Washington D.C., USA, paper JTu3A.18

[7] **N. Klemke**, N. Tancogne-Dejean, G. M. Rossi, Y. Yang, R. E. Mainz, G. Di Sciacca, E. Casandruc, A. Rubio, F. X. Kärtner, and O. D. Mücke, "Strong-field polarization-state control of higher harmonics generated in crystalline solids", Conference on Lasers and Electro-Optics, CLEO US 2018, San Jose, USA, paper FF3P.5

[8] H. Huang, L. Song, N. Tancogne-Dejean, **N. Klemke**, A. Rubio, F. X. Kärtner, and O. D. Mücke, "High-Order Harmonic Generation from Solids Dressed by an Intense Terahertz Field ", Conference on Lasers and Electro-Optics, CLEO US 2018, San Jose, USA, paper FM3F.3

[9] **N. Klemke**, N. Tancogne-Dejean, G. M. Rossi, Y. Yang, R. E. Mainz, G. Di Sciacca, A. Rubio, F. X. Kärtner, and O. D. Mücke, "Polarization states of high-harmonics generated in silicon from elliptical drivers", XXI Conference on Ultrafast Phenomena 2018, Hamburg, Germany

[10] H. Huang, L. Song, N. Tancogne-Dejean, **N. Klemke**, A. Rubio, F. X. Kärtner, and O. D. Mücke, "Ultrafast Control of Even-Order Harmonic Generation from Solids by an Intense Terahertz Field", 43rd International Conference on Infrared, Millimeter, and Terahertz Waves, IRMMW-THz 2018, Nagoya, Japan

[11] **N. Klemke**, N. Tancogne-Dejean, G. M. Rossi, Y. Yang, R. E. Mainz, A. Rubio, F. X. Kärtner, and O. D. Mücke, "Temporal coherence of linearly and circularly polarized high-harmonics from silicon", Conference on Lasers and Electro-Optics, CLEO US 2019, San Jose, USA, paper FF2C.2

[12] **N. Klemke**, N. Tancogne-Dejean, G. M. Rossi, Y. Yang, R. E. Mainz, A. Rubio, F. X. Kärtner, and O. D. Mücke, "Polarization-state-resolved high-harmonic spectroscopy on crystalline solids", 7th International Conference on Attosecond Physics, ATTO 2019, Szeged, Hungary

[13] **N. Klemke**, N. Tancogne-Dejean, A. Rubio, F. X. Kärtner, and O. D. Mücke, "Role of intraband dynamics on circularly polarized high-harmonic generation from solids", XXII Conference on Ultrafast Phenomena 2020, Shanghai, China (online)

Chapter 1

A brief introduction to high harmonic generation

Linear light-matter interactions have revealed themselves to mankind since its very beginning. With dispersion, reflection and absorption alone, one can describe almost our entire visual experience - a sense that most people would call paramount to their perception of the world. Even more so, from a quantum field theory perspective, photons are the force carriers of electromagnetic interactions. Hence even interaction of matter with itself seems to be mediated by light. This hardly leaves any directly observable phenomenon that is not at its core a light-matter interaction. Linear light-matter interactions are macroscopically characterized by an intensity-independent refractive index, i.e. the field-induced polarization in matter is linear to the amplitude of the light field. 60 years ago, this was found to not always be the case.

Only one year after the invention of the laser, Franken *et al.* famously reported that they doubled the frequency of laser light by focussing it on a quartz crystal [1]. Almost simultaneously, Kaiser *et al.* reported the observation of two-photon absorption in doped CaF_2 [2]. Both of these effects were immediately understood as observations of a second-order nonlinear effect, made available by the large photon flux of the newly invented laser [1–4]. Since then, the rapid development of perturbative nonlinear optics has led to countless applications in fields like consumer electronics, communication and medicine [5] and has revolutionized the fields of spectroscopy [6] and microscopy [7, 8].

The invention of chirped pulse amplification (CPA) by Strickland and Mourou in 1985 [9] (Nobel prize 2018) enabled the amplification of laser pulses with femtosecond pulse durations ($1\,\mathrm{fs} = 10^{-15}\,\mathrm{s}$) to the mJ-level. This had tremendous consequences on the feasible peak powers of laser pulses. If compressed to a short enough time, already μJ's of energy can easily produce high enough electric field strengths to rival the intraatomic electric field. Nowadays, the highest possible electric field strengths can be generated with ultrashort lasers. They are anticipated for approaches to overcome the proton-proton repulsion for nuclear fusion [10] and to reach the Schwinger limit, at which the electric field is strong enough to separate spontaneously generated electron-hole pairs and thereby break down the quantum

vacuum [11].

Shortly after the invention of CPA, it was reported that high-order harmonics could be generated when strong laser pulses were focussed on gas atoms [12–14]. The conventional theory of perturbative optical harmonic generation was not sufficient to explain how an infrared laser pulse could generate the observed plateau-like spectrum of high-order harmonics up into the extreme ultraviolet (XUV) region of the electromagnetic spectrum. However, a comprehensive theory was developed within seven years of its first observation. It involved tunnel ionization (theoretically developed by Keldysh already in 1965 [15]), subsequent acceleration of the partly freed electron wave packet and due to the polarity change of the laser field, interference with the wave packets unionized portion in its parent ion [16,17]. High harmonic generation (HHG) from gases has since then matured to a substantial part of ultrafast optics. With HHG, the shortest light pulses (or the shortest events at all for that matter) ever have been created [18], as well as photon energies up to 1.6 keV [19]. This makes HHG an ideal source to study dynamics on the natural timescales of electrons [20–24].

It was early observed and understood that elliptically polarized driving pulses diminish the high-harmonic yield because the freed electron does not find its way back to its parent ion with an electric-field vector that is changing directions in time [16,25–28]. As a consequence, circularly polarized high-harmonic pulses cannot be produced from atoms with a single circularly polarized driving field. However, rather elaborate schemes have recently attracted a lot of attention in generating circularly polarized HHG nevertheless. These included counter-rotating circularly polarized bi-color pulses [29–31], non-collinear counter-rotating circularly polarized pulses [32] or the combination of two orthogonally polarized HHG beams with an appropriate phase shift [33]. In general, circularly polarized, ultrashort XUV-sources are a promising tool to investigate chiral systems [34, 35] and magnetic materials [36,37].

In 2011, Ghimire *et al* demonstrated the first non-perturbative HHG from a solid material, the crystal ZnO [38]. This work has sparked significant interest in the scientific community. The manifold of different solid materials represent a large playground of opportunities for such a new field. For instance, much lower intensities are needed when compared to gas HHG, which could lead to extremely compact solid-state attosecond sources. Another interesting aspect is that solid HHG itself could serve as a spectroscopic tool. For instance, it has been proposed that the band structure of a solid can be reconstructed from it [39, 40]. Also, it contains signatures of the dynamics in interesting materials like topological insulators [41], strongly correlated materials [42,43] or epsilon-near-zero materials [44]. The precise strong-field dynamics underlying HHG from solids are naturally complicated and subject to an intense scientific debate of which no complete picture has yet emerged.

In 2017, it was reported that the response of harmonic 19 (HH19) to driving-laser ellipticity was vastly different than in the gas HHG case [45]. The yield was not zero with circular excitation and for certain crystal rotations it was found that the yield could actually be maximized with elliptically polarized excitation. Similar

observations have then been made from harmonics in the visible wavelength range from Graphene and MoS_2 [46]. Here, Yoshikawa and coworkers have also looked at the polarization of the harmonics and found that in some cases, the polarization angle could be rotated to the driving axis [46]. Tancogne-Dejean and coworkers have modeled this behavior with an *ab-initio* time dependent density functional theory approach (TDDFT) and were able to reproduce the results from MgO and predicted, among other things, that circularly polarized high-harmonic could be generated from solids with circularly polarized driving fields. Also, for elliptical polarization, Tancogne-Dejean *et al.* predicted that the harmonics polarization could deviate from the polarization of the driving pulses. Furthermore, under certain conditions in MgO, the cutoff could be enhanced with elliptically polarized excitation. All of this is far from intuitive when used to the gas HHG dynamics. Even more so, since the precise ultrafast carrier dynamics in solids that underlie solid HHG are not well understood, the high-harmonic response to elliptically polarized excitation could link to some fundamental insights on the one hand and some fascinating applications on the other. The aim of the present project is to explore this behavior in more detail than has been done so far.

This thesis is organized as follows. This chapter introduces gas HHG and discusses its response to elliptical excitation as well as review the methods to generate circularly polarized high-harmonics from gases. Then, we shall review the most important findings of solid HHG to date and discuss some general aspects and challenges of its description. Also, a review on what has been done with elliptical and circular polarization so far will be given. Chapter 2 presents experimental work that mostly revolves around HHG from silicon in which harmonics between 200 nm and 700 nm will be studied. Here, two methods of generating circularly polarized HHG from solids will be presented as they have been found in these experiments for the first time. To better understand the observed phenomena, chapter 3 presents results on single-particle intraband-only calculations which, for the first time, have been applied to solid HHG with elliptically polarized excitation. Some ideas will be developed, as to how the polarization states of the harmonics can deviate so strongly from those of the driving pulses. In chapter 4, this work is extended to the extreme ultraviolet spectral region and it is investigated how high-harmonics generated from MgO respond to elliptically polarized excitation. The conclusions will be drawn in chapter 5.

1.1 High harmonic generation from gases

Even the longest journey begins with a single step - as Lao Tzu has been ascribed to have said - and so, let us start by examining the relevant fundamentals to this work. High-harmonic generation in gases has matured to a reliable source of coherent XUV-pulses that is nowadays implemented in dozens of laboratories worldwide. The generation mechanism is quite well understood and has been described comprehensibly in well received sources. It might seem odd to discuss HHG from gases here since the project that culminates in this thesis revolves

around HHG from solids. However, since HHG from solids is far less understood than its gas counterpart and since there are significant similarities between the two, it makes sense to discuss relevant phenomena in gases first. A central aspect of this thesis is the generation of circularly polarized high harmonics and thus, it is particularly useful to review existing approaches that achieve the same from gases. This should help to discuss similarities and differences as well as possible advantages and disadvantages of the here provided findings. This chapter will take some knowledge about perturbative nonlinear optics and the generation and methodology of ultrashort laser pulses for granted. If interested, the reader is advised to look up standard literature on this topic. For nonlinear optics this could be, e.g., Refs. [47, 48] and for ultrafast optics, e.g., Refs. [49, 50].

1.1.1 Fundamentals

The elementary features of HHG are captured by its unique spectrum. While for perturbative harmonic generation, higher orders than the 5^{th} harmonic are seldom observed, the typical HHG spectrum exhibits dozens to hundreds of odd* harmonic orders. While for perturbative harmonic generation, the harmonic yields, i.e. the intensities of the harmonics, decrease exponentially with increasing harmonic order, this is only the case for the first few harmonics in an HHG spectrum. Most of the harmonics of an HHG spectrum lie in the 'plateau'-regime, in which the harmonic signal varies only very little for different harmonic order. The highest harmonics can be found in the 'cutoff'-regime, in which the harmonic yield decreases exponentially again (see Fig. 1.1**a**).

The HHG process can be described with a three-step model, either semiclassically [16] or with a full quantum-mechanical description [17] (see also Fig. 1.1**b**). The three steps are:

1. **Tunneling** The electric field strength of the laser pulse is strong enough to rival the intra-atomic electric field. That means it distorts the atomic potential, opening up a window for the bound electrons to tunnel out [15].

2. **Acceleration** This is where the classical part of the semiclassical description begins. A free electron is born at the position of the atom and accelerated away from its parent ion. Upon polarity change of the electric field, it is accelerated back towards its parent ion. Its precise trajectory depends on the time of ionization and naturally on the laser parameters. In the quantum description, an electron wave packet is accelerated by the laser field and its expectation value coincides with the classical description. Additionally, it undergoes quantum diffusion which heavily depends on the time spent in the continuum.

*This is for the typical case of a multi-cycle pulse irradiating rare-gas atoms. For single-cycle or sub-cycle pulses, the spectrum does not show distinct harmonic orders. With non-inversion-symmetric molecules instead of rare-gas atoms, the spectrum can also contain even harmonic orders. But these cases have so far been the exception in the literature and therefore they shall be treated as such here as well.

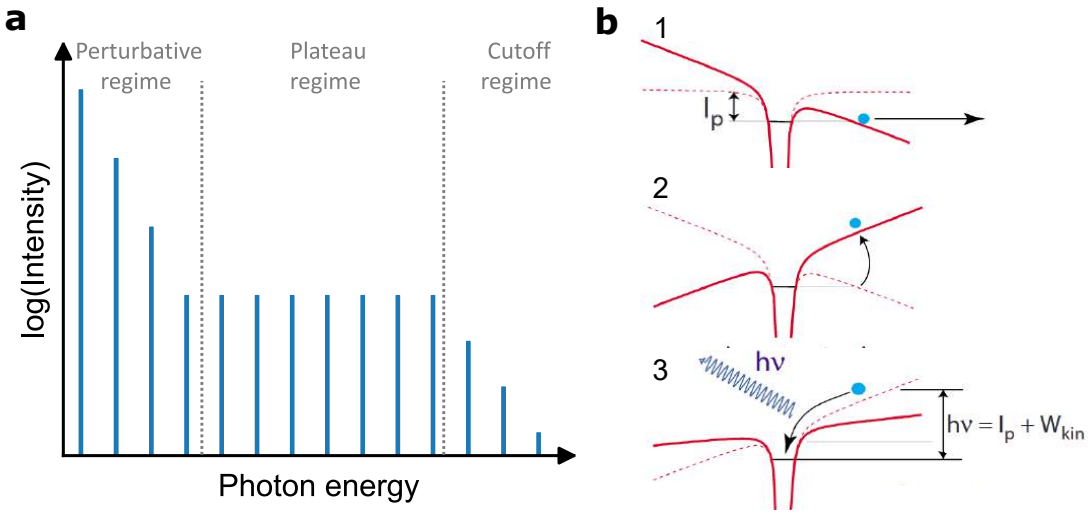

Figure 1.1: **a**: A schematic gas HHG spectrum. **b**: Visualization of the three-step model with (1) ionization, (2) acceleration and (3) recombination. I_p is the ionization potential and W_{kin} the kinetic energy of the free electron (adapted from [51])

3. **Recombination** If the trajectory of the electron crosses its parent ion, there is the chance for the electron to recombine with it. Hereby it emits its final kinetic energy plus the ionization potential of the atom. A key difference lies in the quantum mechanical description where the light-emitting process is a result of interference of the continuum wave packet with its bound portion that did not tunnel out. This interference causes dipole oscillations with the frequency of the energy difference of the two wave packets divided by Plancks constant. These dipole oscillations emit photons. The quantum diffusion that acted on the continuum wave packet significantly decreases the strength of the oscillating dipole.

For multi-cycle laser pulses, XUV-bursts are emitted every half-cycle. Fourier-transforming such a temporal signal leads to the eponymous spectrum containing only odd-order harmonics of the driving frequency. Because high harmonics are only emitted when electrons and parent ions recollide - and because this is only the case for a short range of ionization times - the individual XUV-bursts are significantly shorter than a laser period. To make use of the temporal resolution that is determined by these short burst durations, one needs to isolate a single attosecond burst out of the pulse train. Over the last two decades, several methods have been developed to gate the HHG process accordingly (one will be mentioned in the next section). The shortest pulse duration achieved with HHG to date is 43 attoseconds [18]. This is the shortest controlled event that mankind has created thus far. HHG-based attosecond pulses are inherently synchronized to the driving laser pulses, which enables pump-probe experiments with unprecedented temporal precision (see for instance Refs. [52, 53]).

The plateau has its origin in two contributions: Uncertainty in the precise timing of ionization as well as quantum diffusion that smears out the energy of the free-electron wave packet at the moment of 'recollision'. This equalizes the effect of different ionization probabilities at slightly different phases of the laser pulse. Plateau harmonics do vary in relative strength but their variation is minor when plotted on a logarithmic scale. The other characteristic spectral feature of HHG - the cutoff - can be determined both with the semiclassical and the quantum-mechanical model. It turns out to be

$$E_{max} = I_p + 3.17U_p, \tag{1.1}$$

where I_p is the ionization potential of the atom and U_p is the ponderomotive potential, also called the 'quiver' energy of the electron. U_p is proportional to λ^2 (λ is the laser wavelength) as well as to the driving intensity I. A lot of effort has been put in increasing U_p by driving HHG with longer wavelengths [19, 54, 55], however, the HHG efficiency scales with λ^{-5} to λ^{-6} [56, 57]. Novel approaches are trying to circumvent this limitation with ultrabroadband sculptured sub-cycle pulses [58].

In the quantum mechanical picture, the electron interferes with itself. This is not only interesting as a source for ultrashort highly energetic radiation but also as a spectroscopic tool to gain insight about the gas medium itself. For instance, in Refs. [20, 59], HHG has been proposed as a tool to tomographically reconstruct the atomic or molecular orbitals.

So far, we have only discussed the single-atom response. When looking at HHG as a macroscopic phenomenon with laser-gas interaction lengths of a few mm to cm it becomes crucial to match the group velocity of the fundamental frequency and the desired harmonic order. This is - in parts - possible by carefully counterbalancing different physical parameters, for instance the refractive index (e.g. due to free electron dispersion) or the driving laser phase (e.g. due to Gouy phase shift) but it is a tough business and by definition not possible for all frequencies simultaneously. Typical conversion efficiencies for high-harmonic sources lie in the range of 10^{-9} to 10^{-6} per harmonic order, depending on the desired wavelength range and therefore the gas medium.

1.1.2 Elliptical polarization

One possible validation of the trajectory-picture of the three-step model lies in modification of this trajectory and confirming if the outcome overlaps with predicted results. The easiest way to do so is by inserting a quarter-wave plate (QWP) into the beam which enables adjusting the driving laser to elliptical or even circular polarization. Since the field itself drives the trajectories of the free electrons, elliptical excitation can be expected to have a major impact. To show this, we can investigate the classical acceleration step of the three-step model under the

influence of the laser field. The laser field $\mathbf{E}_L$ is polarized in the x-y-plane

$$\mathbf{E}_L(t) = \frac{\tilde{E}}{\sqrt{1+\epsilon^2}} \begin{pmatrix} \cos(\omega t) \\ \epsilon \sin(\omega t) \end{pmatrix}. \tag{1.2}$$

$\tilde{E}$ is the field amplitude and ω the angular driving frequency. For simplicity we ignore any time dependence of $\tilde{E}$, but the same analysis is valid if $\tilde{E}$ is time dependent. The ellipticity $\epsilon = E_y/E_x$[†] is defined in the range $0 < \epsilon < 1$, with 0 representing linear and 1 defining circular polarization. Next, we can just calculate the classical trajectory of the electron and study under which conditions it comes back to its origin. The classical equation of motion for the free electron is

$$\frac{\mathrm{d}^2\mathbf{r}(t)}{\mathrm{d}t} = -\frac{e\mathbf{E}_L(t)}{m_e} = -\frac{e\tilde{E}}{m_e\sqrt{1+\epsilon^2}} \begin{pmatrix} \cos(\omega t) \\ \epsilon \sin(\omega t) \end{pmatrix}, \tag{1.3}$$

where e and m_e are the electron charge and mass and $\mathbf{r}$ the excursion of the electron from its parent ion. Equation 1.3 can be integrated such that the velocity reads

$$\mathbf{v}(t) = \frac{e\tilde{E}}{m_e\omega\sqrt{1+\epsilon^2}} \begin{pmatrix} -\sin(\omega t) + \sin(\omega t_i) \\ \epsilon\cos(\omega t) - \epsilon\cos(\omega t_i) \end{pmatrix}, \tag{1.4}$$

t_i is the time of ionization. And then, after one more integration, we finally reach the time-dependent excursion of the free electron to its parent ion

$$\mathbf{r}(t) = \frac{e\tilde{E}}{m_e\omega^2\sqrt{1+\epsilon^2}} \begin{pmatrix} \cos(\omega t) - \cos(\omega t_i) + \omega(t-t_i)\sin(\omega t_i) \\ \epsilon\left[\sin(\omega t) - \sin(\omega t_i)\right] - \omega\epsilon(t-t_i)\cos(\omega t_i) \end{pmatrix}. \tag{1.5}$$

Due to the heavy mass of the ion, one typically assumes that it does not move, i.e. that it remains at $x = y = 0$. From Eq. 1.4 one can calculate t_i for which the electron acquires the highest velocity at recollision, which results in the cutoff law described by Eq. 1.1. The point of this section however, is to explore what the three-step model implies for elliptical polarization. Since Eq. 1.5 allows basically two knobs to turn, t_i and ϵ, Fig. 1.2 visualizes different trajectories for variation of these two cases. According to our definition of the laser field, the major axis is always polarized along the x-direction and any perpendicular component due to ϵ points to the y-direction.

Fig. 1.2**a** depicts trajectories for different ϵ ranging from linear ($\epsilon = 0$) to circular ($\epsilon = 1$) driving pulse polarization. Here, the ionization time is $t_i = 0.1\,\mathrm{fs}$ after the peak of the electric field. $\epsilon = 0$ is the typical HHG case: the electron gets accelerated away from its parent ion at $x = y = 0$ and once the polarity of the electric field changes sign, it gets accelerated towards its parent ion again. Finally, after some travel time it reaches $x = y = 0$, which is the moment of recollision that is often referred to as return time t_r. The velocity that the electron has at

[†]In later sections, a slightly more general definition for ϵ will be used.

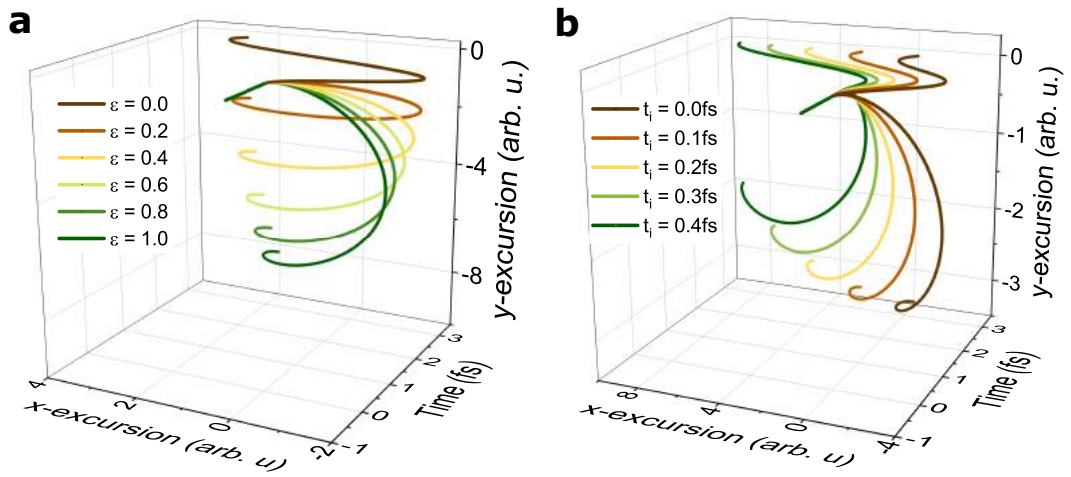

Figure 1.2: Trajectory visualizations of the three-step model with elliptically polarized laser pulses of 800 nm (period 2.7 fs). **a**: Comparison of trajectories for different ellipticities with $t_i = 0.1$ fs. **b**: Comparison of trajectories with linear polarization along x-component, $\epsilon = 0$ (curves with no y-excursion), and elliptical polarization with $\epsilon = 0.3$ (respective curves with y-excursion) for different ionization times t_i with respect to the peak of the field. Note the different units on x- and y-excursion in both **a** and **b**. The parent ion is not depicted and remains at $x = y = 0$ (but propagates linearly on the time axis).

t_r depends on the driving intensity, wavelength and t_i. Since Eq. 1.5 contains no recollision, the trajectory in Fig. 1.2**a** extends further into the negative x direction. Obviously, the electrons we are interested in do recollide, therefore this region does not matter in the discussion here.

For non-zero driving ellipticities, the electrons acquire momentum in the y-direction. As it can be seen from Eq. 1.2, x and y-components are oscillating with a 90°-phase shift between each other. This implies that x and y-components have different times at which they become zero and it is not possible to find a driving condition with $\epsilon > 0$ for which electron and parent ion recombine.

The same is true for variation of the ionization time t_i, see. Fig. 1.2**b**. Here, some t_i are plotted both for linear and for elliptical ($\epsilon = 0.3$) polarization. Note that the t_i are chosen in such a way that they all lead to recollision with linear polarization. Different t_i do alter the excursion of the electron as well as their total kinetic energy. But once again, for elliptical excitation it is not possible to find a t_i for which x- and y-component equal zero at the same time. The semiclassical three-step model therefore implies that there is no high-harmonic emission for $\epsilon \neq 0$.

In Ref. [26] it is argued, that for a typical peak intensity of 5×10^{14} $\frac{\mathrm{W}}{\mathrm{cm}^2}$ with a Ti:Sapphire laser, already $\epsilon = 0.01$ is sufficient to displace the electron by more than one atomic dimension in y-direction, circumventing recollision. Although in experimental data, the harmonic yield does decrease very rapidly with increasing ϵ, harmonics can usually still be observed for $\epsilon \approx 0.3$ with 800 nm and the usual peak

intensities[‡]. Consequently, the simple semiclassical model described by Eq. 1.3 is lacking some accuracy in that regard. In ref. [26] it is argued, that one can assume the ionized electron to have some initial transverse momentum which counteracts the y-component of the elliptically polarized laser field. The measured harmonic yields versus ϵ are then interpreted as direct measurements of this initial transverse momentum [26]. In the full quantum mechanical description of Lewenstein *et al.*, in which the ionized electron is not a well localized particle but an extended wave function, the interpretation of the ellipticity dependence follows more natural. The fact that the harmonic yield does not diminish fully with small ϵ is a direct consequence of the spatial 'extent of the wave packet and quantum diffusion' [28, 60]. In any case, the Lewenstein model also predicts the harmonic yield to decrease rapidly with increasing ϵ [28, 60].

Here, one can see a good exhibition of the typical interpretation pathway in the field of gas HHG. A simple semiclassical model exists that can predict a general trend quite accurately and also gives an intuitive explanation. If one then takes into account the whole quantum model one can often quickly resolve the remaining open questions without taking too much of a conceptual leap. Throughout this thesis, the monotonically decreasing yield with increasing ϵ will be called an 'atomic-like' behavior.

If one wants to utilize the attosecond time resolution of the HHG-emission for further experiments, one typically wants to isolate a single HHG burst in time. Therefore, several gating mechanisms exist. A very popular method exploits the behavior of gas HHG with elliptical polarization. If one wants to generate an isolated attosecond pulse from few-cycle driving pulses, then one can split the pulse into two replicas, converting the first one to LHCP and the second one to RHCP (or vice versa). As argued above, both pulses individually will not generate any harmonics. However if they are overlapped in time, the two circular waves compensate each other to an effectively linearly polarized field for a short amount of time. If one sets conditions just right, it is thus possible to generate an isolated attosecond pulse. This approach is called 'polarization gating' [61].

1.1.3 The polarization of high harmonics from gases

After the ellipticity dependence of gas HHG was first demonstrated, it did not take long for researchers to try to investigate the polarization of those harmonics. Experimentally this is challenging, in particular because in the XUV there are no transmissive optics that can perform this task. The usual workaround utilizes the difference in the p- and s-reflectivity components of metallic mirrors under grazing incidence. By using multiple reflections one can achieve a reasonable contrast for the different polarization components [62, 63]. Since gas HHG is usually performed from noble gas atoms and those are isotropic, the results should not depend on the rotation of the driving field. Therefore, one can get away experimentally with

[‡]Sometimes also with higher ϵ depending on the driving conditions and the detection sensitivity

rotating the driving field with a half-wave plate instead of rotating the mirror assembly that functions as a polarizer. These kind of experiments have been done first in 1995 by Weihe *et al.* [64] in which they discovered that the harmonics' major axis rotates with increasing driving ellipticity ϵ. A rotation of up to 45° was observed for $\epsilon \approx 0.4$. In Ref. [28], Antoine and coworkers extended these experiments for different noble gases and for higher harmonics. They confirmed that the harmonics' major axis rotates with increasing ϵ.

In a recollision-type picture it might seem intuitive that the harmonics' polarization axis rotates with driving ellipticity because the angle at which electrons and parent ions recombine changes. This angle is dependent on the ionization time and hence on the photon energy of the harmonic order. This simple discussion shows how crucial these experiments were to understand and visualize the generation mechanism of gas HHG. Ref. [28] also looked at the ellipticity of the harmonics. In fact, they were only able to give an *upper limit* on the ellipticity because a true ellipticity measurement requires also to measure the circular component of the light. This is closely related to the degree of polarization (see Sec. 2.3.3) and its measurement is challenging in the XUV, to say the least [65]. In any case, by observing the upper limit and comparing with simulations, they found that the harmonics' in fact get elliptically polarized with increasing ϵ. For extreme cases in neon, the upper limit of the ellipticity of harmonic 23 (HH23) was reported to be 0.8 for a fundamental ellipticity $\epsilon = 0.3$. The quantum model utilized in that same paper was able to reproduce results quite accurately although it did not cover this large ellipticity in neon. They argued that macroscopically, the driving pulses polarization varies in space over the spatial profile, which has a depolarizing effect on the harmonics [28].

The origin of the ellipticity observed for harmonics when driving with elliptical fields can be understood in the quantum mechanical picture of HHG. The spatial extension of the wave packet due to the uncertainty of the transverse initial electron momentum and the subsequent acceleration in y-direction due to the elliptically polarized field leads to an asymmetric probability amplitude of the wave packet in y-direction. The oscillating dipole of the wave packet's interference then also exhibits a y-component with $\pi/2$ phase shift. This is elaborated on in detail in Refs. [66, 67].

Atoms exhibit spherical symmetry and in a sense, all results presented so far, can be viewed as consequences from that. With aligned diatomic molecules, it has been shown that the polarization major axis can strongly rotate and is correlated to the symmetry axis of the molecules [68, 69]. Moreover, it can differentiate between σ_g and π_g symmetries of CO_2 and N_2 [68]. In Ref. [69] it was also found that the harmonics were elliptically polarized when the laser was not aligned to the symmetry axes of the molecules. Another interesting effect resulting from the orbital structure of molecules is an asymmetric harmonic response for positive and negative ellipticities, i.e. the handedness of elliptically polarized driving fields. This was found, for instance, in CO_2 [70] and was later exploited to probe molecular chirality in two enantiomers [71]. In the future, this could become a unique spectroscopic tool enabling experiments on the chirality of molecules on sub-cycle

timescales.

1.1.4 A review on methods to generate circularly polarized high harmonics from atomic gases

HHG offers unique capabilities to explore electron dynamics on their natural timescales and no other tabletop method can provide that to date. In fact, even state-of-the-art free electron lasers (FELs) cannot provide the timing accuracy that HHG sources can offer [72–74] although work is being done to change that [75].

For a variety of research, circularly polarized XUV or soft x-ray pulses are crucial. This is true for the spectroscopy of chiral matter [34] but even more so for the study of ultrafast nanoscale magnetization dynamics. A list from 2013 counted 55 synchrotron beamlines worldwide with x-ray magnetic circular dichroism (XMCD) capabilities [76]. While synchrotrons produce extremely brilliant hard x-ray radiation they cannot provide good time resolution. Spin dynamics that are responsible for the formation of magnetic domains can therefore not be studied. Ref. [77] even puts the development of XMCD-setups with subpicosecond temporal resolution as one of the main goal of magnetization physics, as of 2010. This is not referring to HHG methods but HHG sources can reach the necessary photon energies and if they could do so with circular polarization this would open a completely new window to investigate the ultrafast dynamics of magnetization.

Approaches to achieve high harmonics from gases with circular polarization can be grouped in two classes. One way is to generate harmonics in the conventional way with linearly polarized laser pulses and then manipulate the high-harmonic pulses afterwards. The other way is to manipulate the laser pulses in such a way that high-harmonic pulses are generated circularly polarized right away. Let us take a moment to discuss the two and what has been done with them so far.

Converting a linearly polarized harmonic pulse train to a circular one can be done, for instance, by utilizing the phase shift introduced between p- and s-component upon reflection on a mirror. This phase shift depends on the material, the wavelength and the incidence angle. Ref. [78] demonstrated a setup consisting of four reflections on a molybdenum mirror (see Fig. 1.3**a**). The reflection angles were optimized such that p- and s-components experienced approximately the same reflectivities (anything else would cause the resulting wave to be elliptically polarized). A degree of circular polarization of almost 100% could be achieved. Due to the relatively low reflectivities of each mirror, the total efficiency of the 'circular polarizer' was in the range of a few percent [78], which is also the main drawback of this method. HHG intrinsically suffers from a low generation efficiency and losing two additional orders of magnitude of flux converts one hour integration time into hundred hours of integration time which can prohibit experiments altogether. A more efficient approach is to coherently combine two linearly polarized HHG pulses with orthogonal polarization. This has very recently been achieved [33] by generating high harmonics in one gas jet and then reflecting the infrared and the HHG beam from a two segment mirror, which center can be moved to introduce

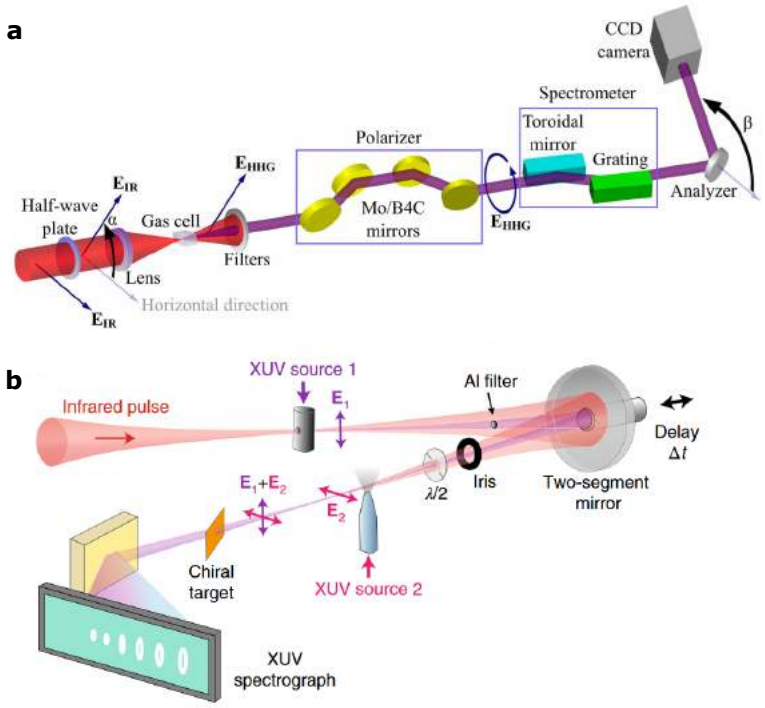

Figure 1.3: Two methods to convert linearly polarized high-harmonic pulses into circularly polarized ones. **a** from Ref. [78], **b** from Ref. [33]

a delay between HHG and infrared pulse (see Fig. 1.3**b**). Then, the two beams pass through a HWP that has a small drilled hole in the center to pass through the HHG beam unperturbed. Therefore the HWP only acts on the infrared pulse, rotating its polarization axis by 90°. This beam then generates high harmonics in a second gas cell. With careful stabilization, the two high-harmonic pulses are phase locked and the polarization state of the combined high-harmonic pulse can be controlled with the delay on the two segment mirror [33]. This approach seems very challenging to implement and to stabilize but apart from that does not have any obvious fundamental limitations. Both of the discussed approaches are wavelength selective, i.e. they do not permit to circularize a broad bandwidth of harmonics at the same time.

The second class of methods to generate circularly polarized high harmonics is to manipulate the driving laser pulses in such a way that circularly polarized harmonics can be generated directly. So far, this has been demonstrated with two techniques. One relies on generation with bichromatic, bicircular fields and the other one utilizes non-collinear bicircular fields. Let us first discuss the bicolor, bicircular field approach.

These type of fields can be generated by frequency doubling the driving laser pulses partly and then converting both the second harmonic and the remaining fundamental to circularly polarized pulses with opposite helicities (Fig. 1.4**a**). The resulting total waveform of these bicircular fields is a propeller-shaped Lissajous

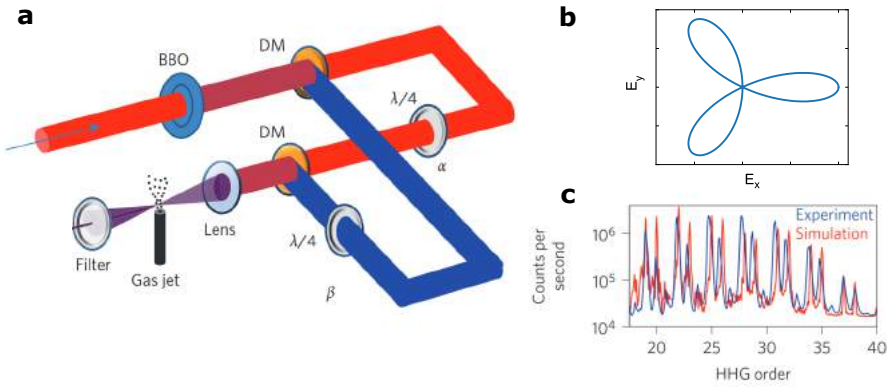

Figure 1.4: **a** Experimental setup for bicolor, bicircular generation of circularly polarized high harmonics. **b** shows a typical Lissajous-curve produced by such a setup. **c** exemplary high-harmonic spectrum, showing suppression of every third harmonic. **a** adapted from Ref. [30], **c** adapted from Ref. [31]

curve (Fig. 1.4). This field consists of three identical regions that resemble elliptical polarization. However, each of the three ellipses exhibit rather low ellipticities. This means that field-driven electrons in the HHG process do not acquire a large amount of perpendicular momentum, thereby keeping the HHG yield at a reasonable level. Recollisions happen three times per laser cycle and the XUV-emission of consecutive recollision events are 120° rotated from another (this is due to the propeller shape of Fig. 1.4**b**). The fact that recollisions happen three times per laser cycle is manifested in the frequency spectrum in such a way, that two consecutive harmonic orders appear, while every third harmonic order is suppressed (Fig. 1.4**c**). The consecutive harmonics are circularly polarized with alternating helicities. Note that because the symmetry of the field is different than in the usual case, odd and even high-harmonic orders can be produced.

This approach has been pioneered already in 1995 [29] however without having measured the harmonics' polarization. Theoretical work has explored this approach further [79] until over the past years this method has gained significant momentum especially due to work from the group of O. Cohen, who have characterized the polarization states [30] (but not the degree of polarization) and increased the brightness to a comparable level with linearly polarized generation [31]. Furthermore, they performed first magnetic circular dichroism measurements on M-shell edges of Co [31] and on nanoscale magnetic domains of a Co/Pd multilayer structure [36]. So far, these experiments have not been time resolved but there is no reason why they should not be. As mentioned in the introduction of this section, time-resolved experiments with circular HHG sources would open a window into completely new physics: Magnetism on the few femto- or even attosecond timescale.

Of course the ω-2ω-field of Fig. 1.4 is only an example. The same type of approach has been followed with two fields consisting of 1.3 μm and 0.79 μm which end up in an eightfold rosetta-shaped field, generating in that case harmonics up

to 160 eV [37] reaching closer and closer to important L-edges. Further increasing the wavelength to increase the harmonic cutoff [19] seems to not contradict this HHG approach at all. However, it should be mentioned, that recent work has characterized the full polarization state of the bichromaticly generated circularly polarized harmonics, including the S_3 Stokes parameter that is required to determine the degree of polarization and that is often neglected [80]. They have found that harmonic ellipticities are on the order of 0.6 and that the harmonics are not fully polarized. In fact, for certain situations the degree of polarization has been reported to be as low as 0.4 (1 is fully polarized) [80]. This does not rule out applications but future work has to take these considerations into account.

Another method to generate circularly polarized harmonics by manipulating the driving field is the non-collinear approach. Here, a driving pulse is split into two and the resulting two pulses are converted to right and left handed circular polarization (RHCP and LHCP) respectively. Then they are focussed into the same spot in a gas jet with an angle to each other [32, 81]. Each individual pulse cannot generate harmonics by itself because it is circularly polarized. But, in the photon picture, one can imagine that harmonics are generated by sharing a certain number of photons from the RHCP and the LHCP field. The total number of photons is odd and the residual spin angular momentum is converted into the harmonic being circularly polarized [32]. Importantly, because for every harmonic, the mixture of photons from the LHCP and the RHCP field is different, each harmonic is emitted under a different angle. This method was used to generate and characterize arbitrary HHG polarization states [81] and for first magnetic circular dichroism measurements on an iron film [32]. The authors claimed that this was the only known method that would in principle allow the generation of a circularly polarized isolated attoscond pulse [32] although this has not yet been experimentally demonstrated. It will be interesting to see which of all these methods will be capable of detecting time-resolved dynamics reliably enough to draw scientifically important conclusions from them.

1.2 High harmonic generation from solids

After several works predicted that non-perturbative high harmonics could be generated from a crystalline structure [82–84], in 2011 it was first experimentally demonstrated by Ghimire *et al.* [38]. They irradiated a 500 μm-thick ZnO crystal with 3.25 μm wavelength, 9-cycle laser pulses with a peak electric field strength in matter of 0.6 V/Å and observed harmonics up to the 25^{th} order (9 eV). In contrast to the isotropic response of atomic gas HHG, they observed the harmonic yield to vary with rotation of the crystal, directly representing the crystal symmetry class of ZnO. A remarkable observation was furthermore that the high-harmonic cutoff scaled linearly with the electric field strength. This is contrary to the quadratic dependence in the cutoff law of gas HHG (Eq. 1.1). This fact already showed that some fundamental dynamics of solid HHG need to be different compared to its gas counterpart. It turns out that there are multiple dynamics in the crystal that can

emit high harmonics and significant amount of effort has been put into identifying which mechanism is dominating in what kind of systems and under which driving conditions. This section will first introduce the fundamental dynamics in the crystal in Sec. 1.2.1. Afterwards we shall review some important results related to solid HHG (Sec. 1.2.2) and finally, we will show the HHG results that are directly related to this work (Sec. 1.2.3).

1.2.1 Generation mechanisms

As a preface to this section, one should emphasize that despite extensive recent scientific effort on the topic, solid HHG is still lacking an intuitive 'simple-mans-model' that captures most of the observed phenomena and can be consulted to make reliable predictions. In fact, it is even unclear what 'most of the phenomena' means. Indeed, the investigated systems so far include unconventional ones like 2D materials [46, 85], topological materials [41], metamaterials [44], solidified rare-gas crystals [86] or amorphous glass [87]. But even the high-harmonic response of conventional crystals has been shown to differ from another much more than this is the case for rare gas atoms, with very low band gap materials that can be driven with 10 μm wavelengths emitting harmonics spanning almost the whole THz-range [88] or rather high band gaps materials like SiO_2, driven by Ti:Sapphire systems with harmonics well into the XUV-regime [89]. All this makes the high-harmonic response naturally very versatile and the fact that gas HHG can be described with a 'simple-mans-model' that captures most of the important physics might remain a luxury inherent to gas HHG. In any case, a lot can be learnt from the different models and instead of being too pessimistic about the theoretical descriptions we should discuss them appropriately.

In general, a crystalline insulator[§] can be described by a band structure, which consists of valence bands that are fully occupied and conduction bands that are initially unoccupied. When driven by a strong electric field, the electrons from the valence bands can be promoted to the conduction band, either by tunneling or multiphoton ionization. Once an electron is in the conduction band it can undergo extremely nonlinear, strong-field-driven dynamics which are usually grouped into transitions within a band (intraband) and transitions between bands (interband). As we shall see later, both intraband and interband dynamics can individually emit high harmonics. However, to complicate things further, both mechanisms are intrinsically coupled because one cannot have intraband dynamics without the tunneling step first and one cannot have high-harmonic interband transitions without having accelerated the electron to higher-lying states within a band first.

An instructive case to consider is a band structure that consists only of two bands: one valence and one conduction band (Fig. 1.5). This is a very minimalistic approach that fails to describe most real materials but it provides a useful picture of the prevalent dynamics. In this case, one could venture to simplify things even

[§]For the sake of argument, let us not differentiate between semiconductors and insulators here and consider any material with a Fermi energy within the band gap as an insulator

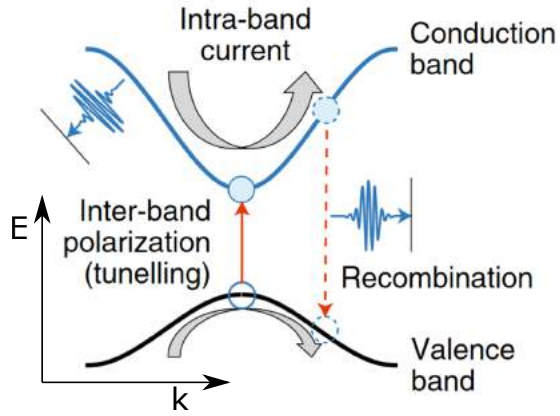

Figure 1.5: Visualization of interband and intraband dynamics that underlie solid HHG. Adapted from Ref. [90]

further and imagine a succession of steps when a strong laser field is applied to the system:

1. An electron is promoted from the valence to the conduction band by tunneling due to the strong electric field of the laser. Tunneling has an exponential dependence on the band gap and therefore this tunneling will most likely happen at the Γ-point, which is the **k**-value with the lowest band gap. The tunneling process leaves behind a hole in the valence band.

2. The electron oscillates in the conduction band driven by the electric field of the laser. The hole oscillates also. If the excursion in **k** exceeds the (first) Brillouin zone, Bloch oscillations occur.

3. The electron can recombine with a hole, emitting the momentary band gap energy as a photon.

The resemblance of this model to the three-step model of gas HHG is no accident and it has been in parts developed by the same people [91,92]. Note that there are certain, very important differences to the gas HHG case. While the acceleration step in gases happens in vacuum, in a solid, the electron is accelerated within the conduction band dispersion which manifests itself in a nonlinear dependence of the electrons' velocity on the driving electric field. This itself leads to an emission of higher frequency components and is one of the *intraband* mechanisms. It has absolutely no analogy to the gas HHG case.

It is also important to realize that the electron leaves behind a hole in the valence band which oscillates as well and can therefore also radiate. Its influence has been investigated only very little so far [93] but there is no fundamental reason to neglect it. Although the effective mass of the hole is usually higher than the electron, it is by no means as high as the mass of the positively charged parent ion in the gas HHG case [93–95].

Another important difference lies in the absence of clear trajectories. In gas HHG, one can ascribe a well defined trajectory to every ionization time and only those trajectories lead to high-harmonic emission that come back to the spatial origin of ionization. One can do a similar analysis in a solid by solving the Newtonian equations of motion for electron and hole with the respective band-dispersion-dependent group velocities [96]. This picture of trajectories in a solid is highly questionable however, even more so than the semiclassical trajectory picture in gas HHG. In a solid, electron waves are delocalized, which is precisely why the band structure description becomes so important. It is also feasible that electrons recombine with holes from different unit cells in which case this analysis needs to be refined. Furthermore, it is also conceivable that electrons remain in the conduction band for longer than one laser cycle and recombine at a later time. All this is not really accounted for in this simple model. For a comprehensive tutorial on the three-step model of solid HHG, see Ref. [96]. It has also recently been discussed by Ishikawa *et al.* in Ref. [97].

For a more general description, full quantum models have been developed. There are multiple approaches, for instance solving the time-dependent Schrödinger equation (TDSE) (see for instance Refs. [43, 98–100]), a density matrix formalism [92, 96] or, similarly, the semiconductor Bloch equations [84, 101, 102] in second quantization. Another approach are multiscale *ab-initio* TDDFT-simulations [103–105] which can be seen as numerical experiments, employing the complete band structure without any a-priori assumptions. These will support the experimental work in Chap. 2.

As said in the beginning of this section, there is a lively debate about the most appropriate formalism and especially about adjustments that need to be made to match experimental data. For instance, the dephasing time constitutes a great uncertainty, with works claiming extremely low dephasing times on a fraction of the pulse duration [92] while Floss *et al.* discuss that accounting for intensity variations over the beam focus can overcome the assumption of these small dephasing times [106].

Let us follow here the approach of Kira, Koch *et al.* which does not treat the nonlinear dynamics as a succession of steps. Although extension to two-dimensional systems is straight forward, the one-dimensional case shall be used for now. Then, the interband ($P(t)$) and intraband ($J(t)$) dynamics are generally given as [84, 102]:

$$P(t) = \sum_k \left[d_k p_k(t) + c.c. \right], \tag{1.6}$$

$$J(t) = \sum_{\lambda,k} e v_k^\lambda n_k^\lambda(t). \tag{1.7}$$

Here, d_k is the interband dipole matrix element, λ is the band index and can be chosen such that the group velocity v_k^λ describes electrons and holes. *c.c.* is the complex conjugate. $n_k^\lambda(t)$ and $p_k(t)$, which represent the time-dependent occupations and polarizations can be calculated by solving the semiconductor optical Bloch equations (SCOBEs) numerically [84]. Importantly, in the SCOBEs neither

the interband nor the intraband contributions are decoupled from another. That means, $n_k^\lambda(t)$ depends on $p_k(t)$ and vice versa.

The crystal momentum $k(t)$ is described by the acceleration theorem

$$\frac{\mathrm{d}}{\mathrm{d}t}k(t) = -\frac{e}{\hbar}E_L(t). \tag{1.8}$$

Here, it is apparent that light-induced shifts of the wavevector require high electric field strengths and this does usually not happen in conventional semiconductor optics. Therefore, there, intraband dynamics are usually neglected. For the electric field strengths discussed here, the transient shifts of k described by Eq. 1.8 can even exceed the width of the Brillouin zone and hence, intraband dynamics become very important. It should be noted however, that, although it is quite oftenly used, the acceleration theorem has been shown to overestimate the crystal momentum when the full multiband dynamics are included [105].

The time-dependent electric field is given by

$$E(t) \propto \frac{\partial}{\partial t}P(t) + J(t), \tag{1.9}$$

and finally, the emitted frequency spectrum is obtained by Fourier transforming $E(t)$

$$I(\omega) = |E(\omega)|^2 \propto |\omega P(\omega) + iJ(\omega)|^2 . \tag{1.10}$$

$\omega P(\omega)$ is the contribution of interband dynamics, $iJ(\omega)$ represents the intraband contribution. Many works compare these two terms and then, e.g. conclude that interband dynamics dominate [91, 92], however, it is apparent that there is a coupling term between them too that is often ignored. In any case, let us elaborate a little on the different mechanisms and what to expect from them.

The most obvious nonlinear intraband dynamics results from the fact that the electron velocity is

$$\mathbf{v}_k = \frac{1}{\hbar}\nabla\mathcal{E}_k \tag{1.11}$$

In vacuum, the free electron dispersion is proportional to $\mathbf{k}^2$. This causes the electron velocity to be proportional to its momentum. In a crystal, however, this is not the case. For instance, in a nearest-neighbor tight-binding approximation the conduction band dispersion is $\mathcal{E}_k \propto 1 - \cos(k)$ (see Fig. 1.5) [107]. In other cases, $\nabla\mathcal{E}_k$ can even change sign, causing the electron to move opposite to the electric field. This nonlinear dependence of the velocity on the electric field causes emission of higher frequency components, which end up being high harmonics when happening in succession over multiple half-cycles of a laser pulse.

There are even more unique dynamics when an electron (or a hole) is accelerated by a strong electric field within a band. Consider a DC electric field that is permanently increasing the momentum $\mathbf{k}$ of a crystal electron. Once $\mathbf{k}$ reaches the Brillouin-zone edge, the crystal momentum is reversed to its negative value.

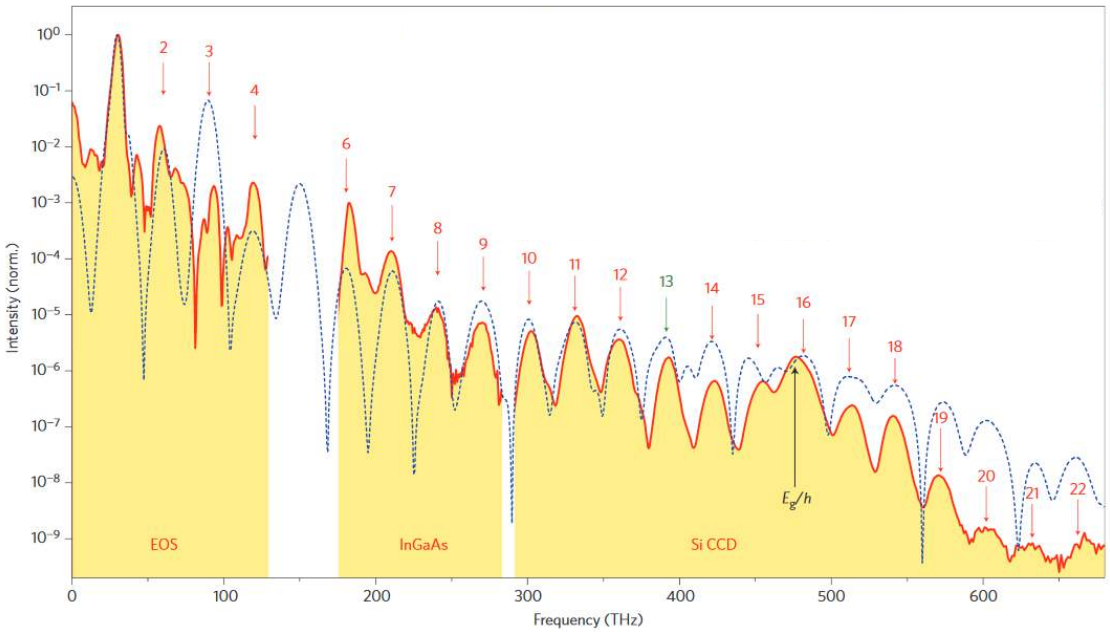

Figure 1.6: Dynamical Bloch oscillations leading to a high-harmonic spectrum spanning almost the entire THz-range. The blue dashed line is a simulated curve. Reprinted from Ref. [88].

One way to visualize this is that the wavelength of the Bloch wave describing an electron equals the lattice constant and this causes Bragg reflection on the lattice. If the DC field continues to be applied the electron momentum then describes a so called Bloch oscillation with the frequency

$$\omega_B = \frac{ae|E|}{\hbar}. \tag{1.12}$$

Here, a is the lattice constant and E the electric field strength. This idea has been brought forward almost 100 years ago by Bloch [108] and Zener [109] but could never be observed because the scattering times within solid materials are much shorter than the time period determined by Eq. 1.12 [110] for DC-electric fields that could realistically be applied to a solid. However, with the advent of semiconductor superlattices - artificial structures with much greater 'global' lattice constants a - the observation of Bloch oscillations seemed to be feasible [111]. Finally, in the early 1990's Bloch oscillations have been observed [112] and subsequently also the THz radiation they emitted [113]. So far, this discussion revolved around static electric fields but of course in principle a far off resonant ultrafast laser pulse could also drive an electron to the Brillouin-zone edge. This requires a relatively long wavelength such that electrons get accelerated for longer times in one half-cycle of the field before it reverses sign and shifts the momentum to the other direction. In fact, once again, ultrafast laser pulses turn out to be ideal drivers for this because field strengths comparable to the inner-atomic electric field strengths can be applied without destroying the crystal. Shortly after the

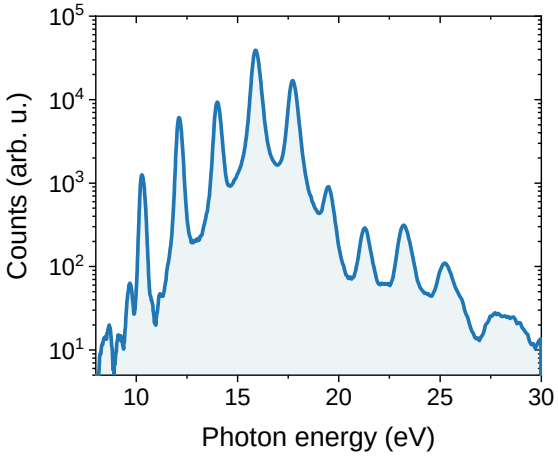

Figure 1.7: HHG XUV-spectrum taken from MgO with 1.3 μm, 30 fs pulses. Harmonics above 20 eV form a second plateau. The spectrum is not calibrated for spectrometer response, especially the harmonic around 10 eV is at the edge of detection range.

experimental discovery of solid HHG, Schubert *et al.* have irradiated a GaSe crystal with 30 THz pulses and 0.7 V/Å peak electric field strength. They detected harmonics up to the 22$^{\text{nd}}$-order through-out almost the entire THz-range [88] - formerly called the THz-gap. Simulations revealed that the electrons in their case passed the Brillouin-zone edge and this obviously is a source of highly nonlinear oscillation that emits high harmonics by itself - purely by intraband dynamics [88].

Intraband dynamics result in a linear dependence of the harmonic cutoff versus electric field strength, as has been observed in ZnO [38]. After having established that even without any recombination, we would expect non-perturbative high-order harmonics from solids due to the intraband dynamics, we can also look at the recombination step, which is referred to as *interband* mechanism.

The interband mechanism resembles the recollision mechanism of gas HHG, with some important differences that we should mention here. In a gas, the cutoff is proportional to the ponderomotive potential. In a solid, this dependency is much less clear. The energy of the electron depends on the precise band structure and, since the hole also moves, it is much less obvious which conditions maximize the electrons energy at time of recollision. What can be stated with certainty is that for each band the maximum band gap and therefore the maximum achievable photon energy is limited. If one drives electrons further than this point, it will undergo Bragg reflection at the zone boundary and then decrease its momentary band gap again. On the other hand, it can also enter a higher conduction band with a higher maximum band gap. This behaviour causes multiple cutoffs to appear [86, 99]. In Fig. 1.7 this behaviour is experimentally observed from MgO.

The relative importance of intraband and interband mechanism has been one of the main targets of investigations of solid HHG publications so far. For both mechanisms there have been numerous publications claiming it to dominate. From

experimental side, one way to extract the generation mechanism is attosecond streaking which allows reconstructing the full temporal profile of the high harmonic pulses [18, 114, 115]. In an interband scenario, one would expect different photon energies to be emitted at different times - the so-called attochirp [96]. Streaking experiments performed with HHG from SiO_2 showed basically no group delay for different high-harmonic photon energies [116], indicating high-harmonic emission due to intraband dynamics. As mentioned already, the Bloch oscillation experiments on GaSe showed also dominating intraband dynamics [88]. On the other hand, by adding a second harmonic field to the fundamental with a variable time delay, Vampa *et al.* showed, that the optimum delay between ω-2ω field in ZnO corresponds to the optimum delay one would expect for interband dynamics [91]. As argued earlier, showing that one mechanism dominates in one scenario does not imply that this is the case for all systems and driving conditions. Generally, as can be seen from the SCOBEs and Eq. 1.10 one cannot isolate one mechanism from the other.

As pointed out by Tancogne-Dejean *et al.*, there are two situations however, where one can say with relative certainty that interband dynamics should play a minor role [104, 105]. First of all, the minimum energy difference between valence and conduction band is the minimum energy for which interband transitions can occur. If harmonics below this photon energy are observed, they are generated by intraband dynamics. Secondly, for harmonics above the direct band gap to be emitted via interband polarization it is required that there are electronics states in this energy range. The joint density of states (JDOS) is defined as [117]

$$\rho_{cv}(\hbar\omega) = \int_{BZ} \frac{d\mathbf{k}}{|\nabla_k (E_c - E_v)|_{E_c - E_v = \hbar\omega}}. \tag{1.13}$$

E_c and E_v are $\mathbf{k}$-dependent conduction and valence bands respectively. One can see that the greatest contributions to the JDOS come from either extrema of both bands, or if $E_c - E_v$ remains constant for a large range of $\mathbf{k}$. Importantly, decreasing ρ_{cv} decreases also the likeliness of interband transitions to occur [104]. Hence, if harmonics are observed in an energy range with low ρ_{cv}, they stem most likely from intraband dynamics. This line of reasoning will be important throughout this thesis.

1.2.2 Prospects

One can identify three major categories that underlie the interest in high harmonic generation from solids: to use it as a compact source of VUV- or XUV-radiation, to use it as a spectroscopic tool or, closely related, to use it as signatures of ultrafast oscillations that could be used for Petahertz (PHz)-electronics. Let us look at these points individually.

Looking through a gas HHG perspective on solid HHG, the most obvious application might be to use it as a photon source for experiments. This is compelling because solid HHG allows for relatively compact setups (no gas capillary, no differential pumping stages). This is even more true, considering the required pulse

energies to produce high harmonics from solids. The intensities required for solid HHG are limited by the damage threshold of the respective crystal. While it is impossible to give a general figure for this damage threshold because it depends on the crystal, pulse duration, wavelength and the number of shots [118–121], it can be estimated that peak electric fields are on the order of 0.1 - 1V/Å, which is ten to hundred times lower than in the gas HHG case. On the other hand, also the charge concentrations are about hundred times higher in a crystal than in a noble gas of 100 mbar. The lower damage threshold could just mean that one relies on oscillators, which can produce CEP-stable sub-two-cycle pulses with MHz-repetition rate [122, 123], as it has been done with metal-sapphire nanostructures [124]. It is also possible to use fiber lasers with MHz-repetition rate [125]. Both approaches are far more compact and cheaper than any gas HHG setup. With relatively low peak electric field strengths it can also be thought of to implement solid HHG-based attosecond sources on a chip. In any case, if the field strengths are not high enough, solid samples offer unique opportunities for field enhancement via plasmonic structures that are implemented directly on the samples [124, 126]. Also refocusing or other kind of manipulation of the high-harmonic beam can done with structuring the solid sample [127]. Another interesting, very recent development is the generation of high harmonics in reflection [128–130]. Because in reflection the crystals' thickness can be ignored, one can imagine using bulky crystals with a large surface aperture. By irradiating these with mJ-level pulses (or even higher) that are not focussed down so hard, one should be able to greatly enhance the high-harmonic brightness. This can not be easily done with gas HHG.

The maximum achievable photon energy seems to be limited thus far to the low end of the XUV-photon-energy range, with maximum photon energies around 40 eV, generated with a hollow-core-fiber pumped sub-cycle waveform synthesizer [89, 131]. This is orders of magnitude lower than the achievable cutoff in gas HHG. Currently, the cutoff law is not well understood and it is probably dependent on the precise generation dynamics. The cutoff does not simply scale linearly with the electric field as found in Ref. [38], because the appearance of a second plateau can give a sudden sharp increase of the cutoff photon energy [86]. Also the wavelength-dependence is unclear. While some works predict an increase of the cutoff with driving wavelength [132], other works predict that such dependencies do not exist [104, 133]. Currently one would most probably refrain from using the XUV-radiation emitted by solid HHG for further experiments as researchers do with gas HHG. But then again, solid HHG is also still a very young field.

Just like HHG from gases can be used to study atomic dynamics itself on attosecond timescales (see, e.g., Refs. [20, 134]), solid HHG offers a unique perspective into a large range of ultrafast strong-field dynamics in a solid. Solid HHG has been used for instance to reconstruct the band structure from ZnO [39], SiO_2 [89] and ZnSe [40]. Because electrons driven in a band are also influenced by the Berry curvature, recent work reported the Berry curvature to be reconstructed from SiO_2 [135] by high-harmonic spectroscopy. Generally, the discussion if high-harmonic emission is dominated by intra- or interband dynamics is by itself not an HHG discussion but a discussion about how strong-field-driven charge dynamics

play out in an insulator. The lively debate about this topic demonstrates how many fundamental questions still exist in this field. Furthermore, high-harmonic spectroscopy has been proposed as a method to investigate novel quantum materials that are even less understood than common semiconductors. For instance one could track light-induced changes of the Hubbard U with HHG from NiO [42] or one could observe phase transitions in topological insulators [41, 136]. The latter relies on characterizing the polarization-states of emitted harmonics.

It is also clear that high-harmonic emission is a direct signature of induced PHz-oscillations in the solid. These reversible dynamics happen on time scales that can currently not be triggered in other ways. If one could control these currents one could think of developing devices with PHz bandwidth [137–140] which would break new ground in capabilities to sample light fields or even for new kind of computing tasks. One key problem of this development is that clock rates are given by the repetition rate of the laser which, currently, are not faster than the MHz scale (when using oscillators). It will be interesting to observe what the future holds for PHz-computing and which role solid HHG will play in understanding the underlying dynamics further.

1.2.3 Elliptical driving polarization and polarization of the harmonics

As argued in Sec. 1.1.2, investigating gas HHG with elliptical[¶] excitation was paramount to the development of both the semiclassical as well as the full quantum mechanical description. For solid HHG, the analysis of the ellipticity-response can be argued to play an even more vital role. Steering the electrons in a two-dimensional cut of the band structure will imprint signatures onto the high-harmonic spectra that have no counterpart in gas HHG. This is due to the intraband mechanism on the one hand but also due to the **k**-dependent JDOS (see Eq. 1.13). This is similarly true for the high-harmonic yield as well as the polarization states of the high harmonics. Both can count as fingerprints of the fastest light-wave-driven charge dynamics in solids and solid HHG seems to be a natural probe to these. Also, one can argue that insights into the generation mechanism of solid HHG itself can be gained by studying the high-harmonic response with elliptical excitation.

Already the first experimental paper on solid HHG by Ghimire *et al.* therefore investigated the harmonics' spectra with driving ellipticities ϵ of 0, 0.5 and 1. They observed a decrease of harmonic yield with increasing ellipticity. This decrease was, however, much weaker than in the case of gas HHG. The interpretation was that the HHG process is not limited to 'ionization and recombination at the same [atomic] site' (quoted from Ref. [38]). Contrarily, in crystallized rare-gas solids, the harmonics' yield has been shown to decrease very rapidly with increasing ellipticities - even more rapidly than in the corresponding gas case [86].

In 2017, You *et al.* reported several remarkable observations by studying the

[¶]For convenience, unless it is otherwise noted, in this thesis the terms elliptical and circular are abbreviations for elliptically polarized and circularly polarized.

harmonics' yield of HH19 (high harmonic 19) from MgO versus driving ellipticity [45]. Irradiating a 200 μm-thin, (100)-cut crystal with 1.3 μm driving pulses of 50 fs pulse durations, they found that the harmonics' ellipticity-dependence was strongly anisotropic for the four crystal rotations shown. With driving major axis along the Mg-O bonding direction they observed a decreasing yield of HH19 with increasing ellipticity up to a value of $\epsilon \approx 0.4$. For $\epsilon > 0.4$ the harmonic yield increased again, with significant harmonic yield for circular excitation. The behavior was even more astounding when the major axis was oriented along the Mg-Mg bonding direction. Here, the very weak harmonic signal with linearly polarized excitation could be *enhanced* with increasing ellipticity, peaking at a value of $\epsilon = 0.65$. The ellipticity dependencies were symmetric with respect to the helicity along those major symmetry axes of the crystal. When rotating the crystal such that the major axis of the driving field was off a major symmetry axis, they found that the ellipticity dependencies became asymmetric, i.e. that the yield differed when irradiating with the same absolute ellipticity but opposite helicity. While the symmetry-related results could be easily understood by considering the cubic symmetry of MgO, the other results came as a surprise to researchers. How can elliptical polarization enhance the harmonic yield? What does it mean to have harmonic yield for circular excitation? Can one naively assume that circularly polarized harmonics are generated, as was observed for perturbative harmonic generation [141, 142] or does the strong-field character of HHG affect the polarization-states of the emitted harmonics in a different way? In the same paper, the authors attempted to explain their results with a semiclassical real-space-trajectory recollision model. Electrons were said to be promoted to the conduction band at the spatial position of the O atoms and were then subsequently accelerated by the laser field. If the resulting electron trajectory was colliding with another atomic site, the yield would be enhanced, if it wouldn't the yield would decrease. This is basically an extension of the recollision model in gas HHG with the difference that recollisions do not happen at the point of ionization (they cannot because trajectories do not come back with elliptical excitation) but with any other atomic site. This model was able to qualitatively explain some of the observed results however it raises also some fundamental questions: In gas HHG, the harmonics are emitted as the wave packet interferes with itself. How does this work for recollision with a neighbouring atomic site, especially if this is a different type of atom (Mg instead of O)? Can a real-space-trajectory picture really capture the dynamics in a crystal where electron waves are delocalized? Furthermore, the model seems to predict different harmonic yields for LHCP and for RHCP which was also observed in the experiment (see Fig. 5 in [45]) but is forbidden by symmetry for a cubic system. Also, with this model it seems that the emitted harmonics have linear polarization, which is questionable, especially in light of the results presented in this thesis. These questions were not really addressed in Ref. [45].

In a more recent publication, the same Stanford group measured the polarization of the high harmonics generated from MgO generated with linearly polarized driving fields [143], also from a sample with 200 μm thickness. Interestingly, they found that the harmonics were rotated with respect to the driving axis when ir-

radiated off a major symmetry axis of the MgO-crystal. In an attempt to explain these results they used the same model as in Ref. [45] and assumed the electrons' velocity vector at moment of recollision to correspond to the harmonics' polarization. They were able to predict different behavior of HH13-HH15 to HH17-HH19 due to different conduction bands but the model failed when predicting the directions of HH17-HH19. It is clear that such a model can not provide a quantitative solution to the complicated dynamics of solid HHG, especially for the higher lying conduction bands. The model however did predict some details quite accurately, for instance the angle dependence with driving field strength. So it could perhaps be used to provide an intuitive general idea. But if harmonics were found to be emitted elliptically polarized in certain situations, the recollision model would have a hard time explaining it. In Chapter 3, an alternative simplified model for rotated major axes will be presented that does also include elliptically polarized harmonics - although probably not valid for MgO.

Using an *ab-initio* TDDFT approach, Tancogne-Dejean *et al.* were able to theoretically reproduce the experimentally measured ellipticity dependencies from MgO [45] and predicted that different harmonic orders would exhibit different ellipticity responses [105]. This was argued to be due to the different interplay of interband and intraband contributions. In silicon, this reasoning led to the separation of harmonics generated by coupled intraband and interband dynamics (high JDOS) and harmonics generated only by intraband dynamics (low JDOS) [104]. Those two classes of harmonics showed different ellipticity dependencies. Perhaps most importantly, the authors argued that circularly polarized harmonics could be generated from both Si and MgO with circularly polarized excitation. In this case, subsequent harmonics were predicted to have counter-rotating helicities as is known from selection rules of the gas HHG case. Furthermore, the authors predicted that the dependence of the harmonics' ellipticities ϵ_n on the driving ellipticities ϵ was non-trivial and also that the harmonics' polarization-state could be changing over the course of the pulse duration. Another impressive prediction was - counter-intuitively coming from gas HHG - that elliptical excitation could *increase* the high-harmonic cutoff in MgO along ΓK-direction. This last prediction will be investigated in Chapter 4.

When the project that is summarized in this thesis started, basically only these works existed (excluding [143]). The goal of this thesis was to investigate the predictions of [105] and to gain a deeper understanding of the ellipticity-response of HHG from solids. However, during the course of these four years, other researchers have worked on related problems and those shall be summarized in the next paragraphs.

The first and so far only other work that studied the polarization of high harmonics from solids generated by elliptically polarized fields has done so from 2D-materials like Graphene and MoS_2 [46]. There, the authors found, similarly to Ref. [45], that the harmonic yield in graphene could be enhanced with elliptical excitation. In fact, with increasing ellipticity, they found that the field component parallel to the major axis of the driving ellipse was decreasing in strength while the perpendicular component increased to a value three times larger than

the parallel component. This caused harmonics to be almost perpendicularly polarized with respect to the driving ellipse for $\epsilon = 0.32$. However, the harmonics remained more or less linearly polarized, which implies that the relative phase between these two components is close to zero. For circular excitation, the harmonics vanished. The authors developed a full quantum model [144] with which they were able to explain their observations. Graphene is a metal with a band gap of zero and a Dirac cone in the conduction band and therefore, its behavior is known to be quite unique [145]. For example, the authors in Ref. [46] reported that the harmonics' behavior was independent on the crystal rotation. This makes a lot of sense, considering that the Dirac cone of graphene is isotropic. But this behavior is quite unusual, considering most band structures are strongly anisotropic. MoS_2 exhibited an atomic-like ellipticity dependence. Its harmonic yield was monotonically decreasing with increasing ellipticity and the perpendicular component of the harmonics' polarization ellipse remained close to zero for any driving ellipticity.

The first report of a non-perturbatively generated circularly polarized high-harmonic from solid has been given by us at the ATTO-conference in 2017 [146]. However, the first peer-reviewed research article appeared shortly after by Saito and coworkers [147]. In a crisp study, Saito *et al.* demonstrated that high harmonics generated from a 30-μm-thin, z-cut GaSe crystal with circularly polarized 3.5 μm pulses followed the selection rules that have been brought forward theoretically long before solid HHG was discovered (In Refs. [141, 142] with conventional perturbative nonlinear polarization analysis, in Ref. [148] with group theoretical methods for arbitrary crystal symmetries and harmonic order as well as in Ref. [149] with a Floquet-type analysis specifically for HHG). In their case, the three-fold symmetric crystal GaSe led to odd and even harmonic orders with linear excitation. When switching to circular excitation however, they observed every third harmonic order to disappear. The remaining harmonics were circularly polarized and counter-rotating. The results could be explained in numerous ways. An intuitive one is that the crystal symmetry class is imprinted onto the fully symmetric circular driving field. Imprinting an N-fold crystal symmetry on the driving field leads exactly to selection rules of the kind [147]

$$n_{HH} = \sigma + Nj, (j \in \mathbb{N}). \tag{1.14}$$

Here, n_{HH} is the harmonic order and $\sigma = \pm 1$ the helicity of the harmonic. It means that for a three-fold symmetric crystal only the harmonic orders $3j \pm 1$ are allowed. Interestingly, Saito *et al.* also showed that the harmonic yield for linear and circular drving polarization was the same for the allowed harmonics with their driving conditions and sample.

The last two publications that shall be described here tried to extract physical insights about the charge dynamics by polarization-resolved analysis. The semiclassical equation of motion for a charge within a single band is

$$\mathbf{v} = \frac{1}{\hbar}\frac{\partial E_k(\mathbf{k})}{\partial \mathbf{k}} - \frac{e}{\hbar}\mathbf{E}(t) \times \mathbf{\Omega}(\mathbf{k}). \tag{1.15}$$

The first term is the conventional dependence of velocity and the band derivative and known from physics textbooks. The second term is called the anomalous velocity and includes the Berry curvature $\mathbf{\Omega}(k)$. The anomalous velocity needed to be added to the equation after Berry carefully investigated the previously unacknowledged phase that a quantum particle accumulates after propagating in a closed loop [150]. It is a recent and still rather mysterious quantity that is very important for the development of lively topics like topological insulators (Nobel price for physics in 2016 [151]). In Eq. 1.15, it is apparent that the anomalous velocity term causes a polarization component perpendicular to the driving field $\mathbf{E}(t)$. Also, it can be shown that for nearest-neighbor-type tight-binding band structures the second term is responsible for the generation of even harmonics and the first term for odd harmonics [85,135]. Note that Eq. 1.15 ignores contribution of multiple bands, i.e. interband dynamics. This argumentation led to two papers that analyzed the Berry curvature from the even-order harmonic response from the two-dimensional material MoS_2 and from SiO_2. In the latter, in which the polarization major-axis of XUV harmonics has been analyzed, the authors have even reconstructed the Berry curvature.

With papers that reconstructed the one-dimensional band structure with high-harmonic spectroscopy [39, 89] and here, also the Berry curvature in one direction [135], it should be very interesting to do this with elliptical excitation. This would allow for reconstruction of these quantities in the full two or even three-dimensional $\mathbf{k}$-space, potentially with the attosecond time resolution that is inherent to HHG.

This chapter introduced the field of HHG both from gases and solids and has elaborated on the differences and the current status of solid HHG. It can be expected that polarization-state-resolved analysis of solid HHG will become a key part of ultrafast oscillation analysis in insulators (and semiconductors) as well as in novel quantum materials like topological insulators or strongly correlated materials. Introducing elliptical excitation simultaneously allows for probing the charge dynamics uniquely in a multidimensional space opening up new avenues for spectroscopic tools with degrees of freedom that gas HHG spectroscopy does not have. The next chapters will revolve around precisely those tools.

Chapter 2

Visible high harmonics and their response to ellipticity

This chapter experimentally scrutinizes the high-harmonic response to elliptically polarized excitation. The most significant role in these investigations will be played by a set of experiments in Sec. 2.3, in which the polarization states of the harmonics are investigated. As argued in the previous chapter, this has not been done prior to this work with elliptically polarized - and even very scarcely with circularly polarized [147] - excitation. When doing so, it comes natural to not only study the polarization states but also the high-harmonic yields under the same excitation conditions. This is done in Sec. 2.2. The experimental setup and methods that enabled the subsequent research are described in Sec. 2.1.

But first, let us start with some general remarks on these experiments. HHG can be an extremely broadband light source and thus, the experimentalist can chose different wavelength ranges to study. Optics, spectrometers and the experimental methods need to be chosen in compliance with this wavelength range. Moreover, the absorption of air for photon energies larger than roughly 6 eV (wavelength smaller than 200 nm) poses a hard boundary. If one wishes to investigate harmonics in the VUV or EUV-region, one needs to place the experimental setup into vacuum and it becomes increasingly difficult to manipulate the harmonics itself, for instance with a polarizer.

In this chapter, we limit ourselves to the detection of harmonics that do still propagate in air, i.e. wavelengths mostly visible to the human eye*. From a gas-HHG perspective, this might seem like a surprisingly low photon energy range, since there, typical HHG spectra are shown in the XUV. This is because the XUV-signal is the most interesting part of the spectrum for further experiments on the one hand, but also because laser wavelengths are typically rather low (800 nm) and thus, there are only a few harmonic orders above 200 nm. However, if we can live with the fact that the detected radiation is not particularly useful for further experiments, it will be much simpler to study HHG in the visible range.

*For simplicity, let us call wavelengths between 200 nm and 700 nm 'visible', although this is a slight exaggeration of the eye's performance.

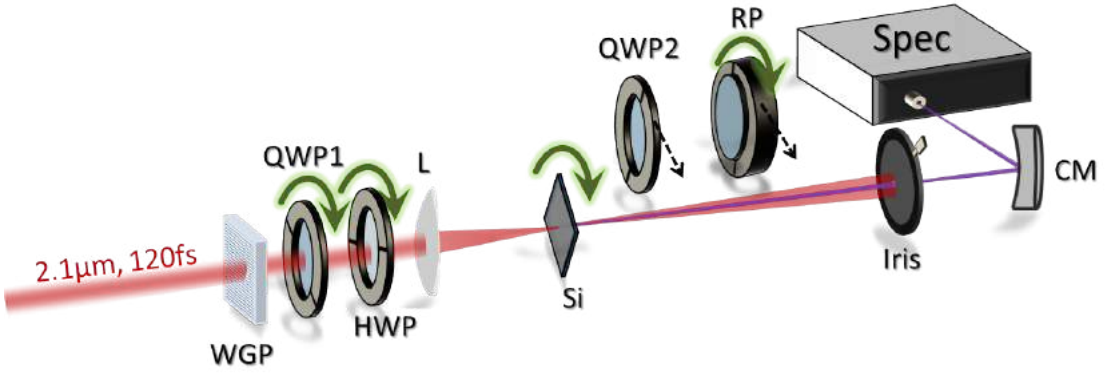

Figure 2.1: Schematic of the experimental setup.

This is valid if we show that those harmonics are generated non-perturbatively, as we will do. Then, from a physics stand point, there seems to be no substantial difference between high harmonics in different wavelength regimes. It should be noted that there is a lively discussion about this topic. Claims have been made that high harmonics generated in the XUV range tend to be generated by the interband mechanism (see e.g. ref. [152]). However, contrary to this claim lies the fact that the highest photon energies generated from solids to date were modeled with an intraband-only theoretical description [89, 116]. It is clear, that high-harmonic emission stems from the extremely nonlinear charge dynamics in the band structure where intra- and interband dynamics are intrinsically coupled. Hence, any differentiation between low-order and high-order seems to be artificial as long as high harmonics are generated non-perturbatively.

2.1 Experimental setup and procedure

Let us first discuss the overall experimental scheme before later sections will look at the individual components in detail. The experimental setup is sketched in Fig. 2.1. A home-built CEP-stable OPA-source delivers 120 fs pulses at 2.1 μm with pulse energies of 13 μJ (Sec. 2.1.1). The pulse energy is adjusted with ND-filters. The polarization state of the incoming light pulses is fixed by transmitting through a wire-grid polarizer (WGP) in order to get it properly linearly polarized first. The transmission through a quarter-wave plate (QWP) and a half-wave plate (HWP) allows for setting any ellipticity while keeping the major axis fixed (Sec. 2.1.5). Unless otherwise noted, the pulses are focused with a CaF_2-lens of 25 cm focal length. The sample is mounted in a motorized rotational stage and placed in the focus (Sec. 2.1.2). After 50 cm of propagation, an iris is used to spatially suppress the otherwise very strong third harmonic. The light is then coupled into an *Ocean Optics HR4000* spectrometer with a curved mirror (CM) made out of UV-enhanced aluminum ($f = 5$ cm). It was beneficial to use a curved mirror

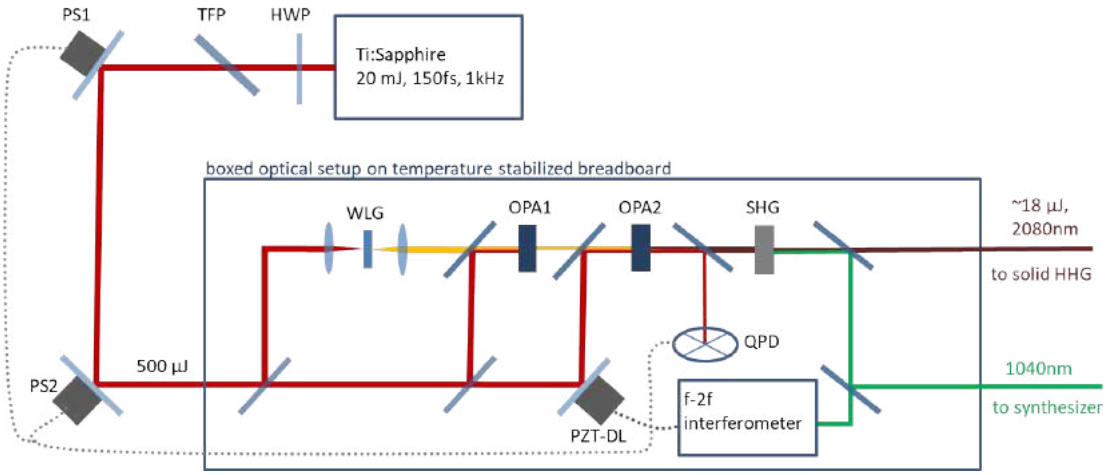

Figure 2.2: Schematic drawing of the OPA source. TFP: Thin-film polarizer; PS: Pointing stabilizer; WLG: White-light generation; SHG: Second-harmonic generation; QPD: Quadrant photo-diode; PZT-DL: Piezo delay stage. Redrawn from Refs. [58, 154]

instead of a lens to avoid chromatic aberrations and hence to align the setup in such a way that it is optimized for all harmonics at the same time. Depending on the experiment, a Rochon polarizer (RP) was added between the sample and the spectrometer. A rochon polarizer is an intrinsically broadband polarizer that transmits the ordinary ray with no spatial deviation. The RP used here was made from α-BBO, which is transmissive between between 190 nm and 3500 nm. For measurements of the Stokes parameters (Sec. 2.3.3), a tunable QWP was added between sample and RP. In later experiments (Sec. 2.4.2 & 2.4.3), a Fresnel rhomb was used instead of a second QWP, which served the same purpose but acted as an ultrabroadband QWP as it geometrically induces a $\pi/4$-phase shift by multiple internal reflections.

2.1.1 OPA-source

The OPA-source that was used in these experiments was developed by Dr. G. M. Rossi and Dr. R. E. Mainz to be employed as a CEP stable seed laser for subsequent amplification stages of a sub-cycle parametric waveform synthesizer. Although briefly described here, for a deeper reading the reader is advised to Refs. [153, 154] or other works that describe white-light-seeded optical parametric amplifiers. The development and maintenance of this system was out of the scope of the author's work.

The OPA is pumped with a commercial cryogenically-cooled Ti:sapphire laser system (*Coherent Legend Elite Cryo PA*) that delivers 150 fs pulses with ~20 mJ and 1 kHz repetition rate. A small part (~500 μJ) of this energy is coupled into the boxed and temperate-stabilized OPA-system. There, yet another small portion of it is used to generate a white-light continuum from a 2mm YAG crystal by means

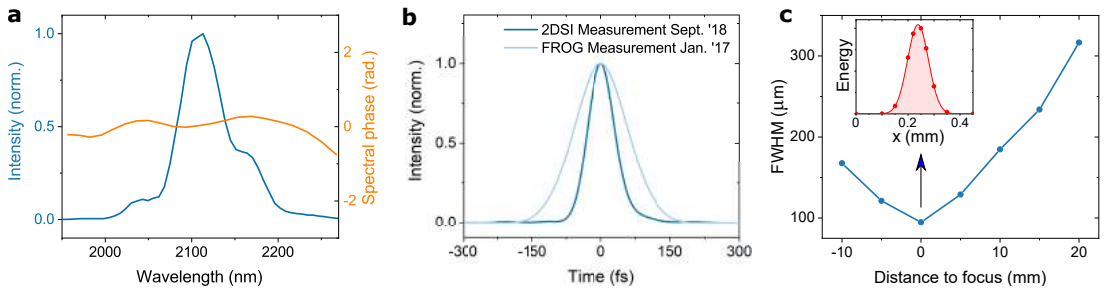

Figure 2.3: **a**: Fundamental spectrum with reconstructed spectral phase from 2DSI (F. Scheiba). **b**: Two measurements of the reconstructed temporal intensity, one of the frequency-doubled idler with FROG from 2017 (Dr. G. Cirmi), one of the 2080 nm pulse with 2DSI from 2018 (F. Scheiba). **c**: The FWHM-beam diameter after transmitting through a CaF_2-lens ($f = 250$ mm) as reconstructed with a knife-edge. Inlet shows the differentiation of the knife-edge measurement in the focus. Solid line in the inlet is a Gaussian fit.

of SPM. A first OPA-stage amplifies the spectral region around 1300 nm (BBO type-II 2.5 mm, $\theta = 25.9°$). A narrow-band band-pass filer selects a 3 nm wide wavelength region around 1300 nm to ensure that the seed pulse duration exceeds the pump duration [155]. Then another BBO amplifies this spectrum and also generates the passively CEP-stable [155] idler (BBO type-II 4 mm, $\theta = 25.9°$) at 2080 nm with ~40 μJ. In order to pump the white lights of the synthesizer, this idler is then frequency doubled in another BBO (type-I 0.5 mm). For the experiments here however, the residual idler at 2080 nm was used.

Due to its purpose of serving as a seed for a sub-cycle waveform synthesizer, great effort has been put into stabilization of this system. The input pulses are spatially stabilized with a beam-pointing-stabilizer system. The whole OPA-system is boxed and build on a breadboard that is slightly heated above room temperature to actively stabilize the temperature below 1 mK rms. This reduces drifts of the optics due to long-term temperature changes of the ambient air. An f-2f interferometer measures CEP-fluctuations for every laser shot and sends a feedback control signal to a piezo delay stage, actively locking the CEP to fluctuations of ~150 mrad rms for the 2080 nm pulses [153]. Note that the precise central wavelength of the idler is subject to the exact phase-matching conditions achieved in the BBO's and thus, it varies throughout this thesis between roughly 2080 nm and 2120 nm.

The spectrum (Fig. 2.3**a**) shows slight side-lobes that are residues of pump-depletion by the frequency-doubling. The precise shape of the spectrum was changing slightly over the course of the project due to differently achieved phase-matching conditions in the SHG-crystal. The spectral phase, as has been reconstructed by 2DSI (F. Scheiba), shows the pulses are well compressed, leading to a FWHM-pulse duration of 73 fs. A FROG measurement from before this project was started (by Dr. G. Cirmi) of the frequency-doubled 1040 nm pulses showed a pulse duration of 120 fs, also without any significant chirp. This difference is

a little surprising because typically one would expect the second harmonic to be shorter than the fundamental. Note that this discrepancy does not stem from using two different methods, as also a FROG measurement was taken after the 2DSI measurement, giving a similar result around 70 fs. Since the OPA was sometimes re-optimized after this project was started, we will assume that the pulse duration changed meanwhile the measurements presented in the chapter took place. Hence, let us assume a 120 fs pulse duration for the most part of this chapter, while the last experiments, that were done around the same time of the 2DSI-measurement, were done with a pulse duration of 73 fs. Note that since these are many-cycle pulses, the precise pulse duration does not affect any of the interpretation and only influences the stated value for the peak intensity - which in any case is a parameter prone to experimental uncertainties.

Another important parameter that determines the peak intensity is the beam size, which has been determined by inserting a knife edge lateral to the beam while measuring the transmitted pulse energy behind. The derivative of the function, describing the laser energy over knife-edge position is then equal to the lateral (one-dimensional) beam profile. In our case, the differentiation has a Gaussian shape, as is shown in the inlet of Fig. 2.3**c**. The FWHM is calculated from the Gaussian fit and plotted for different positions along the beam propagation direction in Fig. 2.3**c**. With these focusing conditions, the FWHM beam diameter in the focus is 95 μm.

The peak intensity is

$$I_{\mathrm{pk}} = \frac{E}{\tau \pi r^2}, \tag{2.1}$$

where E is the pulse energy, τ the pulse duration and r the FWHM beam radius. With the parameters discussed here, and with 120 fs pulse duration, we get $I_{\mathrm{pk}} = 0.6\,\mathrm{TW/cm^2}$ in the focus. Note that typically for a Gaussian beam, I_{pk} is multiplied with a factor of two. In our case, since this intensity will be important also for cross-checking with the TDDFT-calculations, we decided to take the intensity as described by Eq. 2.1. This 'averaged' peak intensity over the focus makes sense in our case, as the whole focal spot is likely to contribute to the high-harmonic emission process.

2.1.2 Crystal considerations

Most of the experimental work described in this chapter was done with silicon. Silicon was an appealing choice for a number of reasons:

1. Silicon has arguably been the most important technological material of the past century and, with silicon photonics on the rising, it continues to inhabit that role. Because it has been extremely well studied, it is a captivating idea to explore completely new strong-field dynamics of it.

2. A consequence of the previous point is that the manufacturing capabilities of silicon are among the most sophisticated. Thus, silicon can be obtained extremely thin with a good surface quality for a relatively low price.

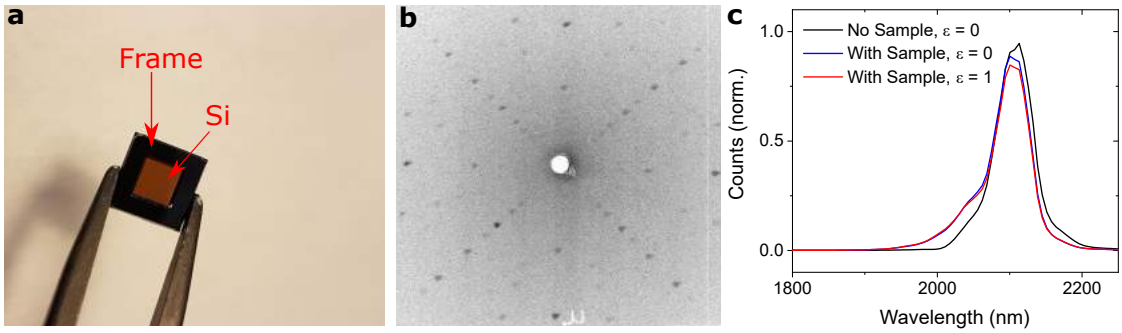

Figure 2.4: **a**: 3.5 mm × 3.5 mm wide, 2 μm thin silicon sample. **b**: X-ray diffraction data of that sample (acquired with the help of M. Spiwek). **c**: Fundamental spectrum with and without being propagated through the 2 μm silicon sample. ϵ denotes the ellipticity, $\epsilon = 1$ is circular polarization.

3. Silicon is known as a semiconductor with a 1.1 eV indirect band gap. To promote an electron via the indirect band gap however requires interaction with a phonon which can usually be neglected on the sub-optical-cycle ultrafast timescales that are discussed in this thesis. The direct (optical) band gap of silicon lies at 3.3 eV. That means, with our excitation energy of 0.59 eV, 6 photons are required to promote electrons to the conduction band. This fulfills the requirement of being far off-resonant for solid HHG. Furthermore, this band gap value means that we can observe two harmonic orders below the band gap (HH3, HH5) and two above (HH7, HH9) which will be helpful for interpretation.

4. Silicon can and has been simulated with the *ab-initio* TDDFT approach of our collaboration partners (N. Tancogne Dejean, A. Rubio).

5. At the beginning of this project, no peer-reviewed work has reported experiments on solid HHG from silicon. Hence, even the most basic experiments presented novelty in itself.

It is extremely important to keep samples as thin as possible in solid HHG. While for perturbative harmonic generation in crystals and HHG in gases, it is a common attempt to increase the interaction length of the laser with the medium (as long as phase-matching can hold up), solid HHG often concerns above-band-gap harmonics and in this case, re-absorption of those plays a pivotal role. Although any other material could be discussed here, let us look at the absorption coefficient of silicon. Here, a wavelength of 300 nm (HH7 in our case) experiences an absorption coefficient of $\alpha = 1.759 \cdot 10^8\,\mathrm{m}^{-1}$ [156]. This means, its intensity drops by e^{-2} after propagating for only 11 nm. For HH9, the situation is similar. Consequently, any crystal thickness greater than this does not increase the harmonic yield at the output surface of the crystal. Quite to the contrary, considering the other highly nonlinear processes that a pulse of such high electric field strengths will experience during propagation, it is desirable to keep the sample as thin as possible.

Of course, a few nanometers thickness are usually not feasible, at least not for free-standing samples. In personal experience, after changing from 20 μm-thin Si crystals to 2 μm-thin Si crystals, the high-harmonic yield increased by a factor of ten. We also did experiments with 200 nm-thin samples however those turned out to be too fragile to work with on a day-to-day basis.

Especially for spectroscopy that requires precise knowledge of the input pulse, samples that are thick enough for the pulse to undergo nonlinear effects prior to the ones under investigation make a thorough analysis quite challenging. For this reason, recent works have proposed to work in reflection [129, 157, 158]. However, as pointed out in point 2) of the previous list, silicon can be manufactured quite thin with a good optical quality and therefore propagation effects should play a minor role. Propagation effects will become important later and will be discussed accordingly (Sec. 4.2.3).

We have mostly worked with silicon samples from *Norcada*. Fig. 2.4**a** shows a photograph of one of their samples. Fig. 2.4**b** shows an x-ray diffraction measurement that reveals the mono-crystalline nature of the sample and that it has cubic symmetry. This x-ray diffraction pattern has been acquired at the facilities of DESY with the assistance of M. Spiwek. With the 2 μm Si sample predominantly discussed in this chapter, the driving spectrum does change slightly due to nonlinear propagation effects (Fig. 2.4**c**) however a change of this small magnitude can be expected to play a minor role for HHG. Polarization-related propagation effects on these samples will be looked at in Sec. 2.1.5.

2.1.3 Data acquisition

To perform the measurements, four motorized rotational stages needed to be controlled and scanned, i.e. QWP, HWP, sample and polarizer. For each rotation angle of any of those stages, a spectrum had to be acquired. It is important to subtract a dark spectrum from the acquired spectra to avoid influences of the ambient lighting and electronic noise of the spectrometer. Since the final measurements were taken non-stop over 48 hours, the ambient lighting and that noise level could change over that period, making it a necessity to record additional dark spectra in between the measurements. All of these requirements were fulfilled with a MATLAB routine that was written by G. Di Sciacca, supervised by the author of this thesis.

Fig. 2.5 shows the graphical user interface (GUI) of that MATLAB routine. First of all it includes the 'obvious' tasks, i.e. moving the four motorized rotational stages independently of another within a given range and with a certain step size. For any set of stage-positions, the program acquires spectra with a given integration time and averaging number. The user can enter a folder name and the program will create this folder with an exact datetime string attached in the name. The program saves each measured spectrum as a '.txt'-file. Additionally, a MATLAB '.mat'-file is created that contains a structure, including every measurement as well as information about the scanned values and the other input parameters. For required subsequent data analysis it is enough to import the '.mat'-file.

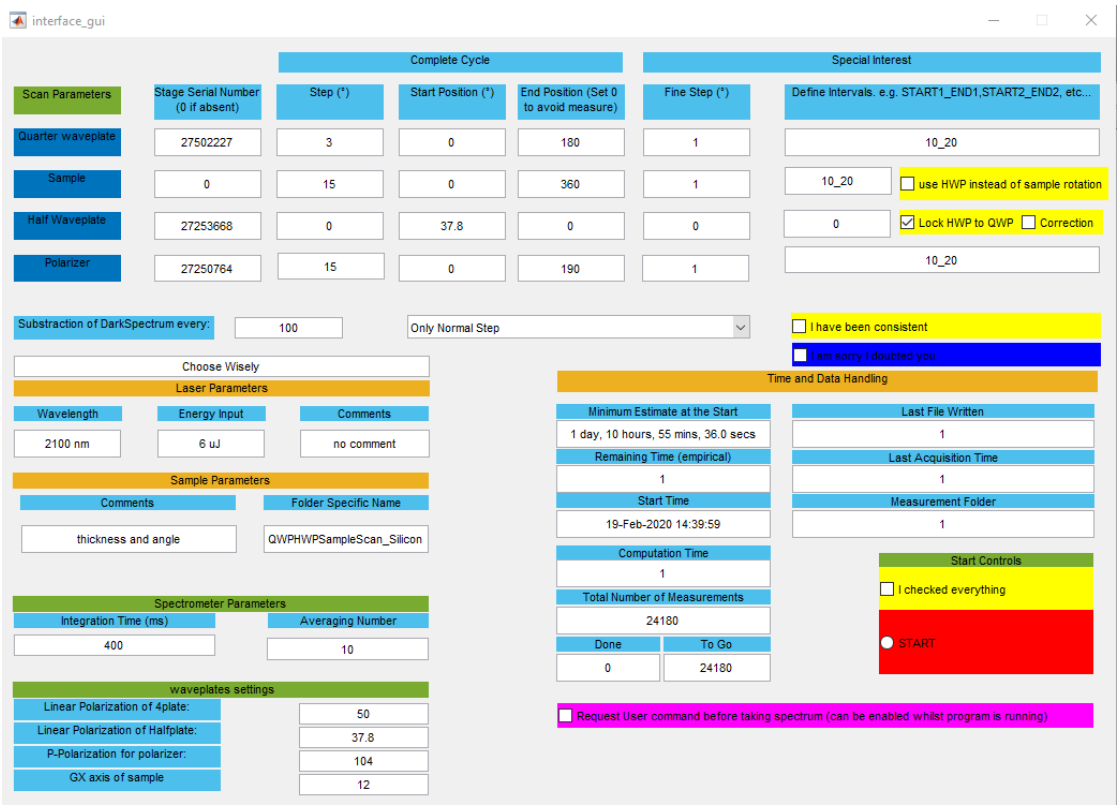

Figure 2.5: The Matlab GUI.

With a motorized shutter in the beam path, the program allows for subtraction of a new dark spectrum after a given amount of spectra. Furthermore, the user can choose to lock the HWP-angle to the QWP-angle, such that the HWP is moved with the fixed relationship to the QWP that keeps the major axis of the driving ellipse constant (see Sec. 2.1.5). However, the HWP can also rotate independently. This is useful if one wants to rotate the light field instead of the sample, for instance if the samples' surface is irregular and different positions on it give different results. The GUI calculates the duration of the measurement which turned out to be a particularly useful feature especially for the longer measurements.

The program can also be used with a Coherent powermeter instead of the Ocean Optics spectrometer. This allows to automatically calibrate the waveplates, as will be discussed in Sec. 2.1.5.

2.1.4 Data analysis

For any spectrum that is acquired, the harmonic yield can be calculated either as an integration over the harmonic peak or as the maximum value of an harmonic peak. In the solid-HHG-literature it is usually not stated how people define the harmonic yield. We found very little differences between the two methods and hence, to be consistent with the definition of our collaboration partners, use the integration method to calculate the harmonic yield [105].

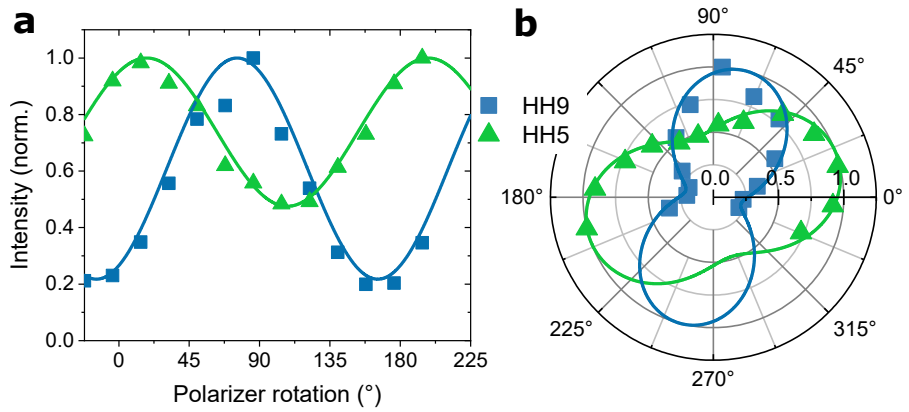

Figure 2.6: Polarization scans for HH5 and HH9 from silicon with $\epsilon = 0.32$ and $\theta = \Gamma X + 5°$. **b** shows the same data as **a** but as polar plot. Solid lines are $\sin^2$-fits.

We have two different types of datasets that need to be evaluated. To simplify things, let us refer to the combined QWP and HWP rotation as ϵ (meaning the driving ellipticity), to the sample rotation as θ and to the polarizer rotation as ξ. If only interested in the harmonic yield, spectra are acquired under variation of ϵ and θ and the polarizer is not in the beam path (This is the case in Sec. 2.2). The harmonic yield is calculated for each of the harmonics, depends on ϵ and θ (and the driving intensity) and can thus be further analyzed.

If interested in the harmonics' polarization states, complexity of data analysis slightly increases. The inserted polarizer in the beam path means that the harmonic yield depends now on ϵ, θ and ξ. Moreover, because the ξ-dependence carries the information about the polarization state of the harmonic, individual ξ-scans need to be evaluated as a whole. Typically, in these experiments, the polarizer is rotated in 13 steps of 18°. The harmonic yield in dependence of ξ can then be fitted with the function $I(\xi) = b - a\cos(2(\xi - \phi))$ (this is Malus law for elliptically polarized light and basically a $\sin^2$-fit.). Here, ϕ is the major-axis rotation of the harmonics' polarization ellipse. Also, the absolute value of the harmonic ellipticity of harmonic order n is

$$|\epsilon_n| = \sqrt{\frac{min[I_n(\xi)]}{max[I_n(\xi)]}}. \tag{2.2}$$

I_n is the intensity of the n^{th}-harmonic.

Note that these kind of measurements are not sensitive to the helicity of the harmonics, i.e. the sign of ϵ_n (this will be addressed in Sec. 2.3.3). For each polarizer scan, the fit is individually calculated for HH5, HH7 and HH9. Fig. 2.6 shows HH5 and HH9 for an exemplary polarizer scan, including the respective fits as solid lines. Because the data is sampled quite well with a step size 10 times smaller than the period, the fits are usually of good accuracy. Polar plots are a great and intuitive way to visualize polarizer scans, as can be seen in fig. 2.6**b**. Here the angle is the polarizer rotation angle while the radial distance is the normalized

intensity. In the case of this data set we find:

$$\epsilon_5 = 0.69 \tag{2.3}$$
$$\epsilon_9 = 0.47 \tag{2.4}$$
$$\phi_5 = 17.9^\circ \tag{2.5}$$
$$\phi_9 = 75.7^\circ. \tag{2.6}$$

Without any further reference, these values might feel a little out of place here, although it can be noted that ϵ and ϕ are different for different harmonics with the same driving conditions. This will be one important result of Sec. 2.3 and hence, will be discussed thoroughly there.

As discussed in the next section, calibration of the QWP and the HWP requires careful characterization of their influence on the polarization state of the driving laser pulses. This is done very similarly as for harmonics by rotating a polarizer and calculating ϵ and θ as defined above.

Because the reflectivity of mirrors and the grating in the spectrometer can differ for p- and s-polarization, it is important to calibrate this influence for all the wavelengths that are relevant here. This has been done with an unpolarized white-light source and it was found that p- and s- polarization differ by up to 15% in intensity. When evaluating the ξ-scan in post-processing, these calibration measurements have been taken into account.

2.1.5 Waveplate calibration

An ideal quarter-wave plate (QWP) acts on a monochromatic linearly polarized light wave by shifting the phase of one axis to the phase of the perpendicular axis by $\pi/2$. Here, we call the angle between the initial linear polarization direction and the fast axis of the QWP α. $\alpha = 0^\circ$ will do nothing to the light wave, while $\alpha = 45^\circ$ will convert it circular polarization. For $0 < \alpha < 45^\circ$, the light wave will not only be elliptically polarized but also experience a rotation of its major axis by the angle $-\alpha$. To adjust ϵ without rotating the major axis, an additional HWP can be used. To confirm this, let us consult the Jones-matrix for a rotated retarder [159, 160]:

$$\mathbf{J}_R(\beta, \alpha) = \begin{pmatrix} \cos(\beta/2) + i\sin(\beta/2)\cos(2\alpha) & i\sin(\beta/2)\sin(2\alpha) \\ i\sin(\beta/2)\sin(2\alpha) & \cos(\beta/2) - i\sin(\beta/2)\cos(2\alpha) \end{pmatrix}. \tag{2.7}$$

β is the phase shift introduced by the retarder (for a QWP it is $\pi/2$, for a HWP π) and α is the rotation angle of its fast axis relative to the lab frame. In Fig. 2.7, the Jones calculus has been applied to calculate the polarization ellipse of an originally linearly polarized light field after propagating through a single QWP with angle α (blue) as well as after propagating through a QWP with angle α and a HWP with angle $\alpha/2$. As it is apparent from this figure, the major axis can be fixed if the HWP is set to the angle $\alpha/2$.

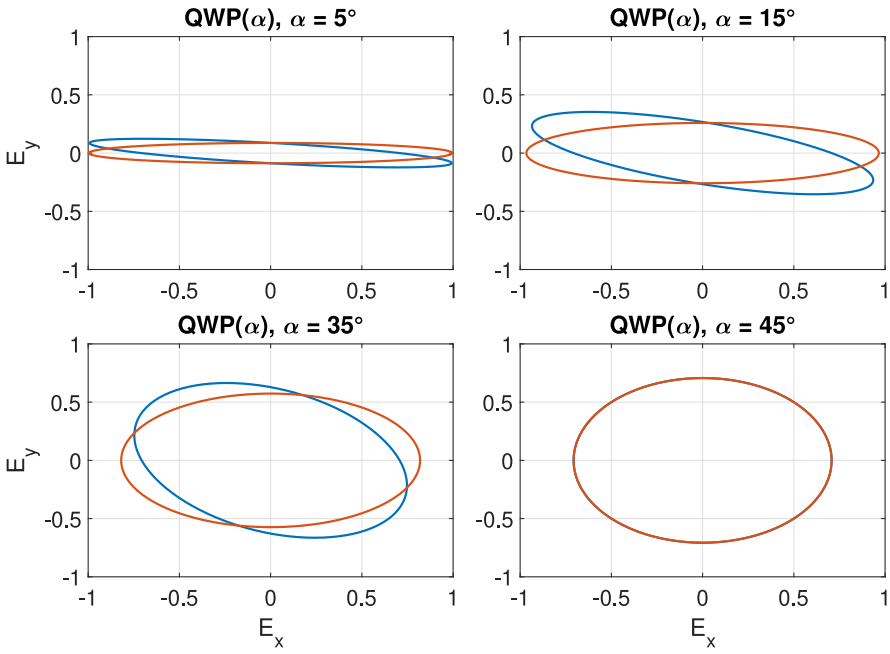

Figure 2.7: Calculation to demonstrate influence of a QWP on the polarization major axis and the ellipticity of an initially linearly polarized light field. The angle α is the angle between initial polarization axis (horizontal) and the fast axis of the QWP. Blue: Propagation through a QWP with angle α. Red: Propagation through a QWP with angle α and a HWP with $\alpha/2$.

Of course in the real world, waveplates are not perfect and the laser pulses have a certain bandwidth. Because a strongly nonlinear process like solid HHG is extremely sensitive to the exact driving conditions (especially ϵ and θ), great care has to be taken to characterize both QWP and HWP as well as to calibrate both of their influences on the laser pulses. As an example, Ref. [45] shows ellipticity profiles from MgO with two orders of magnitude different harmonic yields for $\epsilon = -1$ and $\epsilon = 1$. In a cubic material like MgO and with multi-cycle laser pulses, it should not make a difference if the driving field is rotating clockwise or counterclockwise when it is circularly polarized. One explanation for this could be that the waveplates were not carefully calibrated there but of course that is only speculation.

In our case, the waveplates were calibrated by propagating the laser pulses through them and a subsequent Rochon polarizer that is rotated in 10 steps between 0° and 200° for every configuration of QWP and HWP angle. The transmitted power through the polarizer was measured with a *Coherent* power meter. The resulting curves were then fitted with an $I(\xi) = b - a\cos(2(\xi - \phi))$ function. From the fit, $|\epsilon|$ has been calculated as described in the previous section for the harmonics.

Figure 2.8**a** shows the hereby obtained calibration of the QWP and HWP ensemble. One can see that the major-axis remains within 3° for $|\epsilon| < 0.8$. We were

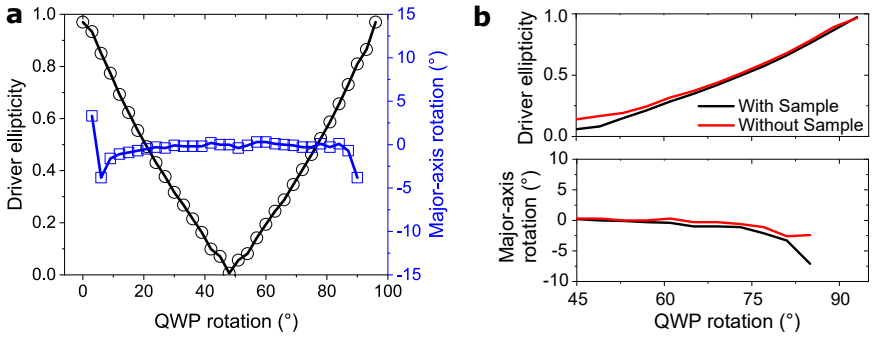

Figure 2.8: **a**: Calibration of QWP and HWP. **b**: Assessment of prevalent birefringence effects by measurement of ϵ and θ with and without a silicon sample in the focus. Here sample is placed such that θ is oriented along ΓK.

able to reach ellipticity values between $0.02 < |\epsilon| < 0.97$. Actually to reach perfectly linear polarization turns out to be quite challenging. The energy resolution for standard commercial powermeters is on the order of 100 nJ and hence, when using 8 μJ pulses, it is difficult to measure $\epsilon < 0.1$ and any measurement in this range needs to be taken with a grain of salt. Also to achieve perfectly circular polarization is challenging because the light before the QWP needs to be as linearly polarized as possible, which, as argued before, is difficult. In fact two wire-grid polarizers before the QWP were used, to have a well defined linearly polarized laser pulses.

Influence of birefringence effects of the 2 μm Si sample are neglible, as is shown in Fig. 2.8**b**. Difference in θ appear only for large ϵ-values, where the major axis alltogether is not so well defined anymore. ϵ differs slightly for close-to linear polarization. As elaborated on before, it is difficult to determine the polarization state for $\epsilon \approx 0$ in any case.

2.2 Yield-resolved high-harmonic analysis

2.2.1 Perturbative and non-perturbative harmonics

With the spectrometer cutting off at 200 nm and a driving wavelength of 2100 nm, harmonics up to the ninth order can be detected. Fig. 2.9**a** shows typical spectra, in this case for three different driving intensities. Silicon is a cubic crystal with inversion symmetry which explains why only odd harmonics are observed [38, 162]. HH3 is consistently the strongest of all harmonics and it is saturating the detector for 0.6 TW/cm^2. Although it would be definitely also interesting to study the transition from perturbative to non-perturbative behavior of HH3, in this work, mainly the harmonics 5,7 and 9 will be discussed. Those are rather similar in magnitude and therefore simultaneous detection of those makes the experimentalists life easier. Additionally for those harmonics, the term 'high-harmonic generation' seems slightly more appropriate than for the lowest-possible harmonic order 3.

When studying relatively low-order high-harmonic generation from solids one

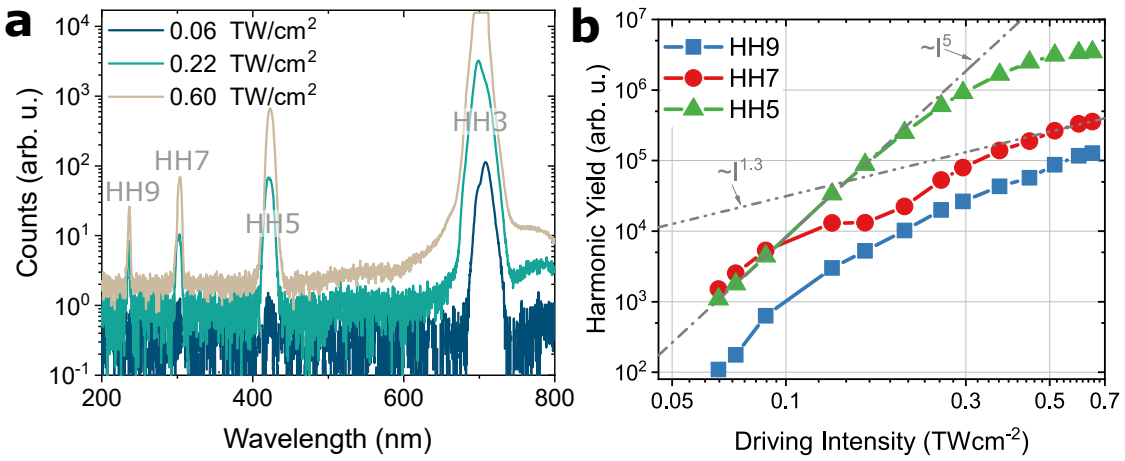

Figure 2.9: **a**: Typical high-harmonic spectra from silicon with three different driving intensities. **b**: Scaling of harmonics 5,7 and 9 with the driving intensity. Linearly polarized driver. **b** is adapted from [161]

has to make sure that these harmonics are indeed generated in a non-perturbative fashion, instead of the conventional harmonic generation which is commonly described as anharmonic oscillations of the localized electron clouds. This can be confirmed by measuring the dependence of harmonics' yields versus driving intensity. A perturbative behavior would imply a power scaling of $I_n \propto I^n$. Deviations to this are a good indication for the non-perturbative nature of the harmonics. Here, I is the driving pulse intensity, n is the harmonic order and I_n the corresponding harmonic intensity.

Fig. 2.9**b** shows the intensity scaling for HH5, HH7 and HH9. With low driving intensities, HH5 follows exactly the expected perturbative power scaling. The higher harmonics 7 and 9 seem to already deviate from their power scaling with the lowest intensities scanned here. It is possible that they only appear in a non-perturbative fashion, since these are already relatively high harmonic orders.

For driving intensities above $0.2\,\mathrm{TW/cm^2}$, also HH5 starts to deviate from its power scaling. For the highest intensities one can see a saturation-like intensity dependence for all harmonics, which is consistent with earlier observations on HHG from solids [38, 85, 88, 126, 163]. This is clearly non-perturbative behavior. Unless otherwise noted, the experiments in this chapter will be done with $0.6\,\mathrm{TW/cm^2}$. For intensities above approximately $0.8\,\mathrm{TW/cm^2}$ laser-induced damage on the sample has been observed which appeared as a decreasing harmonic yield over time.

On another note, the behavior of HH7 in this scan is quite peculiar. One would not expect a higher harmonic to be more intense than a lower harmonic, especially for low intensities, where perturbative nonlinear optics might still be applied. In Ref. [130] a very similar behavior is observed and there, it is speculated that these anomalies can stem from resonant effect due to strong features in the JDOS. Indeed, due to the high JDOS in the energy range of HH7 - being just above the direct band gap - it is feasible that interband effects already start to arise in this driving intensity range. For HH5, on the other hand, because it is below the

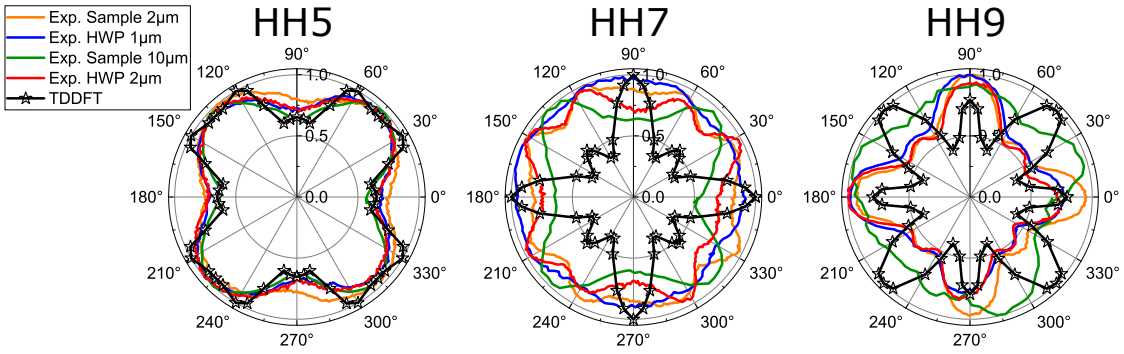

Figure 2.10: The harmonic yields of HH5-HH9 versus rotation of the laser ('HWP') or the crystal ('Sample') for different sample thicknesses. 'Exp.' refers to experimental data, 'TDDFT' to TDDFT simulations performed by N. Tancogne-Dejean.

direct band gap, this cannot happen. Further work would be needed to clarify this behavior but it seems to be a signature of the transition from perturbative to non-perturbative nonlinear optics.

2.2.2 Sample rotation, influence of sample thickness and first comparison to simulations

Having established the non-perturbative nature of the generated harmonics, one can think of the first real experiments to perform. Something that might come to mind when the sample is mounted on a rotational stage, is rotating the crystal with rotational axis parallel to the laser propagation direction. Since a crystal is anisotropic in general, one would expect different harmonics' behavior for different crystal orientations [38, 45]. A serious investigation of rotation-dependent spectra poses an important practical requirement on the sample quality. Since the center of this rotation does generally not coincide with the position on which the laser beam hits the sample, rotating the sample means that the laser will hit a different spot on it. Generally, in order to draw conclusions out of this experiment, it is required that the influence of spot-to-spot variations due to surface quality is rather low. In the authors own experience, this is not always a problem but depends on the crystal, the vendor and the thickness. To find out if whatever variation in the harmonic yield originates from spot-to-spot variations or from the crystal orientation, one can also keep the sample fixed but rotate the HWP. This should negate the influence of spot-to-spot variations. In Fig. 2.10, these kind of measurements have been done for different sample thicknesses. Here 'Sample' refers to rotation of the sample while 'HWP' refers to rotation of the HWP with the HWP rotation angle multiplied by two.

In these plots, 0° is the (100)-crystal direction, or ΓX in reciprocal coordinates. 45° is (110) or ΓK accordingly. All harmonic signals are four-fold symmetric, as one would expect from a cubic crystal. HH5 peaks along ΓK while HH9 peaks along ΓX. For HH7, the sample thickness has an impact on the direction with

maximum yield. The 10 μm sample peaks along ΓK while 2 μm-samples seem to maximize approximately 15° off ΓK. 1 μm thickness shows hardly any dependence on rotation.

In general, one wants to keep the sample thickness as small as possible to mitigate the influence of non-linear propagation effects on the driving laser. If the pulse is unaffected by propagation effects, this clearly helps for interpreting the obtained harmonic spectra. Furthermore, as mentioned in Sec. 2.1.2, the harmonic yield could be greatly enhanced with decreasing sample thickness. All this is a trade off however, because thinner samples are not only more expensive, they often exhibit mechanical weaknesses, leading to variations over the sample surface and therefore cause (above mentioned) spot-to-spot variations in the harmonic signal. For the 1 μm sample that was used here, the signal clearly differed for different spots on the sample (not shown). Since the results obtained from HWP rotation on the 1 μm sample have been rather similar to the results of the 2 μm sample rotation scans, all further measurements on the (100)-silicon crystals have been performed with a thickness of 2 μm. The 2 μm sample from *Norcada* exhibited great reproducible surface quality, as can be validated by comparing the orange and red curves in Fig. 2.10.

Fig. 2.10 also shows first comparisons with *ab-initio* TDDFT-calculations performed by N. Tancogne-Dejean. In these, the quantum-mechanical response of one unit cell to the oscillating laser field is computed, by taking into account the complete band structure and the real crystal structure. Things that are not included are surface and propagation effects as well as dephasing (for details on the simulations, see Refs. [104, 105]). This means that differences can arise from propagation effects introduced by the samples' thickness but also scattering and dephasing are not included of which the influence on solid HHG spectra is not yet fully resolved [91, 106]. For HH5, these calculations show almost perfect agreement to the measurements. For HH9, the main features are well reproduced however their relative intensities are not properly captured by the simulations. For HH7, the agreement is quite bad and it is clear that some important aspects of the strong-field processes prevalent here are not properly accounted for in the simulations. Since HH7 and HH9 are harmonics above the bandgap, they are only emitted within the last few atomic layers of the crystal. Therefore, they will heavily be influenced by the propagation of the laser pulse and maybe also by surface effects. Furthermore, the TDDFT-description ignores not so well understood effects such as, for instance, said electron-electron interactions. It has been argued before that dephasing plays a crucial role in solid HHG [92] so some of the discrepancies in comparing experiment and TDDFT could also originate from that.

2.2.3 Dependence on ellipticity and sample rotation

Before diving deeper into this topic, let us take a moment to define some variables and clarify the symmetries that we should expect when scanning ellipticity ϵ and sample rotation θ simultaneously. Fig. 2.11 shows a visualization of the crystals' lattice (atoms in blue) with its major symmetry directions (100) and (110). The

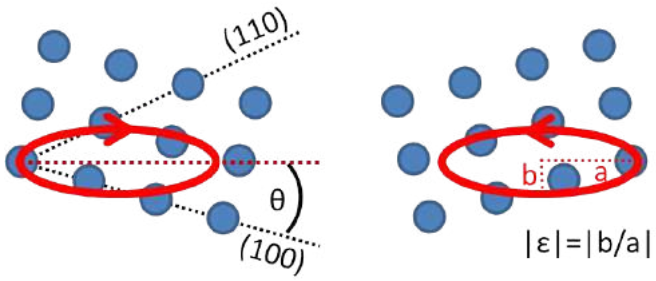

Figure 2.11: Definition of the relevant variables ellipticity ϵ and sample rotation θ. Furthermore visualization of the symmetry between $(\epsilon, \theta) \iff (-\epsilon, -\theta)$.

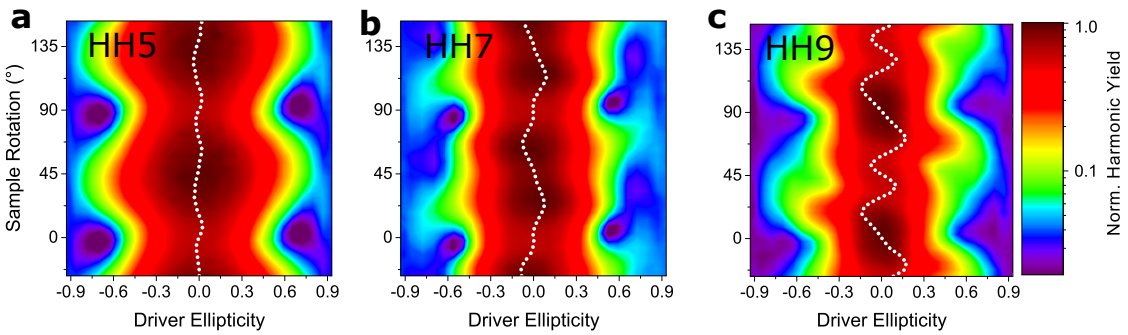

Figure 2.12: Measured harmonic yields of HH5-HH9 in dependence of the driving ellipticity and sample rotation. 0° refers to ΓX direction, 45° to ΓK. White dotted lines are the centers of mass of the distributions (×5 to enhance visibility of the variation). Adapted from [161].

driving electric field ellipse is depicted in red. In (100)-cut Si, the variable θ is defined as the angle between the driving major axis and the (100)-crystal direction (equivalent to ΓX in reciprocal space). ϵ on the other hand is defined as minor axis divided by major axis, while the sign of ϵ gives its handedness. The difference between left and right panels is that ϵ and θ have been transformed to $-\epsilon$ and $-\theta$. From this we see directly that for a cubic crystal like silicon, we should expect the same results for this type of transformation, i.e. $(\epsilon, \theta) \iff (-\epsilon, -\theta)$. Only the handedness of the polarization ellipses of the harmonics should be subject to change but this will be discussed later. Further symmetry rules that we can expect are $(\epsilon, \theta) \iff (\epsilon, \theta \pm 90°)$ as well as $(\epsilon, \theta) \iff (-\epsilon, 90° - \theta)$.

After having clarified the major definitions and symmetries, Fig. 2.12 shows scans of ϵ and θ and the respective normalized yields of HH5, HH7 and HH9 on logarithmic scale. Such a complete dataset, depicting the harmonics' dependence on ϵ and θ has not been shown from solids before. The ellipticity responses in Refs. [45, 46] already revealed that one can expect deviations from the strictly monotonically decreasing harmonic yields with increasing driver ellipticity in the atomic case. But here, this behavior is investigated for multiple harmonics simultaneously and for every sample rotation.

First of all, one can nicely observe above discussed symmetries, i.e. again 90° repetition of the harmonic yields as well as the same harmonic yields for $(\epsilon, \theta) \iff (-\epsilon, -\theta)$ and $(\epsilon, \theta) \iff (-\epsilon, 90° - \theta)$. Those are purely dependent on the crystal symmetry and we can expect to find them for every cubic crystal - completely independent of its band structure.

Let us discuss the individual harmonics behavior starting from HH5. HH5 is the harmonic order with the lowest photon energy of the ones presented here. Thus, electron oscillations that emit HH5 stem most likely from relatively low excursions in the conduction band. Electrons are predominantly promoted to the conduction band at the Γ-point, which is the **k**-value with the lowest direct band gap. The conduction band dispersion of Si can be approximated with a parabolic **k**-dependence close to this Γ-point. HH5 is a low-order harmonic which photon energy lies below the optical band gap. It can therefore only be generated by the intraband mechanism by electrons with relatively low energy. HH5 exhibits a response similarly to the atomic case with monotonically decreasing yield for increasing $|\epsilon|$ for almost all θ. As will be argued in Sec. 3.2.2, the intraband mechanism alone does not necessarily predict a decrease of the harmonic yield with increasing $|\epsilon|$. The fact that we observe it here can mean that the band structure of silicon is shaped in such a way that elliptical polarization decreases the yield of HH5, as argued in [161]. However, the decrease of harmonic yield could also originate from a decrease of electrons being promoted to the conduction band. The driving field strength scales with $1/\sqrt{1+\epsilon^2}$ and, because electrons are promoted to the CB by tunneling, any decrease in the field strength will cause significant less tunneling [164]. Thereby less electrons will contribute to the harmonic emission process. This seems to be one reason for the decrease of harmonic yield, especially since this is generally a recurring behavior for all harmonics from Si. Exceptions to the monotonically decreasing yield of HH5 can be found along $\theta = \Gamma X$ (0°, 90°). Here, for $\epsilon = 0.7$, the yield almost disappears and then increases again for even higher ϵ. This is unquestionably due to the specific shape of the band structure.

The behavior of HH7 and HH9 carries clear non-atomic signatures. For those harmonics, one can note quite generally that the yield-distributions are asymmetric around $\epsilon = 0$. Ref. [45] explains these kind of asymmetries with a real-space-trajectory recollision model in which electrons start its path close to the electronegative oxygen atoms in MgO. However, such a model is not applicable here because silicon is a monoatomic crystal and electrons can be expected to be delocalized in space. Furthermore, the high-harmonic response stems from coupled intra- and interband dynamics, which makes interpretation even more complicated. One can see how an interband mechanism could cause such asymmetries: Electrons would have different momentary band gaps at different times when driven with ϵ or $-\epsilon$. But also the JDOS is different for different helicities, which alters the interband contribution all together. These effects could lead to a different ratio of harmonics being emitted with different helicities. How a pure intraband process could generate these asymmetries is unclear. Ultimately, these kind of asymmetries are not well understood and the most secure, although perhaps unsatisfying, statement that one can make about them is that they originate from the strong-field-induced

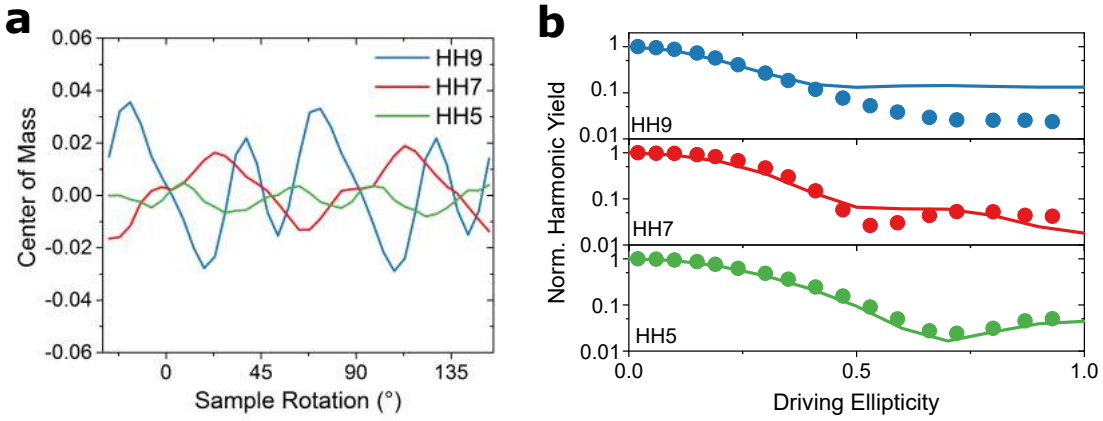

Figure 2.13: **a**: The center of mass curves of fig. 2.12. Adapted from [161]. **b**: Harmonic yields along $\theta = 0°$. Dots are measurements and lines TDDFT-calculations (by N. Tancogne-Dejean).

coupled intraband and interband dynamics. One should also mention that the asymmetry with respect to $\epsilon = 0$ only appears for $\theta \neq 0°, 45°, 90°, 135°$. These direction mark the major symmetry axes of the crystal and we would expect no difference in the response to ϵ and $-\epsilon$ along these directions.

It is interesting to note that for all harmonics the yield does not disappear with $\epsilon = 1$ but remains in the percent level, compared to linear excitation. The fact that there is still significant yield with $\epsilon = 1$ is consistent with earlier observations in solids [45, 147] but still astonishing, if one considers the recollision-type picture in gas HHG.

The white dotted lines in Fig. 2.12 are the center-of-mass curves (CoM) of the respective θ-dependent distributions (exaggerated in its proportions). Those are calculated using

$$\mathrm{CoM}(\theta) = \frac{\sum\limits_{|\epsilon|<0.5} \epsilon \cdot I_n(\epsilon, \theta)}{\sum\limits_{|\epsilon|<0.5} I_n(\epsilon, \theta)}, \tag{2.8}$$

where I_n is the yield of the respective harmonic order. The CoMs are calculated in an interval $|\epsilon| < 0.5$ to emphasize the asymmetric response in the most intense region of the ellipticity profiles. Fig. 2.13**a** shows the same CoM-curves plotted individually.

As said before, HH5 shows atomic-like behaviour and therefore does not exhibit strong asymmetries for any θ. This is different for HH7 and HH9. Importantly, for certain θ, the CoMs of HH7 and HH9 have different signs, implying that they are generated predominantly with different driving helicities. This is a strong indication for them being generated with different generation mechanisms. Indeed, it is hard to reconcile how the same generation mechanism can lead to those harmonics being generated more efficiently with differing driver helicities. Already in Refs. [104, 105] it was argued, that the JDOS is an important measure for the

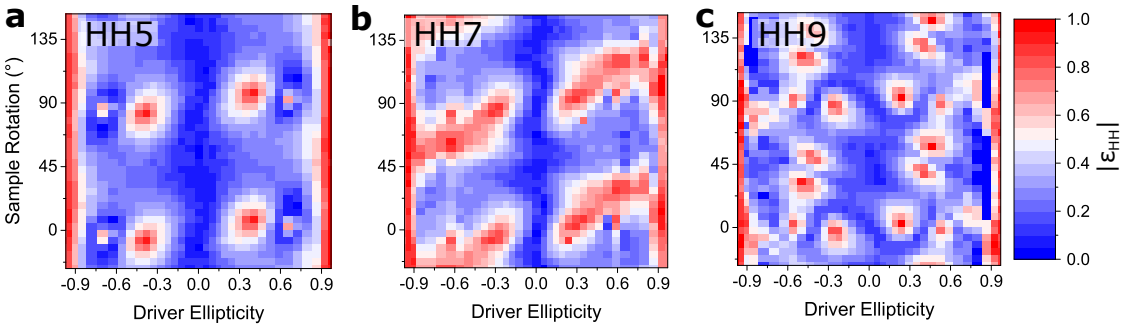

Figure 2.14: The absolute harmonic ellipticities of HH5-HH9 in dependence of ϵ and θ. As in Fig. 2.12, 0° refers to ΓX direction, 45° to ΓK. Adapted from [161].

relative magnitude of interband to intraband mechanism. Also, there it was shown that for the energy region of HH7, the JDOS is rather high, meaning that harmonic is generated by coupled inter- and intraband dynamics. The energy region of HH9 exhibits a relatively low JDOS, which implies that it is generated mainly by intraband dynamics. We will later discuss other manifestations of this but for now, let us note that we can see that HH7 and HH9 are generated in a different way and we can explain this by arguing with the JDOS. Note that CoM = 0 is required by mirror symmetry along the symmetry axes ΓX and ΓK and this is well reproduced in the data of Fig. 2.13**a**. Furthermore, the precise 90°-symmetry can count as a good sanity check for the validity of this dataset.

Fig. 2.13**b** shows the harmonic yields along sample rotation 0°, compared with the TDDFT-calculations of N. Tancogne-Dejean. Harmonics decrease with increasing ellipticity, however, HH5 and HH7 do not show a monotonic behavior. As it was the case in Sec. 2.2.2, simulations and measurements agree extremely well for HH5. For HH7 and HH9, some differences appear, however the major features seem to be reproduced, i.e. the rate of decrease of harmonic yield and the second plateau of HH7. As has been discussed in Sec. 2.2.2, it is clear that experimental data includes effects that are not integrated in the *ab-initio* description and that it is therefore not surprising to find deviations in quantitative comparisons like that. The qualitative features are well reproduced and that suffices to make predictions from these calculations.

2.3 Polarization-state-resolved high-harmonic analysis

After having investigated the dependence of the harmonics' yield on the driving ellipticity ϵ and sample rotation θ, it is time to add a level of complexity and rotate a polarizer for each ϵ and θ. This provides insights into the harmonics polarization states. The data resulting from these measurements can count as the main results of the corresponding publication [161].

Fig. 2.13 shows the absolute harmonic ellipticities $|\epsilon_n|$ versus ϵ and θ. These

maps are signatures of rich dynamics in the solids for a large variety of excitation conditions. We shall discuss them one after another. For linearly polarized excitation, harmonics are approximately linearly polarized. This might be intuitive and is definitely required by symmetry along the major symmetry axes ΓX and ΓK. For HH9 and excitation off a major symmetry axis (for instance around $\theta = -10°$ or $\theta = 22°$) it is slightly elliptically polarized.

For circularly polarized excitation, all harmonics become circularly polarized. For reasons of symmetry, this is independent of the sample rotation for a multi-cycle pulse. This is an extremely important result and when those measurements were firstly done [146], there was no experimental report on this behavior. It implies that one can take a cubic crystal, irradiate it with circularly polarized laser pulses and produce circularly polarized high harmonics - unthinkable in gas HHG. These types of harmonics will be further discussed in Sec. 2.3.1.

Perhaps most astounding are the features with $0 < |\epsilon| < 1$. Here, distinct driving conditions are observed for which the harmonics become circularly polarized. These features will be often called 'islands' over the course of this thesis. Again one can make out certain symmetry rules that stem purely from the cubic crystal class, as discussed in Sec. 2.2.3. Similarly high $|\epsilon_n|$ for elliptical excitation have been reported before from TDDFT-simulations (Fig. 7a of Ref. [105]). There however, they have been left mostly uncommented with the focus being on the generation of circularly polarized harmonics from circularly polarized drivers. Therefore, the observation that circularly polarized harmonic can be generated with elliptical excitation from solids can count as a surprising and important result of this work. This will be discussed in Sec. 2.3.2.

2.3.1 Circularly polarized driving pulses

Independently of the precise dynamics in the silicon crystal, circular harmonics from circular drivers (CHCD) could be expected in a broad sense by requirements of symmetry. The selection rules for circular polarization can be calculated quite easily for specific cases [141] and have been extended to arbitrary symmetry groups and higher harmonics by Tang *et al.* with group theoretical methods (see also Sec. 1.2.3). There, Tang *et al.* pointed out that for cubic systems, harmonics should all be circularly polarized with alternating helicities. Nevertheless, although obvious in a sense, this does not mean that the generation of circularly polarized harmonics is trivial or not worth being looked at. As argued in Sec. 1.1.4, there is great interest in generating circularly polarized high harmonics and the complexity of doing so in gases makes its solid HHG counterpart quite appealing.

Fig. 2.15**a** shows a polarizer scan of the three harmonics HH5-HH9 from silicon with circular driving excitation. For all harmonics there is almost no variation in intensity over polarizer rotation ξ. For reference, high harmonics have been generated with the same driving pulses but with a higher intensity of approximately $40\,\mathrm{TW\,cm^{-2}}$ from $50\,\mu$m-thin z-cut α-SiO_2 samples. A corresponding ξ-scan is shown in Fig. 2.15**b**, showing two harmonics from SiO_2. The trigonal symmetry group of SiO_2 allows for even harmonics to be generated, hence HH4 can be ob-

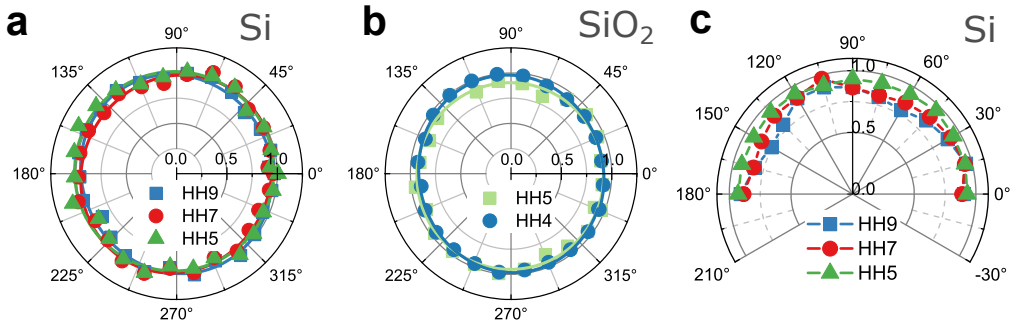

Figure 2.15: Polarizer scans of high harmonics from Si (**a**) and SiO_2 (**b**). Solid lines are $\sin^2$-fits. **c** shows $|\epsilon_n|$ (radial) from Si versus sample rotation (angle). In all figures, the driving pulses are circularly polarized. Adapted from [161].

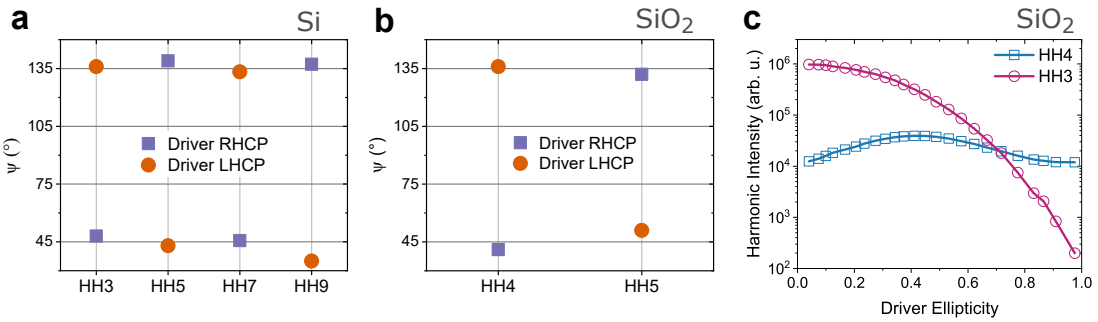

Figure 2.16: Observation of selection rules from Si and SiO_2 with circular excitation. The polarization rotation angle ψ following propagation of harmonics through a second QWP for the cases of HHG from Si (**a**) and SiO_2 (**b**). **c**: The harmonic yields of HH3 and HH4 from SiO_2 when going from linear to circular driver polarization. Adapted from [161].

served. The selection rules will be elaborated on below. Also here, both harmonics do not show any variation in intensity over ξ.

Fig. 2.15**c** shows another polar plot but this time it is not a ξ-scan. Here, the radial variable is $|\epsilon_n|$ and the sample rotation is the angular variable. For pulses that are at least a couple of cycles long, a rotation of the sample should not cause variations in $|\epsilon_n|$ or the harmonic yield when the driving pulses are circularly polarized. This is because there is no specific time where electrons are born because the magnitude of the electric field varies little over the course of a cycle. Then it does not matter if the sample is rotated, and all sample rotations should be equivalent (except for a phase shift, as is shown in the supplement of Ref. [147]). In Fig. 2.15**c** this is clearly visible in the form of very little variation of $|\epsilon_n|$ over 180°-variation of θ. Residual variation stems from the driving pulses not being perfectly circularly polarized, but instead $\epsilon \approx 0.97$ (see Sec. 2.1.5).

The selection rules of CHCD can be seen as conservation of spin angular momentum of light [147]. In cubic materials for instance, it is required by selection rules that the helicities of successive harmonics are alternating [105,147,148], mean-

ing successive harmonics rotate in opposite senses. One method to measure the helicity of a circular wave, relies on phase-shifting one polarization direction to the one perpendicular by $\lambda/4$. This is easy to see. In Jones calculus, a circularly polarized wave is written as

$$\mathbf{J}_{\text{circ}} = \frac{1}{\sqrt{2}} \begin{pmatrix} 1 \\ \pm i \end{pmatrix}. \tag{2.9}$$

The + sign (- sign) in front of the imaginary unit is applied for left handed (right handed) polarization. Using the Jones matrix for a QWP with fast axis along the x-axis:

$$\hat{\mathbf{J}}_{\text{qwp}} \cdot \mathbf{J}_{\text{circ}} = \frac{e^{-i\pi/4}}{\sqrt{2}} \begin{pmatrix} 1 & 0 \\ 0 & i \end{pmatrix} \cdot \begin{pmatrix} 1 \\ \pm i \end{pmatrix} = \frac{e^{-i\pi/4}}{\sqrt{2}} \begin{pmatrix} 1 \\ \mp 1 \end{pmatrix}. \tag{2.10}$$

Thus, the resulting wave will be linearly polarized and its polarization axis ψ will be rotated to the x-axis by 45° or −45° depending on its initial helicity. On the experimental side, a QWP that works sufficiently for the wavelength range of observed harmonics (700 nm to 230 nm) could not be found. Therefore, in these experiments a tunable QWP from *Alphalas* made of α-BBO has been used. It is not a broadband QWP by itself, but the mount of this QWP allows tilting the angle of incidence, thereby optimizing the QWP for different wavelengths. In Fig. 2.16**a** and **b**, this procedure has led to the measurement of ψ, the polarization-axis rotation angle with respect to the x-axis. There, one can see, that successive harmonics are indeed counter-rotating.

While selection rules of cubic materials require odd harmonics to have alternating helicities, the symmetry group of SiO_2 requires 2 of 3 harmonics to exist with alternating helicities [148]. Every third harmonic disappears when going from linear to circular polarization. This is confirmed experimentally in Fig. 2.16**c**, where the yield of HH3 drastically decreases with increasing ϵ. In total, the yield diminishes below the noise floor after a reduction of four orders of magnitude going from linear to circular driving polarization, unambiguously confirming the selection rules.

Another interesting thing to note from Fig. 2.16**c** is that the yield of HH4 does not decrease with elliptical or even circular driving polarization. In fact, it even increases, peaking around $\epsilon \approx 0.4$. The yield with $\epsilon = 0$ and $\epsilon = 1$ is equal. A similar behavior has also been observed by Saito *et al.* from GaSe [147]. This raises interesting questions because from gas HHG one would always expect the harmonic yield to decrease with increasing ϵ. One possible explanation could lie in the intraband mechanism dominating the harmonic emission process in these cases. Here, electrons and holes do not need to overlap again and therefore the yield does not necessarily decrease with increasing ϵ. For the case of SiO_2 this is a likely explanation because these harmonics are far below the band gap of 9.2 eV. It should however be mentioned that at this point it has not been confirmed generally that the interband mechanism diminishes the yield with elliptical excitation. In that

case the precise behavior is unclear because holes are mobile too and electrons can re-encounter holes from neighbouring atomic sites [90]. Both these circumstances should affect the recombination probability differently than in the gas HHG case but should also be band-structure dependent.

It should be pointed out that the observation of a constant harmonic yield over polarizer rotation ξ is no unambiguous proof of circular polarization. In principle, harmonics could be fully unpolarized and in such a ξ-scan, one would not notice. To fully characterize the polarization states of CHCD, a characterization of the Stokes parameters is performed in Sec. 2.3.3.

2.3.2 Elliptically polarized driving pulses

While CHCD can be fully explained by arguments of symmetries and do not seem to depend so much on the exact dynamics of the system, we should investigate the high-harmonic response to elliptical driving polarization deeper. In this case, symmetry arguments did not make corresponding predictions and it will be shown in this section, that circular harmonics from elliptical drivers (CHED) stem from the microscopic strong-field dynamics and not from symmetry alone. Unless otherwise noted, the 2 μm-thin (100)-cut Si samples are used. Additionally, this section contains some TDDFT-simulations performed on a Si unit cell by N. Tancogne-Dejean (as described in Sec. 2.2.2).

With elliptically polarized drivers one can observe well defined driving conditions to generate circularly polarized harmonics. Perhaps even more astoundingly, these conditions are different for every harmonic order. While HH5 exhibits only one island of $|\epsilon_5| \approx 1$ in the range of $0 < \epsilon < 1$ and $0° < \theta < 90°$, HH9 shows at least four (compare Fig. 2.14). The shape of HH7 in the map of Fig. 2.14 looks systematically different with much more elongated regions of $|\epsilon_7| \approx 1$, compared to HH5 and HH9. While N. Tancogne-Dejean *et al.* already predicted that individual harmonic orders would respond differently to elliptical driving excitation [105], this is the first experimental observation of such a behavior. Fig. 2.17 shows an examplary polarizer scan with fixed driving conditions. All harmonics have different polarization states simultaneously, with HH9 being linearly, HH7 elliptically and HH5 circularly polarized.

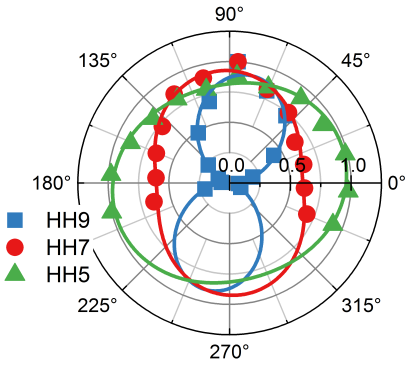

Figure 2.17: A polarizer scan with $\epsilon = 0.4$ and $\theta = \Gamma X + 5°$.

It is interesting to track the evolution of the polarization states for fixed θ but varying ϵ. As stated before, for linearly polarized drivers, harmonics are mostly linearly polarized, while for circularly polarized drivers, harmonics are circularly

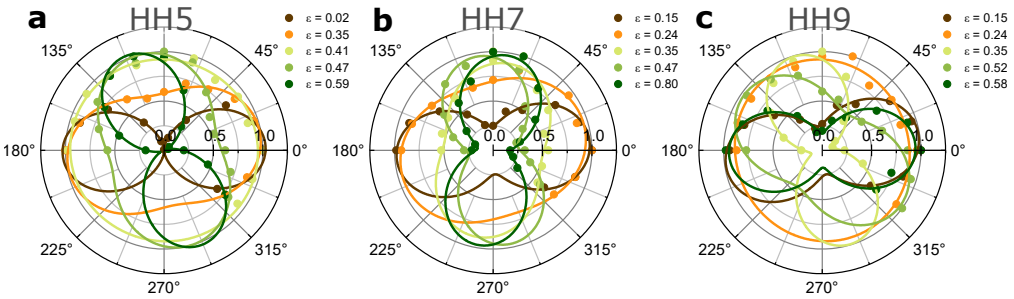

Figure 2.18: Polarizer scans of HH5-HH9 for different ϵ showing cases of CHED. **a**: $\theta = \Gamma X + 8°$; **b**&**c**: $\theta = \Gamma X + 3°$.

polarized. CHED therefore naturally implies that the polarization states vary in between $\epsilon = 0$ and $\epsilon = 1$ in a unique way. To get an impression of this, Fig. 2.18 shows polarizer scans of HH5-HH9 for fixed θ but varying ϵ. First, let us discuss Fig. 2.18**a** in detail. For close-to-linear excitation ($\epsilon = 0.02$), HH5 is linearly polarized along the x-axis, which is parallel to the driving field. With increasing ϵ, $|\epsilon_5|$ increases too, until, for $\epsilon = 0.41$ it is almost perfectly circularly polarized[†]. Interestingly, for higher ϵ, the harmonic becomes linearly polarized again, however with its polarization axis rotated by approx. 110°. In a sense, the harmonics' behavior can be understood as an increase of the perpendicular component with increasing ϵ to a point where the perpendicular component dominates the parallel component, causing the major axis to rotate. The conditions for which the harmonic is circularly polarized is the crossover point of equal intensities of parallel and perpendicular component. These characteristics will be investigated in-depth in the calculations of Chapter 3.

The depicted cases of HH7 and HH9 are similar. For HH9 (Fig. 2.18**c**), there is a slight modification, since it seems to have two of the previously mentioned crossover points. It becomes circularly polarized for $\epsilon = 0.24$ and then almost circularly polarized again for $\epsilon = 0.52$. For the values in between it undergoes rotation, as can be seen from $\epsilon = 0.35$, where it is rotated with respect to the driving field, while for $\epsilon = 0.58$, it is parallel to the driving field again. Note also the different ranges of ϵ in Fig. 2.18. For HH9, driving conditions for CHED are much more sensitive than for HH5.

The close collaboration with our theory partner, N. Tancogne-Dejean, provides unique possibilities to cross check the validity of the results on the one hand and to explore further predictions on the other. The harmonics' ellipticity as well as the harmonics' major-axis rotation have been measured along $\theta = \Gamma X$ and compared with the corresponding TDDFT-calculations (see Fig. 2.19). At this point, one should strongly emphasize the *ab-initio* character of these simulations. There are no free parameters to input in the calculations, as it is often done in this field (e.g. the number of bands). Keeping this in mind, experiment and theory

[†]Let us keep in mind that these kind of polarizer scans are not *actually* a proof of circular polarization due to ambiguities with unpolarized light. We will need to assess to degree of polarization later on in Sec. 2.3.3.

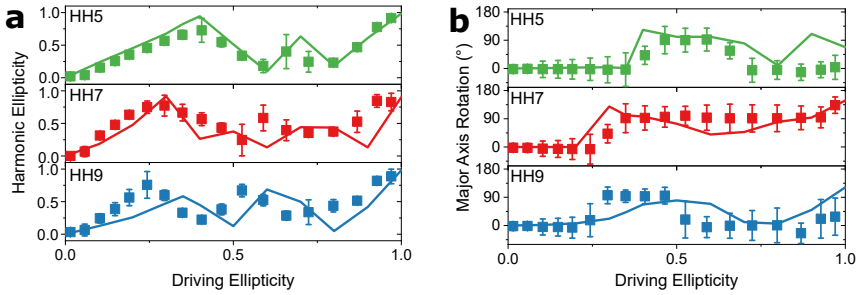

Figure 2.19: $|\epsilon_n|$ (**a**) and harmonics' major axis rotation (**b**) along $\theta = \Gamma X$. The solid lines are TDDFT-calculations performed by N. Tancogne-Dejean. For all plots, the values are interpolated between $\theta = \Gamma X + 2°$ and $\theta = \Gamma X - 3°$ and averaged over positive and negative ϵ values. The error bars are the averaged absolute deviations.

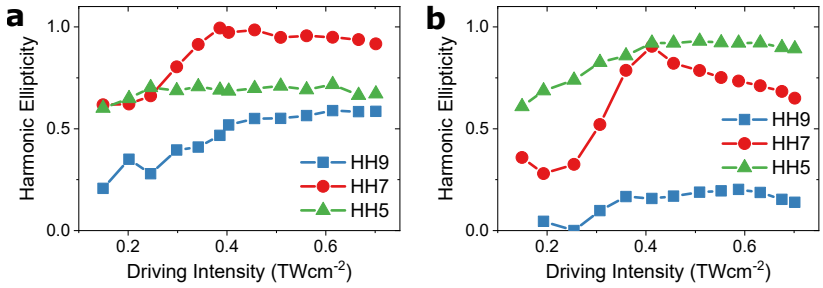

Figure 2.20: Measurements of $|\epsilon_n|$ for fixed ϵ and θ, but varying driving field intensities. **a**: $\epsilon = 0.4$, $\theta = \Gamma X + 10°$; **b**: $\epsilon = 0.3$, $\theta = \Gamma X + 15°$

match very well. The previous observation that HH5 fits best continues to be true here. However, the other harmonics are well captured too. Even the double-island structure of HH9 appears both in experiments and theory in Fig. 2.19**a**, although there, the absolute positions are slightly off. The rotation of the major axis was an effect previously not mentioned at all but also there, experiment and simulations fit very well.

Since these calculations only take microscopic effects into account, the agreement to experiments is a good indication that the experimental results are not produced by some parasitic phenomena. One could for instance think of surface or nonlinear propagation effects (e.g. induced birefringence) or artifacts (e.g. doping or strain) of the acquired samples. The agreement to the calculations implies that the here discovered phenomena are directly linked to the strong-field-driven charge dynamics inside the crystal.

While CHCD could be perfectly deducted from symmetry arguments, the question arises how and if this is also the case for CHED. While of course the individual islands in the ellipticity maps in Fig. 2.14 reproduce the crystal symmetries (four-fold symmetric, etc.), it should be investigated if also the position of the islands itself can be explained by symmetry. One way of doing so is by studying the intensity dependence of the CHED. This has been done in Fig. 2.20, where for fixed

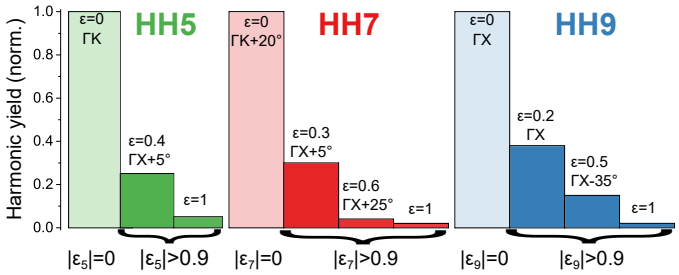

Figure 2.21: Harmonic yields for HH5-HH9 for cases of circular polarization. The yields are normalized to the linear case with $\epsilon = 0$ (indicated by the light colors). Adapted from Ref. [161].

ϵ and θ the driving intensity was varied and $|\epsilon_n|$ was measured. It is apparent that $|\epsilon_n|$ is dependent on the intensity for all harmonic orders. Most variation can be found for HH7 in these plots, which varies from $|\epsilon_7| \approx 0.25$ to $|\epsilon_7| \approx 0.9$ in Fig. 2.20**b**. Symmetry arguments alone could not be used to explain this behavior since no symmetry is changed when varying the intensity. This indicates again that the polarization states of high harmonics emitted with elliptically polarized driving pulses are a direct consequence of the strong-field-driven dynamics in the system. It shows also that besides ϵ and θ, also the driving intensity plays a crucial role in the high-harmonic response from solids. This is obvious in a sense, since the electrons can be driven to completely different regions in the Brillouin zone for higher intensities. This could for instance trigger the transition to a higher-lying conduction band or lead to some strongly changed curvature of the populated conduction band. As argued before, HH7 is generated by coupled interband and intraband dynamics. It is interesting that this is the harmonic that shows the most variation in Fig. 2.20, while for the intraband-only harmonics HH5 and HH9 the variation is not so significant. One could speculate that sudden changes of the JDOS can arise when electrons reach different **k**-values in the Brillouin zone and that this could give rise to the observed change in $|\epsilon_n|$ with intensity. This would of course be especially important for the interband mechanism and hence HH7 in this case. But further data would be needed to verify this hypothesis. In any case, as will be shown in Sec. 3.3, the harmonics' polarization states are also dependent on the intensity when only considering intraband dynamics.

An interesting property of CHED at least from silicon is its relatively good efficiency. In silicon, since the yield of the harmonics overall decreases with increasing driving ellipticity, generating circularly polarized harmonics with $\epsilon = 1$ causes the yield to decrease to the percent level, compared to linearly polarized harmonics (see Fig. 2.21). With elliptically polarized drivers, the yield does not decrease so much. In the most extreme case observed here, the yield of circularly polarized harmonics can be boosted up to 20x when generating HH9 with $\epsilon = 0.2$ instead of $\epsilon = 1$.

2.3.3 Stokes parameters

As mentioned repeatedly throughout the last sections, measuring no intensity variation over rotation of a polarizer does not unambiguously proof circular polarization of the investigated light wave. It could also be fully unpolarized or elliptically polarized with a major-axis rotating over the course of a pulse. This is an important point. Taking the intensity dependence of $|\epsilon_n|$ into account (compare Fig. 2.20), it can be expected in a sense that the polarization states of the emitted harmonics change over the course of the pulse. The next step is therefore to take a closer look at the degree of polarization of CHCD and CHED.

The classic method to characterize the full polarization state of a light wave is by means of the Stokes parameters - a set of four parameters that Stokes introduced in 1852 [165]. They are [160]

$$S_0 = E_{0x}^2 + E_{0y}^2 \tag{2.11a}$$
$$S_1 = E_{0x}^2 - E_{0y}^2 \tag{2.11b}$$
$$S_2 = 2E_{0x}E_{0y}\cos\delta \tag{2.11c}$$
$$S_3 = 2E_{0x}E_{0y}\sin\delta. \tag{2.11d}$$

E_{0x} and E_{0y} are the amplitudes of the fields' x- and y-components and δ is their relative phase. The Stokes parameters can be measured with a polarizer and a device introducing a $\pi/2$ phase shift between x- and y- component (for instance a Fresnel rhomb or a QWP). Let $I(\alpha, \beta)$ be the detected intensity behind a polarizer with angle α and an introduced phase shift between x- and y- component of β. Then [160]

$$S_0 = I(0,0) + I(\pi/2,0) \tag{2.12a}$$
$$S_1 = I(0,0) - I(\pi/2,0) \tag{2.12b}$$
$$S_2 = 2I(\pi/4,0) - S_0 \tag{2.12c}$$
$$S_3 = S_0 - 2I(\pi/4,\pi/2). \tag{2.12d}$$

Often the parameters S_1 to S_3 are normalized by S_0, because it is just the total intensity. Then all Stokes parameter S_1/S_0, S_2/S_0 and S_3/S_0 range from -1 to 1. One can describe S_1 as the degree of linear polarization in the x- and y-direction, S_2 as the degree of linear polarization in the 45°- and 135°-direction and S_3 as the degree of circular polarization (with its sign noting the helicity). All parameters except S_3 can be measured without an additional QWP (or Fresnel rhomb) by simply rotating a polarizer. This is what has been done so far throughout this thesis. The degree of polarization (DoP) however, requires knowledge of S_3:

$$\mathrm{DoP} = \frac{I_{\mathrm{pol}}}{I_{\mathrm{tot}}} = \frac{\sqrt{S_1^2 + S_2^2 + S_3^2}}{S_0}, \quad \mathrm{DoP} \in [0,1]. \tag{2.13}$$

Fig. 2.22 shows the Stokes parameters S_1, S_2 and S_3 as well as the DoP with circular driving polarization for varying sample rotations. We see that S_1 and S_2

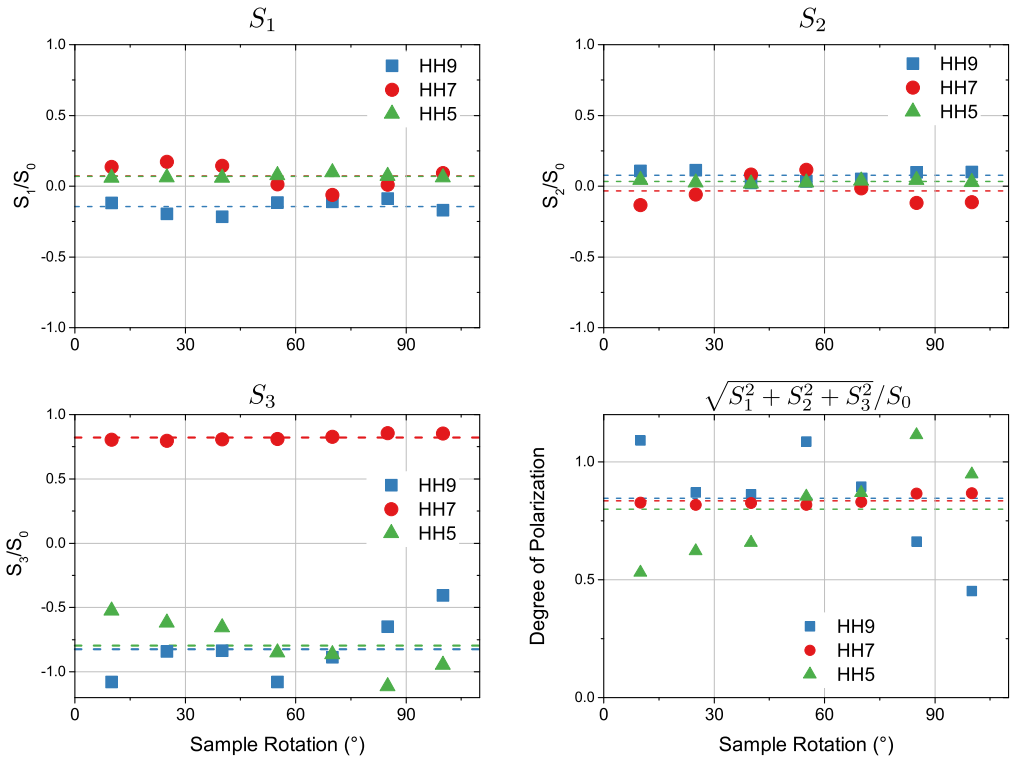

Figure 2.22: Stokes parameters and DoP for variation of θ with $\epsilon = 0.98$. Dashed lines indicate the mean values. From Ref. [161].

are close to zero for all harmonics while $|S_3|/S_0 \approx 1$. The different signs of S_3 reveal the opposite helicities as they already have been discussed in Sec. 2.3.1. The DoP shows mean values around 0.8 for all harmonic orders. The variations over sample rotation are an indication for the error bars of this measurement, since there should not be any variations. Of course also the values of $|S_3|/S_0 > 1$ or the DoP > 1 link to uncertainties in the measurements. The variation comes from not having perfectly circular driving pulses as well as significant introduced errors by the measurement of the Stokes parameters (discussed below). DoP ≈ 0.8 implies that harmonics are highly polarized. Compared to HHG in gases and molecules, the reported values of the DoP are of similar magnitude [31, 166].

The Stokes parameters for the case of varying driver ellipticities along a fixed sample rotation are shown in Fig. 2.23. Here, two independent measurements have been performed from each harmonic order in order to at least grasp the error of these measurements. Additionally, the Stokes parameters of the driving pulses have been measured. In S_3, one can see that both harmonics become circularly polarized for $\epsilon \approx 0.2$ and also for $\epsilon \approx 0.6$. Interestingly, in between, the sign of S_3 changes which means that the helicity reverses with elliptical excitation already. This is best understood as a monotonic increase of the relative phase δ, thereby flipping the helicity when surpassing $\pi/2$. For $\epsilon > 0.6$ the sign of S_3 changes again for HH9, while it stays negative for HH7. Also the major-axis rotation in between the two islands of high $|S_3|$ can be found in these scans: For $\epsilon \approx 0.4$, S_2 is positive

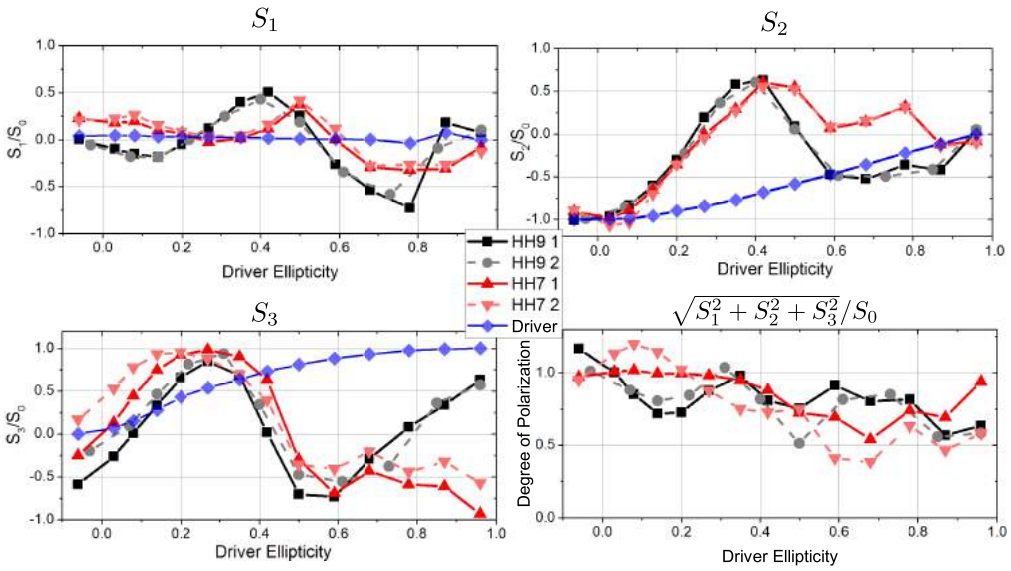

Figure 2.23: Stokes parameters and DoP versus driving ellipticity ϵ for sample orientation $\theta = \Gamma X - 5°$. Two independent measurements denoted by 1 and 2 are shown. From Ref. [161].

for both harmonics and also S_1 has a relatively high value, indicating a rotation by more than 90° in space, which has been observed and described in Fig. 2.18. The DoP seems to constantly decrease in these measurements with increasing ϵ, however it almost always stays above 0.5. Also here, large variations are apparent due to uncertainties in the measurement. In this case they clearly stem from the method of determining S_3.

As can be seen from Eqs. 2.12, the Stokes parameters are in this case calculated with a set of only four measured values. While this might not be a significant issue for S_0, S_1 and S_2, especially S_3 suffers from this. Here, one introduces a QWP into the beam which, even without any phase retardation already affects the transmitted beam by absorption, reflection and also by misalignment if the QWP is not inserted at exactly 0° angle of incidence. The tunable QWP actually relies on tuning the angle of incidence in order to achieve a $\pi/2$ phase shift for different wavelengths, which complicates things further. Although the effects of reflection and absorption have been calibrated and taken into account in these measurements, significant uncertainties remain. A better way to measure the Stokes parameters has been proposed in Ref. [167]. Here, the pulse under test is sent to a rotating QWP and transmitted through a stationary polarizer behind. Behind the polarizer, the intensity of light is measured. The detected intensity variations over QWP rotation can be fitted and all four Stokes parameters can be retrieved from that fit. The usage of multiple data points at once and not having to change the setup to measure S_3 increases the accuracy. This measurement technique is not possible with the tunable QWP that has been used here and also with a Fresnel rhomb it turned out to be extremely challening due to the length of the Fresnel rhomb and the requirement to rotate in the same axis as the laser propagates (the Fresnel

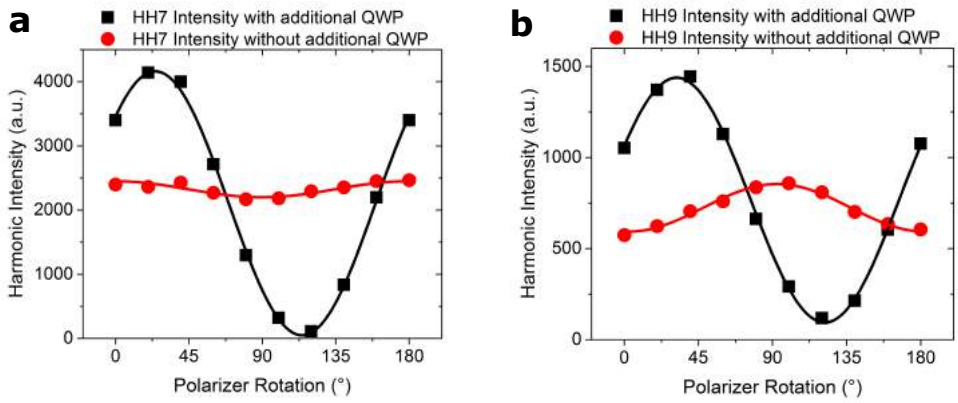

Figure 2.24: Polarizer scans showing circularly polarized harmonics that are converted to linear polarization with a second QWP. **a**: $\epsilon = 0.3$, **b**: $\epsilon = 0.6$. $\theta = \Gamma\text{X} - 5°$ in both cases. Solid lines are $\sin^2$-fits. Adapted from Ref. [161].

rhomb used here had a length of 90 mm).

In any case, while certainly not the most precise measurements, Figs. 2.22 and 2.23 show that harmonics are highly polarized and that there are interesting changes in the helicity of the harmonics with varying ϵ. These are the first measurements of Stokes parameters for HHG from solids and improvements of the method are likely to bring new insights into the strong-field-driven charge dynamics in solids.

While the Stokes parameters might be a little unintuitive, the measurements that it requires show in a very direct way what it means to have a highly polarized light wave. Fig. 2.24 depicts two cases of CHED for HH7 (**a**) and HH9 (**b**). Inserting a QWP converts this circular wave into a linear one (as described in Sec. 2.3.1) if and only if the initial wave is really circularly polarized. Any depolarized component or polarization state that changes over time would not be converted to a linear wave. Fig. 2.24 shows therefore a convincing visual proof for the high polarizability of the here measured CHED.

2.3.4 Vectorial field reconstruction of a circularly polarized harmonic from Si

The aim of this section is to temporally characterize a third harmonic generated nonperturbatively from Si with circularly polarized driving pulses. Temporal characterization of a generated high harmonic faces the general problem that harmonics are on the pJ-level in terms of their pulse energy, which is too weak for self-referencing techniques that require the pulses to trigger non-linear effects, for instance in FROG. Additionally, the reconstruction of pulses that are not linearly polarized is challenging by itself, particularly because of the polarization-sensitive $\chi^{(2)}$ in typical non-linear crystals like BBO. The characterization technique utilized here is two-dimensional spectral shearing interferometry (2DSI) [169, 170] which

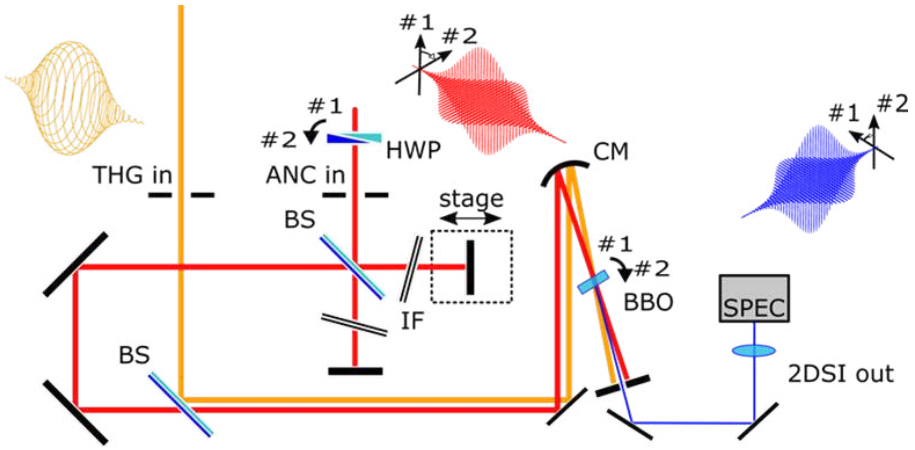

Figure 2.25: Experimental setup to retrieve the two dimensional temporal profile of HH3. THG: HH3, BS: beam splitter, IF: interference filter, ANC: ancillery pulse, CM: curved mirror, BBO: barium borate crystal, SPEC: UV-NIR Spectrometer. Adapted from Ref. [168].

provides the possibility to boost the weak harmonic signal with a strong pulse (for instance the laser pulses directly) via sum frequency generation (SFG). This section has been realized in very close collaboration with F. Scheiba who was particularly responsible for the experimental part but also contributed significantly to the data analysis and interpretation.

In 2DSI, a pump pulse is copied into two replicas (or ancillae) with the help of a Michelson interferometer. Both of these replicas pass through narrowband filters that are slightly detuned to each other (806 nm and 808 nm in this case). The ancillae are then overlapped with the pulse under test in a non-linear medium (e.g. a BBO) upconverting the pulse under test by means of SFG. Temporally delaying one ancillery pulse to the other generates an interference pattern in the spectral domain of the upconverted signal. When considering the shear frequency between the ancillae pulses, this interference pattern encodes the group delay and thus the sought-after spectral phase. For a detailed discussion, the reader is advised to look at Refs. [169–171]. Here, as ancillae, a portion of the Ti:Sapphire pulses is used that also pumps the OPA. As a nonlinear medium we use a type-II 20 μm-thin BBO crystal, cut at an angle of $\theta = 44°$.

Harmonics are generated with a circularly polarized driver and are therefore also circularly polarized. It is not possible to phase match both polarization components at the same time in a crystal that relies on birefringent phase matching. Since we use a type-II BBO, only polarization components perpendicular to another can be phase matched. Therefore, the upconverted polarization direction of HH3 can be selected by flipping the polarization of the ancillae pulses with a HWP at the input of the 2DSI setup. p- and s-components of HH3 are then measured separately in the 2DSI and also their temporal profiles are reconstructed individually. To add the two temporal profiles together, the remaining free parameters are the relative amplitudes E_{0x} and E_{0y} as well as their relative delay. These three

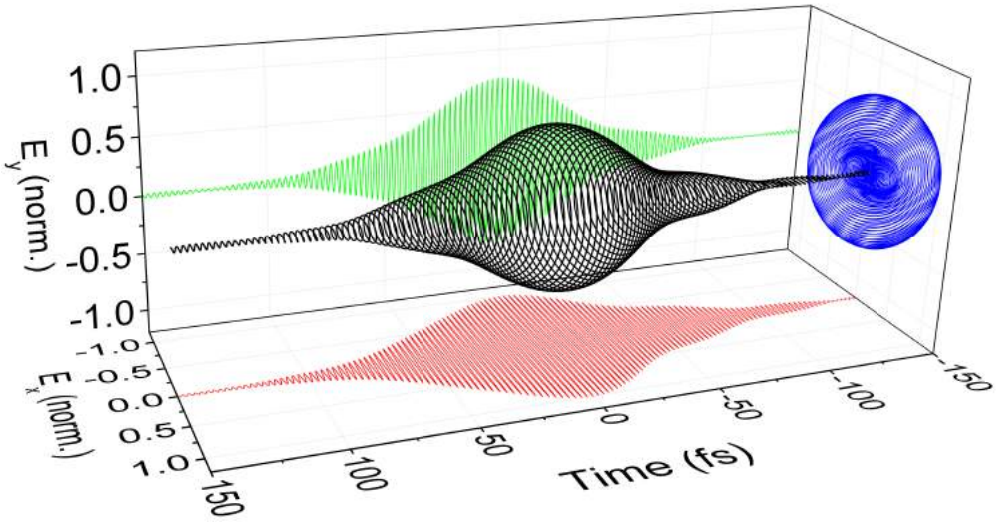

Figure 2.26: 2DSI measurement and its corresponding projections of HH3 when generated with circularly polarized driving pulses. Adapted from Ref. [161].

parameters can be retrieved from an independent measurement that is taken by inserting a polarizer behind the sample and guiding the harmonics to an additional spectrometer with a flip mirror. Rotation of the polarizer lets one retrieve the polarization ellipse of the harmonics, as has been done throughout this chapter. The relative phase can be determined with [160]

$$\delta = \arccos\Big(\frac{\tan(2\psi)(E_{0x}^2 - E_{0y}^2)}{2E_{0x}E_{0y}}\Big), \tag{2.14}$$

where ψ is the rotation of the major axis. δ varies over the spectrum of HH3. By comparing to the instantaneous frequencies of the two temporal reconstructions, δ has been determined for an instantaneous frequency 20 fs before the center of the pulse. This choice is arbitrary and could have been any other instantaneous frequency. The reconstructed temporal profiles of p- and s- components are delayed by the time that corresponds to δ at this frequency. One can then produce a figure like Fig. 2.26 which shows the measured electric field of the circularly polarized HH3.

Since 2DSI is not sensitive to the CEP, the CEP of the x-component is set arbitrarily to 0 in this case. For multicycle pulses like the one here, the CEP does not significantly influence the pulse shape. Another ambiguity of this method is a 2π-uncertainty of δ. However it seems unlikely that one component would be delayed so much from the other without any major effects of birefringence.

The FWHM pulse durations of the x- and y-components are 61 fs and 50 fs respectively. From perturbative nonlinear optics, one would expect an $n^{-1/2}$-dependence of the pulse duration, where n is the harmonic order. Here, the pulse duration is 70 fs and $70\,\text{fs}/\sqrt{3} = 40\,\text{fs}$. In order to guide the harmonics to the BBO, they are reflected from in total 6 UVAl-mirrors. These reflections affect the

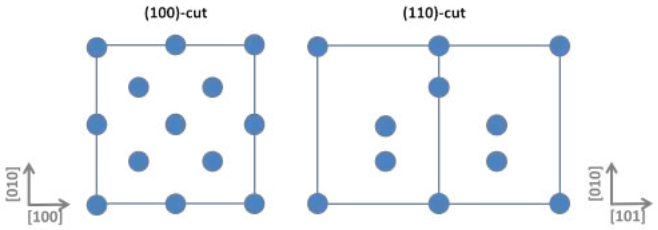

Figure 2.27: Comparison of the (100)- and (110)-planes of a diamond cubic unit cell. The blue dots mark atoms.

phases of x- and y-components differently which could alter the measured pulse durations. Perhaps more important than the measurement of the harmonics pulse duration is that the technique introduced in this section allows to track the polarization state of an harmonic over the course of the pulse. This method would be sensitive to abrupt changes of the polarization state as they have been predicted theoretically [105,172]. This is not observed for the case of CHCD HH3 however it would be interesting to do similar measurements with higher harmonics and with elliptically polarized excitation. Detection of higher harmonics turned out to be very challenging in our case, especially due to their low pulse energies. However, with further improvements of this setup (e.g. by increasing the pump energy or the high-harmonic pulse energies), this should be possible and could reveal signatures of otherwise hardly accessible ultrafast electron dynamics.

2.4 Polarization maps of other materials

After having established polarization-state-resolved high-harmonic spectroscopy mainly of (100)-cut silicon, it is essential to do similar polarization scans of other materials. It is clear that the high-harmonic response is greatly dependent on the system in which the strong-field dynamics take place. Without doing further measurements on other systems, it is absolutely unclear if effects like CHED are uniquely linked to (100)-cut silicon or if it can also be found from other systems. In this section, three different systems will be investigated. None of which will be looked at as closely as it has been done from (100)-cut silicon, although the ZnS measurements at the end of this section will be compared to simulations in Chapter 3 and thus also plays a vital role in the sections to come.

2.4.1 (110)-cut Si

The (110)-cut silicon provides an interesting geometry because any major symmetry direction of Si can be accessed when rotating the sample along the laser propagation axis, i.e. [100], [110], [111]. This comes at a cost however, because this cut reduces the symmetry in the polarization plane of the laser. As Fig. 2.27 reveals, this cut is not four-fold symmetric anymore. In fact, only one axis remains

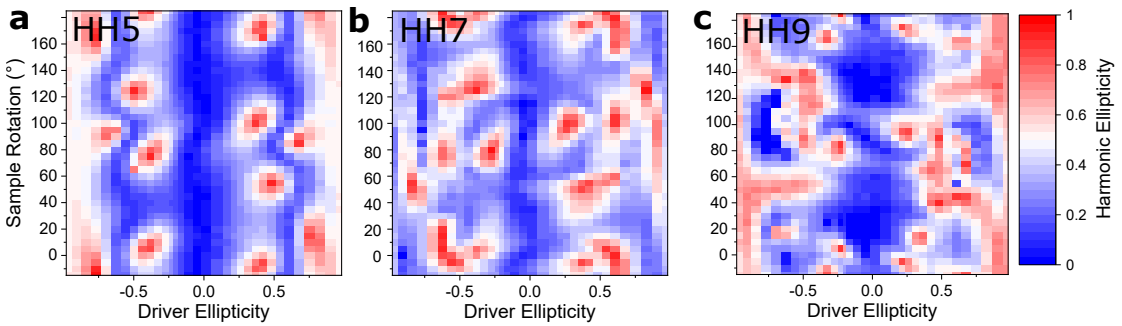

Figure 2.28: Ellipticity maps from (110)-cut silicon.

inversion symmetric and that is [010], i.e. the vertical direction in the sketch of Fig. 2.27. The sample used here is from Norcada and 5 μm thin.

As from the (100)-cut, the ellipticity maps of Fig. 2.28 show distinct features in the responses of the harmonics to elliptical excitation. Once again, for all harmonics, islands of CHED appear for various driving conditions. From these islands one can make out certain symmetry directions. For instance, around $\theta = 90°$ seems to be a mirror-symmetric axis, i.e. $(90° - \theta, \epsilon) = (90° + \theta, -\epsilon)$. The same is true for $\theta \approx 0°$ which makes sense, given the 90° rotation between [010] and [101]. Lingering on the topic of symmetry for a little longer, one notices that harmonics do not generally become circularly polarized for the highest ϵ. This is indeed an interesting feature and a consequence of (110)-cut Si not being four-fold symmetric anymore. Different strengths of nonlinearities in perpendicular directions convert the circularly polarized driving field into elliptically polarized harmonics. In terms of selection rules, the derivations in Ref. [148] do not apply here anymore. This is because they have the underlying assumption that the laser propagates along the axis with highest rotational symmetry. That is not the case here since the highest rotational symmetry axis for a cubic system lies perpendicular to the (100)-plane.

2.4.2 (0001)-cut ZnO

ZnO has been the first material to detect nonperturbative HHG from solids from [38] and has since then been studied extensively both experimentally and theoretically (see, e.g., Refs. [39, 91, 96, 173, 174]). The development of the solid HHG version of the three step model mostly revolved around HHG from ZnO because of its relatively simple band structure in which the lower conduction band is well isolated from the others. However it should be mentioned that ZnO has multiple valence bands overlapping at the Γ-point [175] which could complicate things if one was to consider valence band dynamics. ZnO is probably the material that has the most publications on solid HHG so far. It is therefore important to transfer the here introduced spectroscopic technique to ZnO.

In these experiments, a 50 μm-thin (0001)-cut ZnO sample from *SurfaceNet* was used. The peak intensity was similar than in the Si case, i.e. 0.7 TW/cm^2. The surface quality of the sample was rather poor, meaning that the yield fluc-

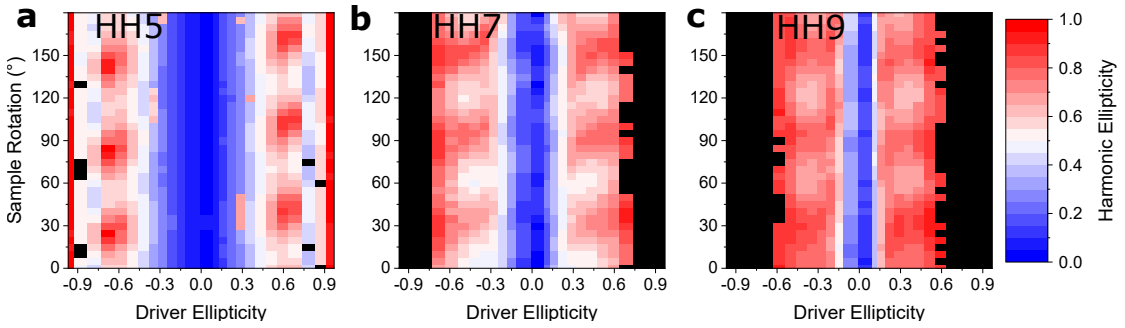

Figure 2.29: Ellipticity maps from (0001)-cut ZnO. Data points where the signal to noise ratio is below 2.57 times the standard deviation of the noise floor are marked in black.

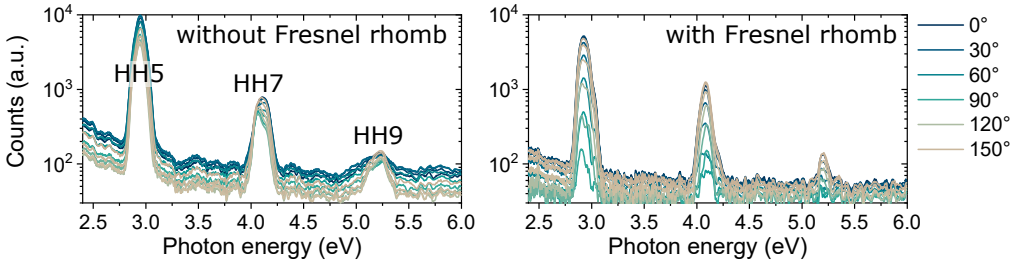

Figure 2.30: Spectra from ZnO with and without inserted Fresnel rhomb behind the sample. The differently colored spectra are for different polarizer rotations, as indicated in the legend. Here, $\epsilon = -0.45$ and $\theta = 90°$.

tuated significantly from one spot to the next. This behavior is not really seen in the ellipticity maps in Fig. 2.29, which implies that the harmonics' ellipticity is somehow less dependent on the exact surface structure of the sample than the yield.

The ellipticity maps in Fig. 2.29 show important differences to the results from Si. First of all, the maps are 60°-periodic. This is not surprising since (0001)-cut ZnO has a hexagonal symmetry. Second, again CEHD can be found for any harmonic order. However, while HH5 shows somewhat distinct islands, the higher harmonics HH7 and HH9 do not. Those harmonics seem to become circularly polarized for very low driving ellipticities ϵ. Furthermore, the ellipticities of those harmonics change very little with varying θ or ϵ. It is interesting to note that HH5 is below the band gap of ZnO while HH7 and HH9 are above. ZnO has been repeatedly argued to be a material for which interband dynamics are dominating high-harmonic emission [91]. In Fig. 2.29 data points are blackened for which the signal to noise ratio of the harmonics is below 2.57 times the standard deviation of the noise (99% confidence interval). It is clear that HH7 and HH9 disappear for large ϵ. This has been observed already in Ref. [38].

To confirm the degree of polarization of the harmonics, a Fresnel rhomb has been inserted between the sample and polarizer, that converts the polarization

states of the harmonics as described in Sec. 2.3.1 and Sec. 2.3.3[‡]. Fig. 2.30 shows spectra for different polarizer rotations both for the case without a Fresnel rhomb between sample and polarizer (left) and for the case of an inserted Fresnel rhomb between sample and polarizer (right). While the spectra without additional Fresnel rhomb show very little variation over polarizer rotation, the inserted Fresnel rhomb causes heavy modulation on all harmonics simultaneously (consider the logarithmic scale), verifying that harmonics are highly polarized in this case. It is indeed captivating that especially HH7 and HH9 are circularly polarized for such a broad range of ϵ and θ. Intuitively, this behavior is hard to comprehend with the two-band single-particle model that has been used so often to describe HHG from ZnO. To deepen our understanding on solid HHG, it might help to search for a description that can explain the polarization-state-resolved ellipticity response from ZnO.

2.4.3 (100)-cut ZnS

The next and last sample of this section is 50 μm-thin, (100)-cut ZnS. The driving peak intensity in these experiments is approximately 0.4 TW/cm^2. ZnS has a zinc-blende crystal structure which resembles the diamond cubic crystal structure of Si, but consists of two different kind of atoms. This means, it is not 90°-periodic but we can find the same symmetry rules that we identified for (110)-cut Si in Sec. 2.4.1. Here a symmetry axis is around $\theta \approx 100°$. The broken inversion symmetry of ZnS manifests itself in the generation of even harmonics. ZnS has been chosen here because it has, somewhat similarly to ZnO, a well isolated conduction band from the higher lying bands. Nevertheless, this band shows interesting distinct features. Due to this, ZnS will be used as a reference in Sec. 3.3 to compare the intraband-only simulations to. The spectral region of HH6 overlaps with the band gap, meaning HH4 and HH5 are below while HH7 is above the band gap.

The polarization-state-resolved high-harmonic response to elliptical excitation of ZnS differs yet again from the previously discussed materials. The differences between the odd harmonics HH5 and HH7 are somewhat similar to the behavior of HH5 and HH7 in (100)-cut Si. HH5 shows distinct islands of high $|\epsilon_5|$ while these conditions are much less sensitive for HH7, which shows a more continuous structure in high $|\epsilon_7|$. It is interesting to note that HH5 is below and HH7 above the band gap. Also for Si, HH7 was generated by intraband and interband dynamics while HH5 and HH9 were mostly generated by intraband dynamics alone. The different appearance of the maps of HH5 and HH7 could therefore possibly be linked to the generation mechanism. This will be discussed further in Sec. 3.3. Note also that the continuous structures appeared for above-bandgap harmonics from ZnO.

[‡]The Fresnel rhomb has not been used before in this thesis. It introduces a $\pi/2$-phase shift by multiple total internal reflections inside a glass prism. It is therefore a broadband device and besides a more complicated optical alignment very useful in this case to study its influence on all harmonics at the same time.

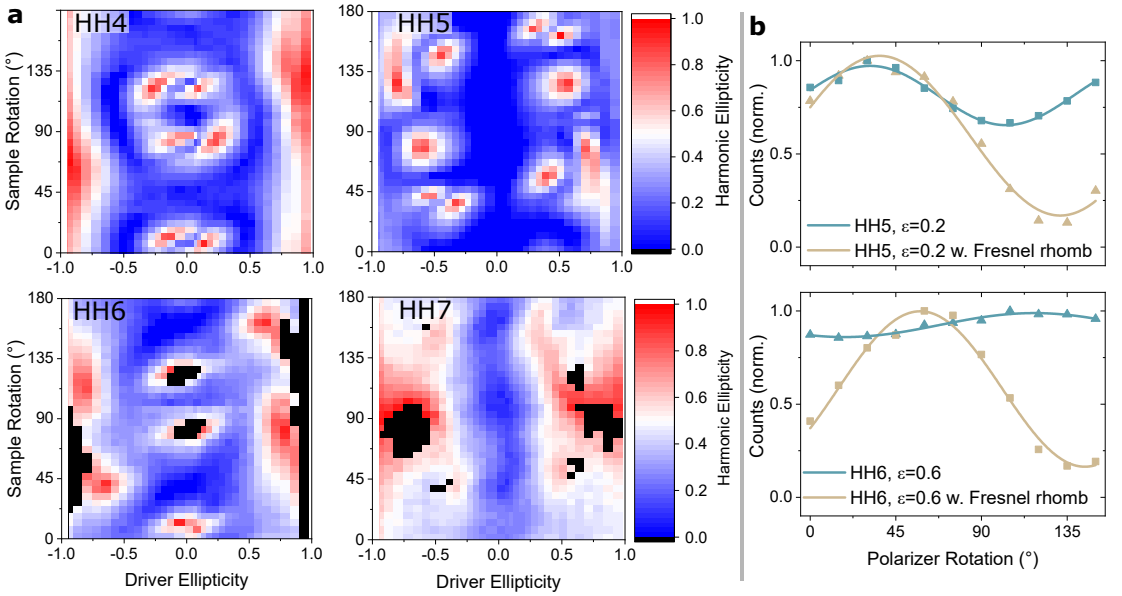

Figure 2.31: **a**: Ellipticity maps from (100)-cut ZnS. Data points where the signal to noise ratio is below 2.57 times the standard deviation are marked in black. **b**: Comparison of polarizer scans of HH5 and HH6 with and without inserted Fresnel rhomb, to confirm that harmonics are polarized.

The maps of the even harmonics HH4 and HH6 seem to differ from HH5 and HH7 once again. Here, there are cases with $|\epsilon_n| \approx 1$ for linearly polarized excitation. This is indeed surprising. Already in previous publications, the even harmonics have been shown to behave differently. The most prominent example of this is that even harmonics are perpendicularly polarized to the driving field (with linear excitation) for certain conditions. This has been argued to be due to the symmetry of the crystal in GaSe [176, 177] or due to the Berry curvature in SiO_2 [135] and MoS_2 [85]. The behavior of even harmonics in this experiment needs to be investigated further and is little understood so far. One possible explanation could lie in a counterbalancing of the anomalous and the conventional velocity component in the intraband-only Eq. 1.15. But at this point this is pure speculation.

ZnS belongs to the T_D symmetry group [178]. From symmetry arguments it follows that with circular driving fields, all harmonics (odd + even) should exist and be elliptically polarized [148]. This prediction is well captured in the measured data in Fig. 2.31**a**. Intuitively, this result can be understood by considering that this lattice has different nonlinearities along perpendicular directions. This causes the harmonics to have elliptical polarization when generated from a circularly polarized field.

The degree of polarization has been verified for some exemplary conditions, as shown in Fig. 2.31**b**. Harmonics are highly polarized in most cases that were looked at, however some significant depolarization appears for certain driving conditions. This will be discussed in greater detail in Sec. 3.3.3.

Chapter 3

Single-particle intraband-only calculations

The previous chapter revolved around the experimental high-harmonic response to elliptical excitation. This led to the discovery that the harmonics' polarization states were depending very sensitively on the driving conditions, particularly the ellipticity of the driving pulses as well as the crystals' rotation. Most noteworthy were the generation of circular harmonics both from circular (CHCD) and from elliptical drivers (CHED). Also a rotation of the harmonics' polarization major axis could be observed in some cases. While the *ab-initio* TDDFT-calculations from N. Tancogne-Dejean reproduced these results quite accurately (compare Fig. 2.19), it is difficult to extract further insights into the underlying physical mechanism from them. This is because they do not allow to separate intra- and interband dynamics. Although this represents a realistic restraint, as these two never appear separated in experiment either, it complicates learning more about the individual influences of each of those mechanisms. Furthermore, the TDDFT-calculations are extremely costly from a computational perspective.

While intra- and interband dynamics cannot be separated generally, it is clear that harmonics with low JDOS or harmonics with photon energies below the direct band gap are generated mainly by intraband dynamics [104, 105, 161]. Because CHED and CHCD have been observed also from those harmonics orders, it seems reasonable to study the influence of intraband dynamics on the harmonics' response to elliptical excitation individually. If one can identify features in the results of such simple dynamics alone, one can possibly draw conclusions also for the measured results. This will be the topic of this chapter.

Intraband-only calculations have been successfully utilized to reproduce the linear relationship of the cutoff energy to the driving field [38, 179], the six-fold rotational symmetry of HHG spectra in the three-fold symmetric crystal GaSe [177], anisotropic HHG emission in ZnSe [93] as well as to reconstruct the Berry curvature [135] and the band structure of SiO_2 [89] and ZnSe [40]. However, in solid-state HHG they have so far not been used to study the effects of elliptical polarization. It is clear that such a model ignores influences from dephasing [92], wave packet spread [105], HHG from multiple bands [100], contribution from holes

[93], along with effects of the subcycle ionization dynamics [180].

One should emphasize that the intraband mechanism was observed to underlie high-harmonic emission with the highest photon energies reported from solids to date ($\approx 40\,\mathrm{eV}$) [89,116]. So although only low-order harmonics are discussed in this chapter, the findings should be applicable to any intraband-dominated generation of higher energy photons, potentially supporting circularly polarized harmonics up into the XUV-spectral region.

3.1 The model

This section is largely reprinted from the corresponding publication [181]. Let us consider an electron wave packet in a single band. The current density $\mathbf{j}$ at time t can be described as (compare Eq. 1.7)

$$\mathbf{j}(t) = -\int_{\mathrm{BZ}} e\mathbf{v}_{\mathbf{k}}(t) n_{\mathbf{k}}(t) \mathrm{d}\mathbf{k}. \tag{3.1}$$

Here, BZ refers to the first Brillouin zone, e is the electron charge, $n_{\mathbf{k}}$ is the charge distribution in $\mathbf{k}$-space and $\mathbf{v}_{\mathbf{k}}$ is the $\mathbf{k}$-dependent electron velocity, which consists of two terms

$$\mathbf{v}_{\mathbf{k}} = \underbrace{\frac{1}{\hbar}\frac{\mathrm{d}\mathcal{E}_{\mathbf{k}}}{\mathrm{d}\mathbf{k}}}_{\mathbf{v}_{co}} - \underbrace{\frac{e}{\hbar}\mathbf{E}_{\mathrm{L}} \times \boldsymbol{\Omega}(\mathbf{k})}_{\mathbf{v}_{ano}}. \tag{3.2}$$

While the first term describes the well-known velocity a charge has within a conduction band $\mathcal{E}_{\mathbf{k}}$, the second term is the so called anomalous velocity $\mathbf{v}_{ano}$ and contains the driving laser field $\mathbf{E}_{\mathrm{L}}$ and the Berry curvature $\boldsymbol{\Omega}(\mathbf{k})$. Sec. 3.3.1 will discuss the influence of $\mathbf{v}_{ano}$ on the calculated high-harmonic spectra. However, since the Berry curvature vanishes for inversion symmetric materials [182], let us set $v_{ano} = 0$ for now. Neglecting the influence of the Berry curvature in this model is in line with other recent works that utilized the semiclassical model on solid HHG [40, 89, 93, 177, 183].

Assuming a single fully-localized electron wave packet at $\mathbf{k}(t)$, i.e. $n_{\mathbf{k}}(t) = \delta(\mathbf{k} - \mathbf{k}(t))$ and inserting $\mathbf{v}_{co}$, Eq. (3.1) simplifies to

$$\mathbf{j}(t) = -\frac{e}{\hbar}\frac{\mathrm{d}\mathcal{E}_{\mathbf{k}}}{\mathrm{d}\mathbf{k}}\bigg|_{\mathbf{k}=\mathbf{k}(t)}. \tag{3.3}$$

Under these assumptions, the emitted electric field $\mathbf{E}^{\mathrm{HH}}(t)$ originating from an intraband current is

$$\begin{aligned}\mathbf{E}^{\mathrm{HH}}(t) \propto \frac{\mathrm{d}\mathbf{j}(t)}{\mathrm{d}t} &= -\frac{e}{\hbar}\frac{\mathrm{d}^2\mathcal{E}_{\mathbf{k}}}{\mathrm{d}\mathbf{k}^2}\bigg|_{\mathbf{k}=\mathbf{k}(t)} \cdot \frac{\mathrm{d}\mathbf{k}}{\mathrm{d}t} \\ &= e^2 \left(\frac{1}{m^*_{\mathbf{k}}}\right)\bigg|_{\mathbf{k}=\mathbf{k}(t)} \mathbf{E}_{\mathrm{L}}(t).\end{aligned} \tag{3.4}$$

$m^*_{\mathbf{k}}$ denotes the effective mass tensor. Here the acceleration theorem

$$\mathbf{k}(t) = -\frac{e}{\hbar}\int_{-\infty}^{t} \mathbf{E}_{\mathrm{L}}(t')dt' \tag{3.5}$$

has been used and with it the assumption that the electron is initially at the Γ-point. Regarding the calculation of $\mathbf{k}$: The impact of Bloch oscillations is investigated in the one-dimensional case in Sec. 3.2.1. There, k is kept within the first Brillouin zone by subtracting or adding $2\pi a$ whenever the calculated k is outside of the first Brillouin zone.

In the simplest tight-binding-type band structure that will be discussed in Sec. 3.2, the off-diagonal terms in $\left(\frac{1}{m^*_{\mathbf{k}}}\right)$ are zero. In this case, Eq. (3.4) further simplifies to

$$E_x^{\mathrm{HH}} \propto \frac{\partial^2 \mathcal{E}_{\mathbf{k}}}{\partial k_x^2} E_{\mathrm{L},x}, \tag{3.6a}$$

$$E_y^{\mathrm{HH}} \propto \frac{\partial^2 \mathcal{E}_{\mathbf{k}}}{\partial k_y^2} E_{\mathrm{L},y}. \tag{3.6b}$$

Finally, the emitted high-harmonic spectrum can be calculated as

$$\mathrm{I}_{\mathrm{HH}}(\omega) \propto \left|\mathrm{FT}[\mathbf{E}_{\mathrm{HH}}(t)]\right|^2. \tag{3.7}$$

It can be seen from Eq. (3.4) that the nonlinear evolution of $\frac{\mathrm{d}^2\mathcal{E}_{\mathbf{k}}}{\mathrm{d}k^2}$ is the source for emission of higher frequency content. When happening in repetition over multiple laser cycles, this emission gives rise to a non-perturbative, high-harmonic spectrum in the frequency domain [38, 84].

The following discussion will not discuss E_x and E_y but instead use the parallel and perpendicular field components, defined with respect to the driving major axis, i.e., $E_\parallel$ and $E_\perp$. To obtain harmonic orders n and their corresponding electric field $\mathbf{E}_n$, the Fourier transform of the total electric field is band pass filtered in a window of $n \pm \mathrm{f}/0.3$, f being the center frequency of the driving field. The harmonic ellipticities are calculated with

$$|\epsilon_n| = \sqrt{\frac{I_n(\alpha_{min})}{I_n(\alpha_{max})}}, \tag{3.8}$$

where α denotes the angle of maximum or minimum harmonic yield I_n. This resembles the experimental method to rotate a polarizer. The driving field is

$$\mathbf{E}_{\mathrm{L}}(t) = \frac{\tilde{E}(t)}{\sqrt{1+\epsilon^2}} \begin{pmatrix} \cos(\omega t) \\ \epsilon \sin(\omega t) \end{pmatrix}, \tag{3.9}$$

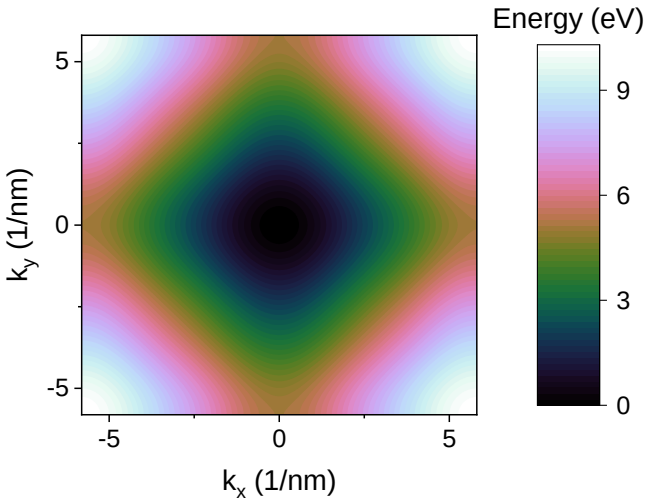

Figure 3.1: The tight-binding band structure with all $c_n = 0$ except for $c_1 = -0.95$ and $c_3 = -0.05$.

where $\tilde{E}(t)$ is a Gaussian envelope with a FWHM pulse duration of 70 fs and the central wavelength is 2100 nm. The field is rotated by an angle θ by multiplying $\mathbf{E}_\mathrm{L}$ with the rotation matrix.

The code has been written in MATLAB and consists of approximately 700 lines. It allows for easy variation of some fundamental variables: The driving ellipticity, lattice rotation, intensity and the tight-binding coefficients (Eq. 3.10). Additionally one can input other band structures, for instance the one of ZnS.

3.2 Tight-binding band structure

In this section, the two-dimensional tight-binding band structure

$$\mathcal{E}_k = \frac{\hbar^2}{4a^2 m_e}\left[1 + \sum_m c_m(cos(mk_x a) + cos(mk_y a))\right] \tag{3.10}$$

will be employed. All c_m are set to zero except for $c_1 = -0.95$ and $c_3 = -0.05$. These coefficients have previously been used to theoretically model HHG from ZnO from intraband dynamics alone [38], although there, only in the one-dimensional case. The lattice constant of ZnS is used, i.e. a = 5.4 Å. The band dispersion is depicted in Fig. 3.1.

3.2.1 The one-dimensional case: Two different kinds of harmonics

While this section aims at exploring the intraband-only model in a two-dimensional lattice, it is instructive to first discuss the simple one-dimensional case. This helps in both verifying the code as well as understanding some basic consequences from

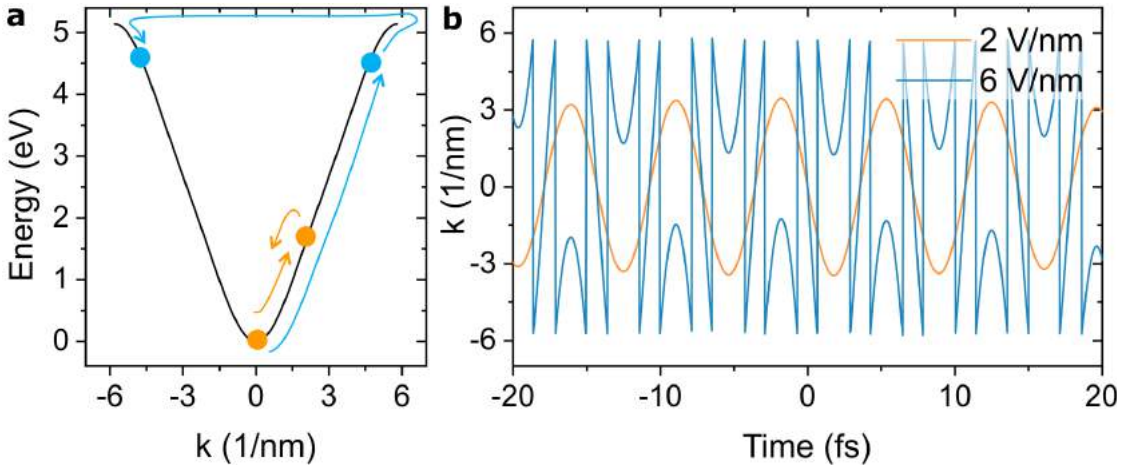

Figure 3.2: **a**: Schematic of electron oscillations in a conduction band with (blue) and without (orange) Bloch oscillations. **b**: Excerpt of the resulting crystal momentum plotted over time. The blue curve shows clear Bloch oscillations.

this model. In this section, the tight binding band structure as described in Eq. 3.10 is employed. The driving field is linearly polarized along k_x.

It is important to realize that intraband dynamics can generate harmonics in two distinct ways. On the one hand, harmonics are emitted due to the non-parabolic shape of the conduction band (Eq. 3.4). This means that the electrons' velocity has a non-trivial dependence on the driving field strength and thus, the field-driven electron oscillations contain higher frequency components. On the other hand, even with a hypothetical parabolic band shape, harmonics are emitted if the electron is accelerated strongly enough such that it traverses the edge of the Brillouin zone. If this happens, the crystal momentum flips its sign instantly, leading to the counter-intuitive phenomenon that electron oscillations can be triggered by a dc-field (for a discussion of these Bloch oscillations, see also Sec. 1.2.1). Figure 3.2**a** visualizes this with a schematic of an electron and its oscillation when driven with two different driving intensities. The higher intensity provides enough acceleration within a laser half-cycle such that the electron traverses the Brillouin-zone-edge (blue). With the lower intensity, this is not the case (orange). For both these cases, the crystal momenta k have been calculated in Fig. 3.2**b**. Here, the implications of the two different driving conditions are obvious. While k of the orange curve seems to follow the driving wave (it consists of weak higher frequency components too), it is apparent that the Bloch oscillations (blue curve) distort the crystal momentum strongly. Whenever the electron traverses the edge of the Brillouin zone, the crystal momentum is reversed (compare also Fig. 3 in Ref. [88]).

Naturally, this behavior has major implications for the resulting high-harmonic spectra, which are shown in Fig. 3.3**a** for the two cases. The harmonic spectrum of the lower field strength consists of harmonics up to the 11^{th}-order with an exponential decrease of the harmonics' yield. On the other hand, for the higher

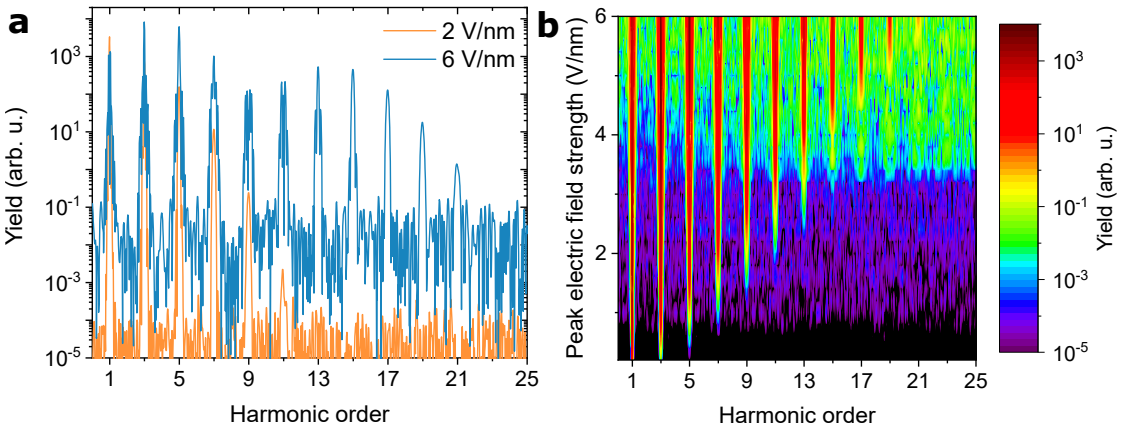

Figure 3.3: High-harmonic spectra from the single particle intraband-only model with a tight-binding band structure in one dimension. **a**: Two different driving field strengths **b**: Scan of driving field strengths.

field-strength case, the spectrum exhibits a second plateau for harmonics above the 9^{th}-order and the highest harmonic order observed is 21. Also the noise floor of the higher field strength is higher. This originates in the instantaneous jumps of k which result in a broad frequency spectrum. The two spectra are the same as shown for similar conditions in Ref. [38] (i.e. band structure and laser parameters), which gives confidence that the implemented code is correct. Note that, because the band structure is inversion symmetric, only odd harmonics are present in these spectra. It should also be mentioned that the second plateau due to Bloch oscillations that is seen here has a different origin than the multiple plateaus that have been observed when electrons reach higher lying conduction band and perform interband transitions from there [86, 99, 143].

It is interesting to extend these investigations on the one-dimensional intraband-only model to variation of the driving field strength. Fig. 3.3**b** shows the harmonic spectra plotted in logarithmic scale versus the driving field strength. It is apparent that the cutoff frequency depends linearly on the field strength [84, 132] which has also been verified in an experiment in ZnO [38]. The sudden increase in the noise floor and the appearance of the second plateau just above 3 V/nm is due to Bloch oscillations that appear only above this field strength.

It is understood that Bloch oscillations play a major role for long wavelength driving lasers [88] however for the driving conditions employed experimentally in this work, Bloch oscillations can be neglected [161]. Hence in the rest of this chapter, the analysis is concerned only with the pure HH emission due to the non-parabolic shape of the conduction band. The driving field strength will therefore be 2 V/nm which is below the threshold above which Bloch oscillations appear. In all further sections in this chapter, it is verified that Bloch oscillations do not appear. Let us now extend the previous analysis to two dimensions.

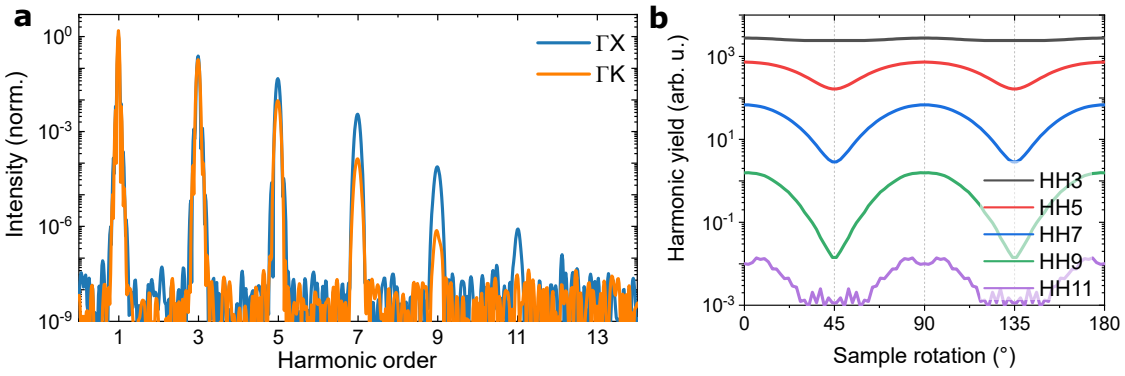

Figure 3.4: Simulated HHG with linear driving polarization. **a**: Harmonic spectra for two different sample orientations, **b**: Harmonic yields versus sample rotation.

3.2.2 The two-dimensional case: Circularly polarized harmonics

There are quite some things to analyze with the intraband model in two dimensions. Let us start by investigating the harmonic response for linear driving polarization along different rotations of the lattice will be studied. Note that, for consistency with the other chapters, 'sample rotation' will be used synonymously with a virtual rotation of the lattice. Furthermore, let us call the axes parallel to k_x and k_y ΓX (i.e. 0° and 90° rotation) and the ones rotated by 45° ΓK.

Figure 3.4**a** shows spectra for both ΓX and ΓK. The ΓX-spectrum is the same that was shown in Fig. 3.3**a** and extends up to the 11^{th}-order. Along ΓK, harmonic emission seems to be less favorable and the general harmonic yield is reduced. Also, the highest observable harmonic is HH9 and therefore reduced. This result is in contrast to what is observed in HHG from atoms in gas phase because there, the cutoff is determined by the maximum kinetic energy that the free electron can acquire while being accelerated in the vacuum. Hence, the strong field approximation implies that the rotation of the laser polarization direction with respect to the gas atoms has a neglible impact on the highest acquirable kinetic energy. In the intraband model, since the electron is never free, the sample rotation affects not only the yield of the harmonics but also the cutoff. This is directly related to the theoretical prediction in Ref. [105] that the cutoff can be enhanced with elliptically polarized driving pulses, which will be investigated in Chapter 4.

In Fig. 3.4**b**, the harmonic yields are plotted versus sample rotation. All of the harmonics are maximized along ΓX and minimized along ΓK. When comparing these directions to the precise shape of the band dispersion (see Fig. 3.1), the harmonic yield is maximized along the lowest slope of the band dispersion. Also, the harmonic yields' variation over sample rotation increases with increasing harmonic order n. Note also that the harmonic yields are 90°-symmetric, which is consistent with the band structure as it describes a square lattice.

Let us now turn to some polarization-related quantities and look at the perpendicular and parallel harmonic components separately and additionally explore

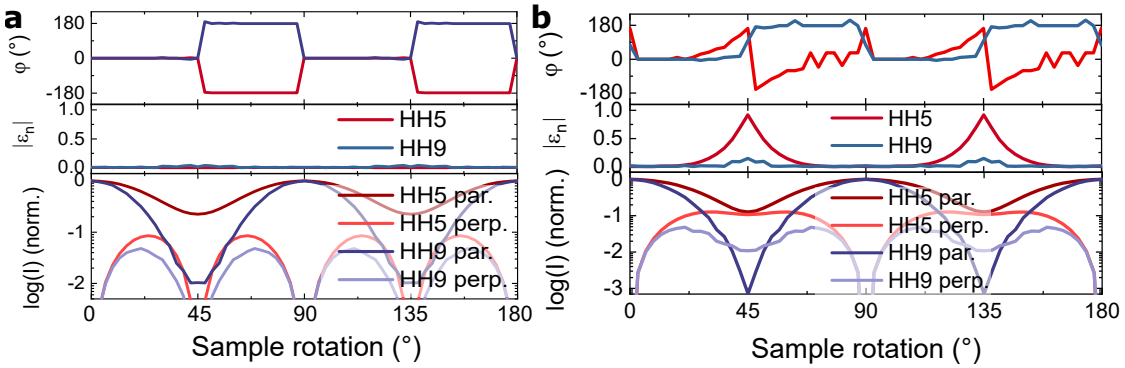

Figure 3.5: Both figures show the same polarization-related quantities of HH5 and HH9 versus sample rotation. Top panel: Relative phase φ between $E_{\parallel}$ and $E_{\perp}$, center panel: Harmonic ellipticities, bottom panel: Respective intensity components of the parallel and perpendicular components of HH5 and HH9. **a**: $\epsilon = 0$, **b**: $\epsilon = 0.15$.

their relative phases φ as well as the harmonics' ellipticities $|\epsilon_n|$. Figure 3.5**a** shows a rotational scan as before with linear driving polarization. Perhaps as one would expect, also the harmonics' ellipticity remains zero for any sample rotation. For polarization along the major symmetry axes ΓX and ΓK, there is no perpendicular intensity component of the harmonics and hence, the harmonics' polarization follows the driving polarization fully. What is striking however is the presence of a perpendicular component when generated off a major symmetry axis, especially for $\theta \approx 22°$ for both harmonics. This, together with the fact that the relative phase φ remains 0 for all sample rotations, means that the harmonics' major axis is rotated slightly but remains linearly polarized. This by itself is a fascinating result and a similar behavior to this has been reported experimentally from MgO [143] and has there been attempted to be explained with a real-space recollision model. Considering the problems that this model has, it might perhaps be worth investigating the intraband dynamics as well.

How will the harmonics react to elliptical driving excitation? Figure 3.5**b** plots the same quantities as before but with $\epsilon = 0.15$. Now the perpendicular components do not disappear for driving major axis along ΓK. In fact, the parallel and perpendicular components of HH5 reach the same values for this sample direction. This, combined with the fact that $|\varphi| = 90°$, means that the harmonic ellipticity peaks for this case. In fact, in these conditions, HH5 is circularly polarized along ΓK with elliptically polarized excitation. CHED can therefore be found already with such a simple intraband-only model and a tight-binding-type band structure. For HH9, the perpendicular component is stronger than the parallel one along ΓK, which means that the harmonics' major axis is rotated with respect to the driving field. Major-axis rotation with elliptically polarized fields has been observed in Graphene [46] and, as elaborated on in Chapter 2, in Si [161].

These are the first intraband-only calculations with an elliptically polarized field that the author is aware of and also the first microscopic explanation for the

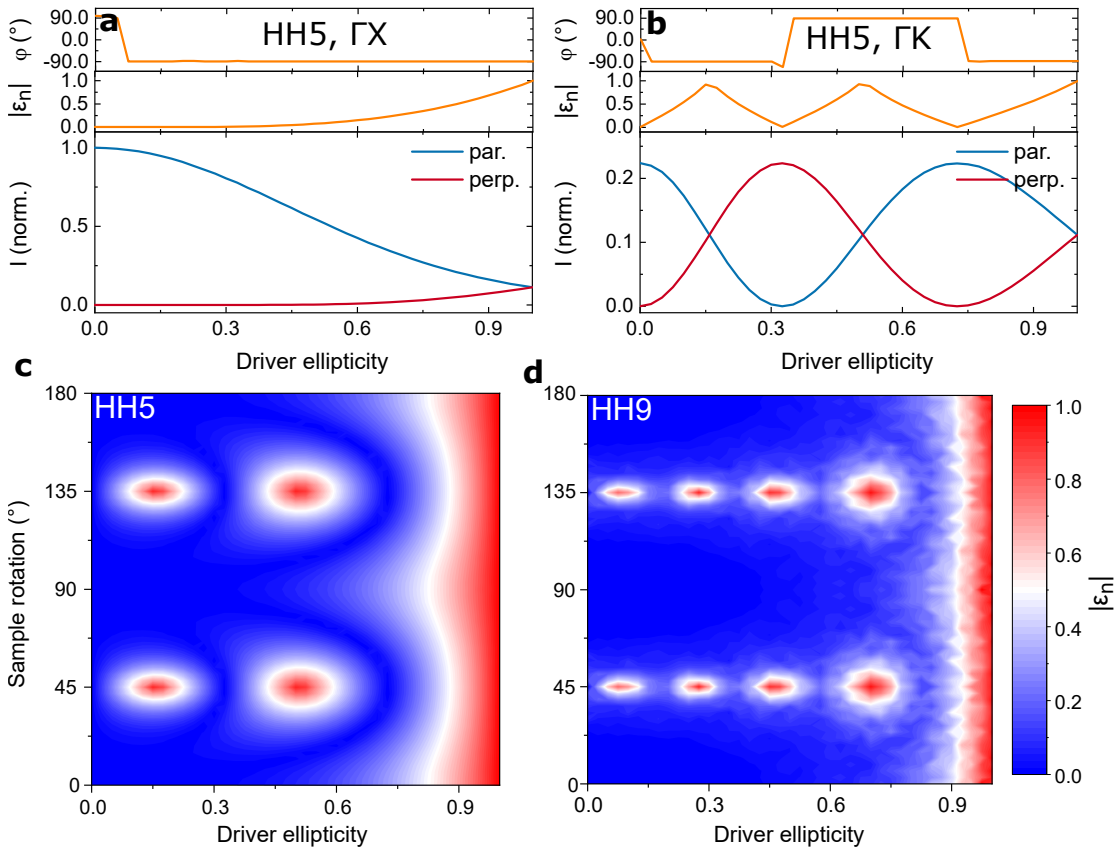

Figure 3.6: **a**,**b**:Relative phase φ, absolute value of the harmonic ellipticity $|\epsilon_n|$ as well as intensities of parallel and perpendicular components of HH5 in dependence of the driving ellipticity. **a**: ΓX, **b**: ΓK. Complete maps of harmonics' ellipticity of HH5 (**c**) and HH9 (**d**).

appearance of CHED.

The next logical step is not to scan the harmonics' response to the rotation of the sample but to scan the driving ellipticity ϵ instead. This is depicted in Figs. 3.6**a** and **b** for θ along the two major symmetry directions. Let us recall that the direction that most efficiently produces harmonics is ΓX. If one introduces ellipticity on the driving field along $\theta = \Gamma X$, one drives the electrons away from this most efficient direction. This causes the total harmonic yield to decrease (bottom panel in Fig. 3.6**a**). While the parallel component decreases, the perpendicular component increases very slowly, only to reach the same intensity as the parallel component for $\epsilon = 1$. As one can see in the center panel of Fig. 3.6**a**, the harmonics' ellipticity remains close to zero for any $\epsilon < 0.6$ and then increases to 1 for circular driving fields. The band structure used here represents a square lattice and, as argued in the last chapter repeatedly, these lattices require odd harmonics to be circularly polarized with $\epsilon = 1$. The simple intraband model reproduces that. It even produces harmonics that have alternating helicities (not shown).

Fascinating behavior of the harmonic starts to arise when $\theta = \Gamma K$ (Fig. 3.6**b**).

This is the least efficient direction to generate harmonics. Introducing elliptical driving fields therefore drives the electron away from this direction with lowest nonlinearity. Hence, the nonlinearity is enhanced due to the elliptical polarization. This leads to a very rapid rise of the perpendicular component already with low ϵ. For $\epsilon = 0.15$ (the case that has been shown above already), perpendicular and parallel component are equal, causing the harmonic to be circularly polarized. For higher ϵ, the perpendicular component gets even stronger, which rotates the harmonic polarization axis with respect to the driving field by 90°. When ϵ reaches 0.3, the perpendicular component peaks and decreases again, while the parallel component is increased until the two cross over again at $\epsilon \approx 0.5$. Here, HH5 is once again circularly polarized (with opposite helicity as before as φ reveals). Above this value, the harmonic is parallel to the driving field and becomes circular for $\epsilon = 1$. Note that very similar behavior to this has been observed in Si (compare Figs. 2.19 and 2.23).

The total harmonic yield does not decrease with increasing ϵ for $\theta = \Gamma\mathrm{K}$. Indeed this seems surprising, since from gas HHG one would always expect the yield to decrease due to the decreasing probability for electron and parent ion to recollide. In the intraband model, harmonic emission stems from the non-parabolic shape of the conduction band and the harmonic yield is completely independent on any chance of recollision. In principle, harmonic yield could also increase with increasing ellipticity, if the nonlinearity just so happens to be higher with this trajectory in reciprocal space (this was observed for instance in Ref. [46]). Saito *et al.* [147] found the harmonic yield to be unchanged when going from linear to circular excitation which could be a good indication for intraband dynamics to be dominant. One thing to consider however, is that our model ignores the influence of ionization. In a real system, increasing ϵ will decrease the driving field strength by a factor $(1 + \epsilon^2)^{-1/2}$ and hence, less electrons will contribute to the harmonic emission process which in turn could decrease the harmonic yield again. But even this influence is unclear because less electrons in the conduction band could also cause less dephasing to be present which in turn could also increase the harmonic yield. As one can see from this sobering discussion, there are plenty opportunities for speculation in complex and system-dependent dynamics like the ones underlying in solid HHG.

Figures 3.6**c** and **d** show the full ellipticity maps of HH5 and HH9 in dependence of the sample rotation and the driving ellipticity which summarize the findings discussed until here. Harmonics are linearly polarized with linear excitation and with elliptical excitation too when θ is close to ΓX. CHED appear along the least efficient direction to generate harmonics, ΓK, and more of these islands appear for HH9 than they do for HH5. Also this is similar to the experimental maps discussed so far, where higher harmonics showed more islands of CHED. For circular excitation, harmonics are circularly polarized and subsequent harmonics are rotating in opposing senses (not shown), as required by symmetry for a four-fold-symmetric system [148].

Figure 3.7 shows the same maps of $|\epsilon_5|$ as before, but now for four different driving field strengths. Almost no difference can be seen for different field strengths

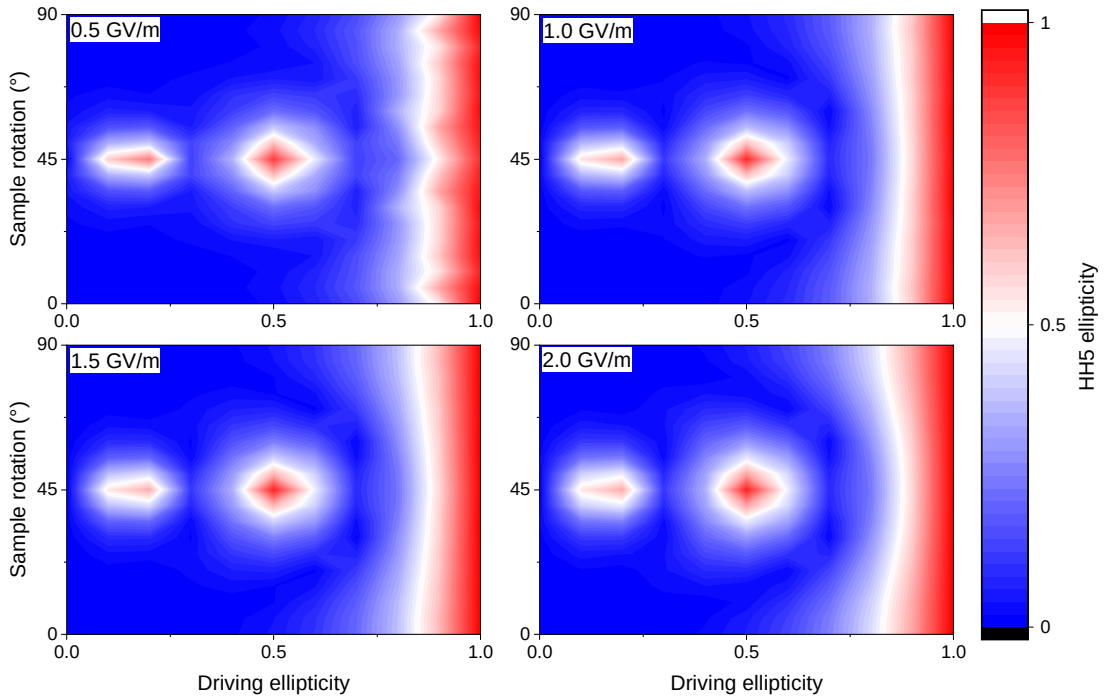

Figure 3.7: Maps of $|\epsilon_5|$ for four different driving field strengths, ranging from 0.5 GV/m to 2 GV/m.

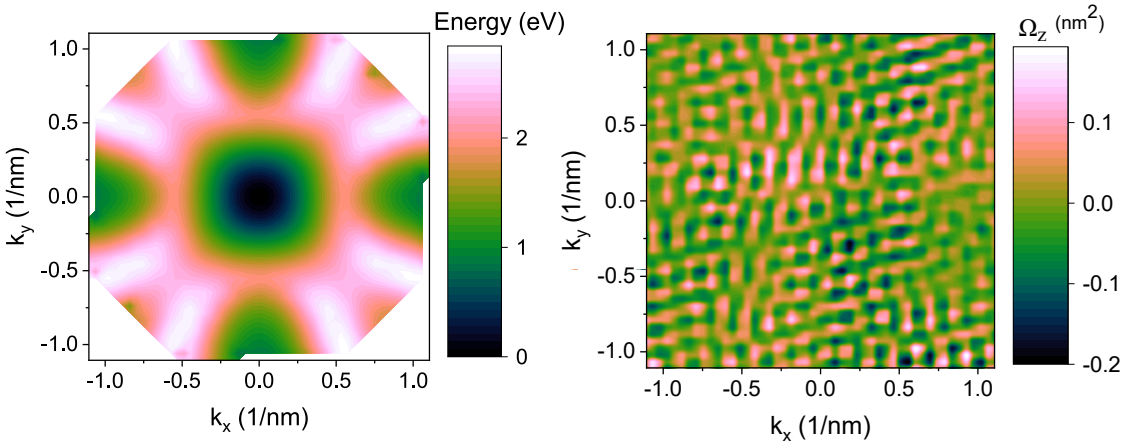

Figure 3.8: Left: The first conduction band dispersion of ZnS. Right: The z-component of the Berry curvature, Ω_z, averaged over all bands. Both figures calculated by means of DFT by N. Tancogne-Dejean.

which means that the ratio of x- and y-components of the effective mass in Eq. 3.6 do not change with the driving field strength for this particular band structure. It will be shown later that this is not necessarily the case.

3.3 Zinc sulfide band structure

After having studied a model band structure, it is interesting to extend the current analysis to a a real system and see how the intraband-only model compares to results obtained from experiments. The material of choice will be ZnS (see measurements and discussion in Sec. 2.4.3) because the conduction band of ZnS is well isolated from higher-lying conduction bands. This could render the one-band intraband-only model a reasonable approximation. It should be mentioned that, while the first conduction band is well isolated from the others, this is not the case for the valence bands. Both a heavy hole as well as a light hole band are present in ZnS. Hole dynamics are ignored in this chapter but they do impact the emission in some way [93]. Since harmonics below the band gap should be produced predominantly by intraband dynamics, the focus of our attention will lie on the below-band-gap-harmonic HH5.

3.3.1 The influence of the anomalous velocity

ZnS has a zinc-blende crystal structure. Therefore it is not inversion symmetric along certain crystal directions. This means that the Berry curvature $\mathbf{\Omega}(\mathbf{k})$ in Eq. 3.2 does not vanish. The theory collaborator of this work, N. Tancogne-Dejean, has supplied us with a calculated Berry curvature that is averaged over all the bands. While this is not very useful for precise comparison between measurements and calculations, it does help to explore what influence a non-vanishing Berry curvature can have on the high-harmonic response. This should be the aim of this section.

The anomalous velocity is

$$\mathbf{v}_{ano} = -\frac{e}{\hbar}\mathbf{E}(t) \times \mathbf{\Omega}(\mathbf{k}) = -\frac{e}{\hbar}\begin{pmatrix} E_y\Omega_z - E_z\Omega_y \\ E_z\Omega_x - E_x\Omega_z \\ E_x\Omega_y - E_y\Omega_x \end{pmatrix}. \tag{3.11}$$

By our definition, the z-component is the propagation direction of the laser pulse. This means that $E_z = 0$. Consequently

$$v_{ano,x} = -(e/\hbar)E_y\Omega_z, \quad \text{and} \tag{3.12a}$$
$$v_{ano,y} = (e/\hbar)E_x\Omega_z. \tag{3.12b}$$

Interestingly, v_{ano} also has a z-component. Thus, the Berry curvature causes electrons to oscillate also in the propagation direction of the laser. This component will be ignored in the future discussion because it does not affect the polarization of the emitted harmonics in the plane of the polarizer. According to Eqs. 3.12, only the z-component of the Berry curvature appears in the the x- and y-components of v_{ano}. It is plotted in Fig. 3.8.

In the experimental harmonic spectra, the lack of inversion symmetry manifests itself in the generation of even-order harmonics. The band structure on the other

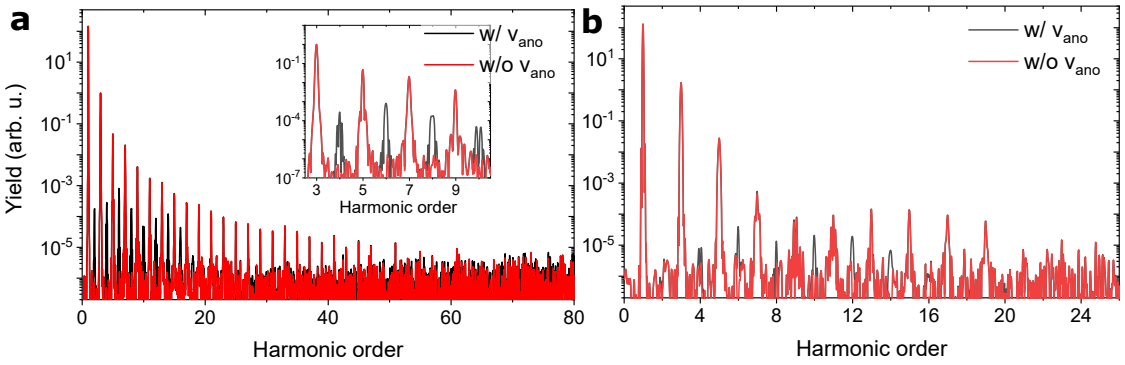

Figure 3.9: Calculated spectra from ZnS for $\theta = 0°$ (**a**) and $\theta = 45°$(**b**). Both figures contain the spectra calculated with v_{ano} and without. Driving field strength is 1 V/nm and $\epsilon = 0$.

hand is by definition inversion symmetric and hence the intraband-only model fails to reproduce even harmonics [135, 177], when v_{ano} is not included. It is known, that if the contribution of v_{ano} is accounted for, even harmonics appear in the high-harmonic spectra [85, 135].

Figure 3.9 shows spectra calculated with the model described above for two different sample rotations $\theta = 0°$ and $\theta = 45°$, each for one case where v_{ano} is included and one in which it is not. Three noteworthy conclusions can be drawn from this figure. First, as predicted, the spectra with v_{ano} do contain even harmonics. Second, the influence of v_{ano} on the odd harmonics is neglible, which can be seen by the complete overlap of the red and black curves. Third, with and without contribution of v_{ano}, the cutoff extends much higher than with the tight-binding band structure from the previous section, where it went to the 11^{th} harmonic. For $\theta = 0°$, harmonics up to the 50^{th}-order can be observed. For $\theta = 45°$, the cutoff is reduced to the 20^{th}-order. Consequently, the ZnS band structure is much less parabolic than the tight-binding band structure, which can already be anticipated from its appearance in Fig. 3.8.

Also, note that the spectra exhibit a clear plateau-like structure. This was not really the case with the tight-binding band structure, except for when Bloch oscillations were included. Here, due to the stronger non-linearity of the band structure, the harmonics form a plateau as one can observe in experiments.

One can also compute the harmonic ellipticity, here for HH5, $|\epsilon_5|$ and compare its values obtained both with v_{ano} included and without. This is shown in Fig. 3.10 for varying ϵ under four different sample rotations. While $|\epsilon_5|$ behaves in a unique way, especially for $\theta = 45°$, the exact behavior will be discussed more deeply when comparing the calculation results to the experiment. What should be looked at here, is the influence of v_{ano} and if it alters the calculated response. This does indeed seem to be the case, although for this Berry curvature, the influence is neglible. At this point, it is unclear what would happen if the band-specific Berry curvature would be used. However, calculating the latter is out of scope of this thesis.

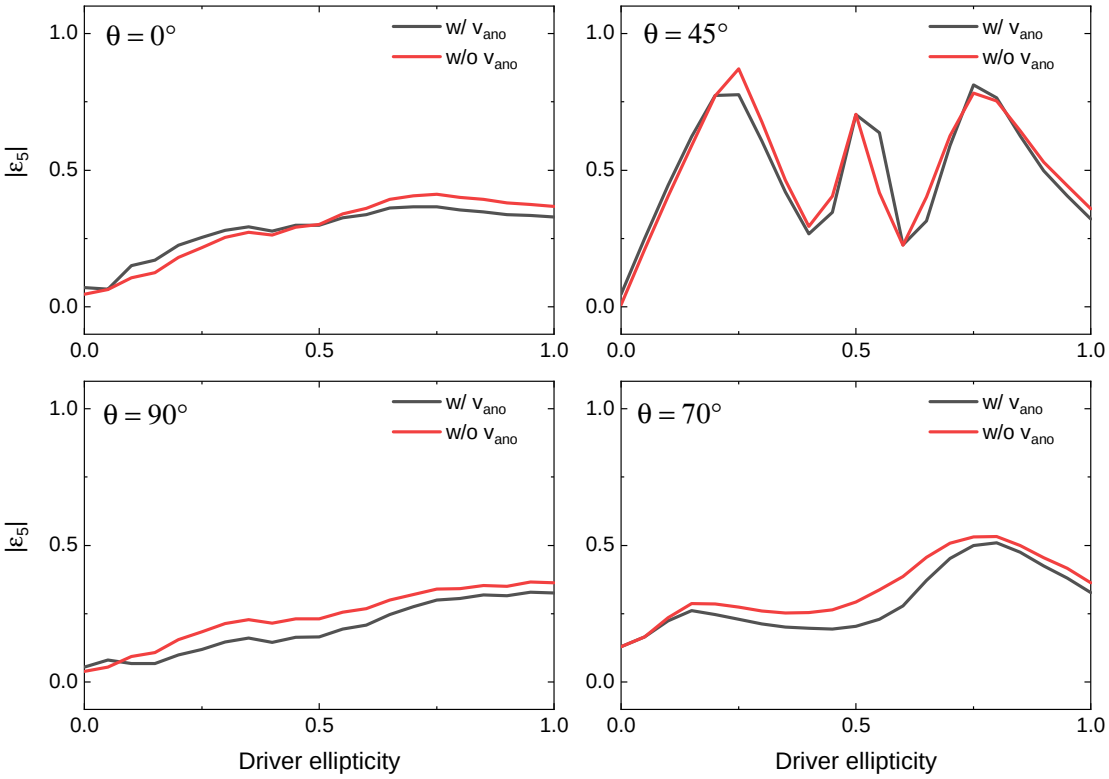

Figure 3.10: The influence of the anomalous velocity on the computed ellipticity of HH5 when varying ϵ for four different θ.

One thing to point out is that all the curves combined in Fig. 3.10 have been computed within five minutes on a standard office computer. In comparison, each data point in Fig. 2.19 calculated by means of TDDFT took approximately one day on a supercomputer, making it 10 days for one ϵ-scan with 10 datapoints. This makes clear that the model used in this chapter is strongly simplifying the physical reality on one hand, but also that, if this simplified model turns out to describe some features accurately, it would be extremely useful especially for calculations in which many parameters need to be scanned.

Concluding this section, one should say that, while in Ref. [135] it is argued that for a tight-binding band structure, the anomalous velocity term can be ignored when studying odd harmonics, we see that this is not necessarily the case for a real band structure. The exact influence of it, however, remains to be investigated in future work. In the rest of this chapter we will set $v_{ano} = 0$ and study the pure influence of the conventional velocity term on the high-harmonic response from ZnS.

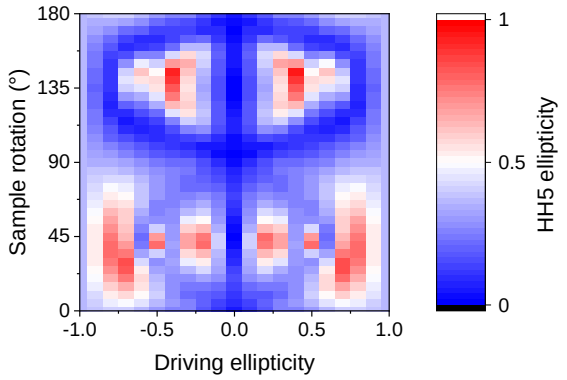

Figure 3.11: Computed $|\epsilon_5|$-map for the full range of ϵ.

3.3.2 Artificial symmetries, the dependence on intensity and depolarization

Let us take a moment to discuss some features and artefacts of the calculated results of the ellipticity response of HH5 before we compare it to the experimental data in Sec. 3.3.3. Fig. 3.11 shows a full map of $|\epsilon_5|$ calculated with experimental conditions, i.e. 2.1 μm, 70 fs and 1 GV/m peak electric field strength in matter. One thing to note is the symmetry with respect to $\epsilon = 0$, i.e. $|\epsilon_n(\epsilon, \theta)| = |\epsilon_n(-\epsilon, \theta)|$ for any arbitrary driving ellipticity ϵ and sample rotation θ. One could call this an 'artificial' symmetry because it does not appear in the experimental data. Instead, in experiment, the crystal structure of ZnS leads to symmetry rules of the type $|\epsilon_{\mathrm{n}}(\theta, \epsilon)| = |\epsilon_{\mathrm{n}}(180° - \theta, -\epsilon)|$, where θ refers to the rotation angle with respect to one of the symmetry axes.

Let us linger on this discrepancy for a bit. The band structure is inversion symmetric and hence, it seems obvious that the current produced by a laser pulse is the same when generated with positive or negative helicities because the electron will traverse the same nonlinearities in opposite directions. Thus, a process that broke this symmetry between left and right helicities could in principle produce differing $|\epsilon_5|$ in these cases. A process that comes to mind is the transition of electrons from the valence to the conduction band which happen in successive steps at the peaks of E_{L}. It is also feasible that dephasing would break this symmetry if the dephasing times were sufficiently short. This, however, is unclear and quite debated [92, 106, 184]. It is also feasible that the inclusion of hole dynamics could introduce some fundamental differences between positive and negative helicities. In any case, a symmetry-breaking process would somehow need to induce another symmetry, as there are the above mentioned symmetries observed in the experiments. To the author, the origin of this is unclear.

While more work is needed to resolve these said issues, there exist an applicable remedy for this problem. That is, to consider only one driving helicity. Either way, also in experiments the results for positive and negative ϵ are redundant due to the prevalent crystal symmetries. Thereby, by considering only one driving helicity, one does not lose any information.

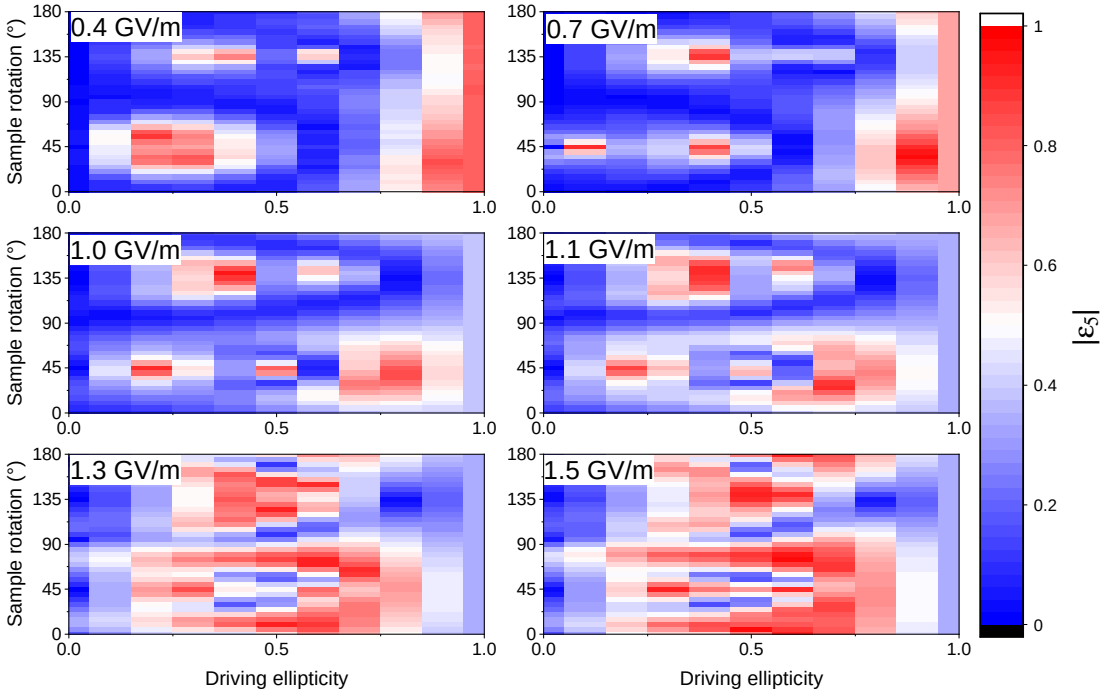

Figure 3.12: Computed $|\epsilon_5|$-maps for six different peak electric field strengths.

Another important aspect when comparing the computed results to measurements is an uncertainty in the exact peak electric field strength E_0. That is an experimental quantity prone to errors for a number of reasons. Both beam size and pulse duration measurements have a certain variance, especially for pulses that are not necessarily Gaussian. Propagation through the sample could also affect the electric field strength due to nonlinear propagation effects, especially self-phase modulation and multi-photon absorption, although those are not a significant issue with the present conditions in ZnS*. For HH5, since it is below the band gap, it is generated throughout propagation through the sample, which means it is generated with a variety of electric field strengths and even phase-matching issues could arise. Even more so, it is generated not only in the center of the pulse spatially but also with lower field strengths in the wings of the spatial profile [106].

Because of the previous discussion, it is required to compute the high-harmonic response for different peak electric field strengths E_0 and to therefore see how other field strengths compare to the one measured. Fig. 3.12 shows maps of $|\epsilon_5|$ for E_0 ranging from 0.4 GV/m to 1.5 GV/m. Evidently, variation of E_0 strongly alters $|\epsilon_5|$. While for the tight-binding band structure in Sec. 3.2.2, no dependence on the driving field strength was observed, here, $|\epsilon_5|$ increases in average with increasing E_0. This partly goes hand in hand with another effect that happens with stronger

*The accumulated non-linear phase can be calculated with the B-integral $B = 2\pi I n_2 z/\lambda$, where I is the peak intensity, n_2 the nonlinear refractive index ($3.1 \cdot 10^{-15}\mathrm{cm}^2/\mathrm{W}$ at 1.3 μm wavelength [185]) and z the thickness of the sample. $B = 0.15$ rad with experimental conditions. Note that this is only an estimation since n_2 has not been determined at the here present wavelength of 2 μm.

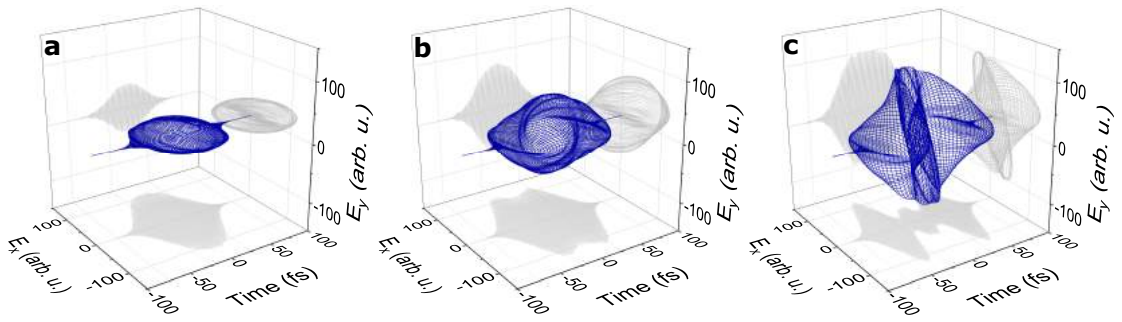

Figure 3.13: Computed electric fields of HH5 with $\epsilon = 0.6$ and $\theta = 75°$. Peak electric field strengths 0.8 GV/m (**a**), 1 GV/m (**b**) and 1.3 GV/m (**c**).

field strengths: Polarization states that are evolving over the course of the pulse. This effect will be used synonymously with 'depolarization'. The polarization state is well defined at any time but does not stay constant over the course of the pulse (see Fig. 3.13), hence it seems depolarized when averaging over a pulse as it is usually done experimentally.

So far, there have not been deep investigations on depolarization in solid HHG, apart from the fact that it has been identified in TDDFT-calculations in Si and MgO [105] as well as in TDSE-calculations in gapless graphene [172]. No experimental signature of depolarization in solid HHG has been reported by now. The decreasing degree of polarization in Fig. 2.23 is an indication of depolarization however there, the experimental error is rather high, which prohibits a statement with certainty. There were also no obvious signatures of depolarization in the ZnO-measurements in Fig. 2.30.

Here we see that depolarization enters already with a simple single-particle one-band computation in ZnS. Fig. 3.13 shows the time-dependent electric field, band-pass-filtered around HH5 for $\epsilon = 0.6$ and $\theta = 75°$ for three driving field strengths. Notably, especially for the highest field strength in Fig. 3.13**c**, the polarization state of the harmonic is varying with time. This does not come as a surprise: As we have seen, the polarization state depends on the driving field strength. A laser pulse has a time-dependent amplitude and therefore, by definition, different driving field strengths over the course of a pulse. This means, electrons are driven to different regions in the Brillouin zone over the course of the pulse where the conduction band curvature can have completely different values. Therefore it makes sense that harmonics show time-dependent polarization states and that this phenomenon increases in magnitude with E_0.

Since we have the luxury of having both simulated as well as experimental data (Sec. 2.4.3) at our disposal, we can compare the simulation results with the experiment. We will do this later to study the ellipticity but for now, let us look exclusively at the degree of polarization (DoP). We can calculate the Stokes parameters from our simulation results by propagating the electric field of an harmonic through the according Jones matrices of a QWP and a polarizer (compare Sec. 2.3.3) and afterwards integrating over time. This gives us the values plotted

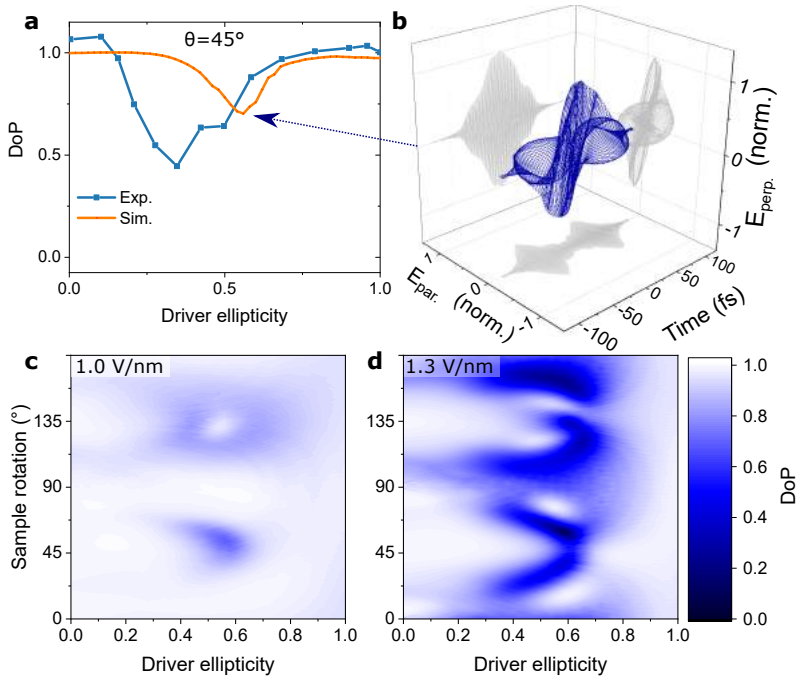

Figure 3.14: **a**: Comparison of the DoP obtained by experiments (see Sec. 2.4.3) and simulation along $\theta = 45°$ for HH5. **b**: Computed electric field of HH5 along $\theta = 45°$, $\epsilon = 0.54$ with 1 GV/m. **c**&**d**: Calculated DoP for various θ and ϵ for two different driving field strengths (HH5). Adapted from Ref. [181]

in Fig. 3.14**a**, where also the experimentally obtained values are plotted. Quite astonishingly, both experimental and calculated data show a clear decrease in the DoP for certain ϵ. While in Sec. 2.3.3, the DoP was decreasing with increasing ϵ, it was there not backed by theory, so the interpretation of this phenomenon was a bit vague. Here, even the simple intraband-only model predicts a depolarization effect, which we do also observe in the experiment. The electric field at the simulated point of lowest DoP is shown in Fig. 3.14.

All the electric fields plotted so far are symmetric with respect to $t = 0$. This makes sense since there are no effects included in this model to break this symmetry and because in this model, the electron is already in the conduction band before the pulse arrives. In a real system the laser promotes electrons to the conduction band and therefore the emitted electric field would be 'switched on' when the first electrons start to oscillate. On the trailing edge of the pulse no electrons get promoted to the conduction band anymore and therefore, the emitted field would fade out, depending on the dephasing time of the system. These two effects should effectively gate the emitted electric field around the center of the pulse which should increase the DoP when compared to experiments. However, as we see in Fig. 3.14**a**, this is not the case. In fact, the experimental DoP is reduced stronger than in the single-particle single-band model. This could mean that some other relevant dynamics cause depolarization too. Of course, the hole oscillating in a valence band would work in exactly the same way as the electron, so depolarization

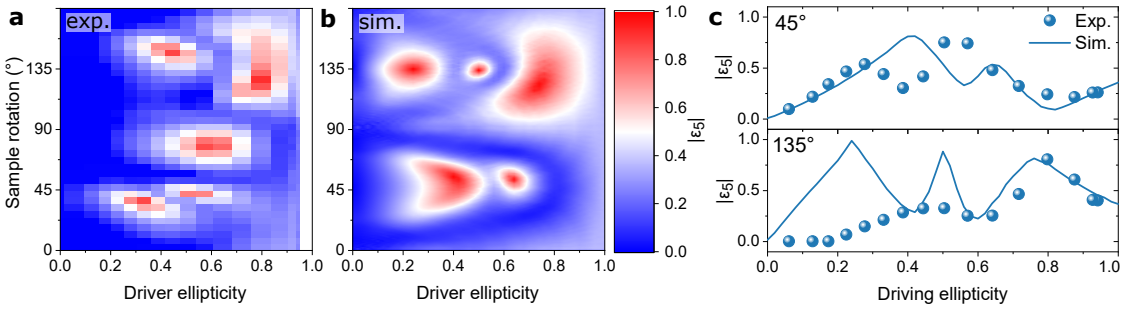

Figure 3.15: Comparison of the $|\epsilon_5|$-map obtained from ZnS between experimental (**a**) and computed (**b**) data. **c**: Line-outs along the major symmetry directions 45° and 135°.

would also be expected to happen there. Also the sub-cycle ionization dynamics could send the electrons along different paths through the Brillouin zone depending on their time of ionization, which could also act as a depolarization mechanism. More work is needed in that direction to distinguish these effects.

As has been said before, the DoP is strongly intensity dependent. Figs. 3.14**c** and **d** plot the calculated DoP depending on ϵ and θ for two different driving field strengths. It is apparent that the DoP is far stronger reduced in the case of the higher field strength. There, the harmonic is even partly depolarized with $\epsilon = 0$ for certain θ. This significant prediction should be confirmed or disproved in future work in solid HHG before further assuming harmonics to be fully polarized, as it is usually done.

3.3.3 Comparison between computed and experimental data

Let us now compare our simulated ellipticity data with the experimental data presented in Sec. 2.4.3. Because the even harmonics are missing in the computation, they will not be looked at, although their behavior - especially the observation of high $|\epsilon_n|$ for linear driving - seems very interesting and needs to be investigated and understood in future work. Here we will use the simulated data for 1 GV/m which is the same as the estimated experimental peak electric field strength in matter.

Figure 3.15 shows the experimental (**a**) as well as the simulated data (**b**) of $|\epsilon_5|$. Note that, in order to match θ of simulation and experiment, 90° has been added to θ of the computed data with respect to the results shown in the last sections.

Due to the zinc-blende crystal structure, neither the experimental nor the calculated data show a four-fold symmetry. Another aspect of this crystal structure is that harmonics are elliptically polarized with circular excitation, as has been argued already in Sec. 2.4.3. This is well captured by the one-band computation. For elliptical excitation, CHED appear both for simulated as well as experimental data. Some features of the experimental data are qualitatively well reproduced in the simulations. This is especially true for the asymmetric elongated island around $\epsilon = 0.8$ and $110° < \theta < 150°$. Also the two islands along $\theta \approx 45°$ can be found

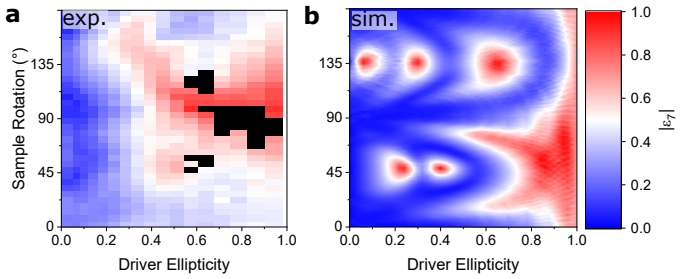

Figure 3.16: Comparison of the $|\epsilon_7|$-map obtained from ZnS between experimental (**a**) and computed (**b**) data. Data points where the signal to noise ratio is below 2.57 times the standard deviation are marked in black.

both in experiment and simulations. The experiments show a circularly polarized HH5 for $\epsilon \approx 0.6$, $\theta \approx 80°$ which is not covered in the simulation.

In Fig. 3.15**c**, line-outs along the major-symmetry directions $\theta = 45°$ and $\theta = 135°$ compare experiment to the simulations. For $\theta = 45°$, the overall shape is reproduced in the simulation, although the precise positions and magnitude of the $|\epsilon_5|$-peaks are slightly off. For $\theta = 135°$, the simulated results only reproduce the experimental data well for $\epsilon > 0.6$. The peak at $\epsilon \approx 0.2$ does not appear in the experiment at all and also the sharp peak at $\epsilon = 0.5$ is missing.

Since the peak electric field strength scales with $\sqrt{1/(1+\epsilon^2)}$, it can be expected that the number of electrons in the conduction band increases with lower ϵ. This will have an impact, both because of the sub-cycle ionization dynamics manifesting itself in the high-harmonic response [180] as well as due to the increasing impact of dephasing that scales with $\sqrt[3]{n_e}$, when n_e is the electron density [184]†. Because the simulations describe a single particle and no interband transitions, especially the low-ϵ-regions have poor agreement to the experiment. For higher ϵ, experiment and simulations seem to match rather well. Apart from the lobe at $\epsilon \approx 0.6$, $\theta \approx 80°$ that does not appear at all in the simulation, an overall qualitative agreement can be ascertained for the below-band-gap harmonic HH5. Quantitative discrepancies are no surprise given the simplicity of the model and the complexity of the dynamics.

Another interesting result is the comparison between experiment and simulation for HH7 (Fig. 3.16). Here, the simulated map looks qualitatively similar to the previously discussed maps. It exhibits rather sharply defined islands of CHED and - as the higher harmonics do in the tight-binding case - it shows more islands than HH5. The experimental map however, looks systematically different. Here, we can observe much more elongated regions of high $|\epsilon_7|$ and no sharp islands appear at all. HH7 is above the band gap and therefore it is generated by coupled intraband and interband dynamics. It is very clear that the intraband calculations do not reproduce the experimental data. Note that also for silicon, HH7 was above the band gap and had a high JDOS. And also there, this harmonic had similar elongated regions of CHED that have not been seen in the intraband simulations,

†Note that in a tunneling process, n_e increases exponentially with the driving field strength [15].

while HH5 and HH9 showed CHED that depended very sensitively on ϵ and θ.

This could suggest that HH7 both in Si and ZnS is generated predominately by interband dynamics and that one can use this kind of analysis to make statements about the generation mechanism of the harmonics. To ultimately verify this hypothesis one should include also the interband dynamics in the computations by calculating the full semiconductor Bloch equations and see if CHED can also appear with interband dynamics and if so, under which conditions.

To conclude this chapter, the single-particle intraband-only calculations have revealed some fundamental insights about the polarization-state-resolved response of high harmonics from solids with elliptically polarized driving fields. It is especially noteworthy that sharp CHED can be assigned to intraband dynamics. But also features like a rotation of the major axis and an intensity-dependence can be observed from pure intraband dynamics. Of special significance is also the effect of depolarization that is predicted by the simple intraband-only model and could even be found in experimental results. In future work it would be interesting to include the Berry phase and confirm its influence on both the odd and even harmonics. Finally, including the interband dynamics and investigating their influence on the harmonics' polarization state would be very helpful in order to determine which generation mechanism causes which kind of signatures in the maps of $|\epsilon_n|$.

Chapter 4

The high-harmonic cutoff with elliptically polarized pulses

We have now seen both experimentally and theoretically that elliptically polarized laser pulses can drive high harmonics from crystals in ways that are unexpected when compared to the dynamics of gas HHG. So far, we have only studied relatively low-order HHG. This is because this wavelength range allows to study a large variety of properties with relatively simple setups. It is also because a OPA source at 2.1 μm was readily available at the start of the corresponding project. Although the dynamics do not fundamentally differ between HHG in the visible and in the EUV-domain, it is a valid criticism that harmonics in the visible domain are not too useful from a source perspective, that is, there are far brighter and simpler sources conventionally available in that wavelength range. Another drawback in the observed visible wavelength range with the driving wavelength that we used was that we could only observe relatively few orders at the same time. Moreover, the higher energy region exhibits some important characteristics that are simply not accessible in the visible domain. These are for instance the emergence of multiple plateaus as well as the cutoff region. Both provide important information about the underlying HHG mechanism. Consider the cutoff: In gas HHG, the cutoffs'

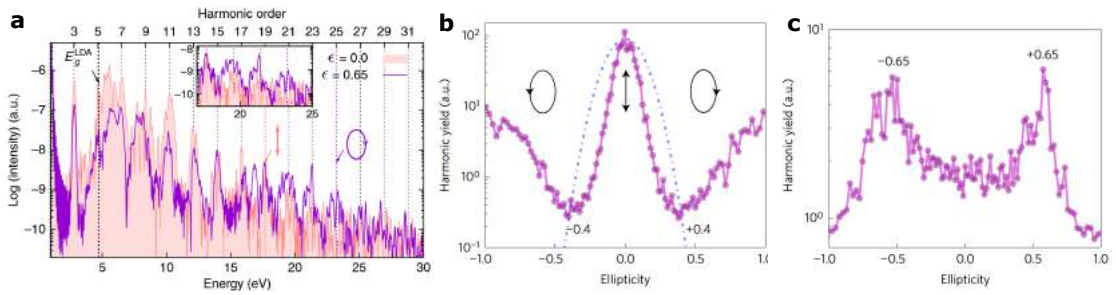

Figure 4.1: **a** Calculated HHG spectrum from MgO along ΓK with $\epsilon = 0$ and $\epsilon = 0.65$ by Tancogne-Dejean *et al.* (Adapted from [105]). Experimental harmonic yield versus driving ellipticity for ΓX (**b**) and ΓK (**c**) obtained by You *et al.* from MgO. Adapted from [45].

dependence on the driving laser parameters served as an important building block to the development of the corresponding three-step and full quantum model.

The cutoff in solid HHG is again a less obvious quantity than in gas HHG. Its wavelength-dependence is yet undetermined and even though many quote the linear dependence of the cutoff on the driving field strength, it has also been shown that the cutoff can increase in steps as soon as electrons gain enough energy to be promoted to higher lying conduction bands [86]. Moreover, in 2017, Tancogne-Dejean *et al.* predicted by means of TDDFT-calculations that the high-harmonic cutoff from MgO could be enhanced by 30 % when going from $\epsilon = 0$ to $\epsilon = 0.65$ with major axis along ΓK (Fig. 4.1**a**) [105] . This came as a surprise since one would expect the cutoff to *decrease* with increasing ϵ if it depended on the maximum electric field strength. The conditions for which Tancogne-Dejean *et al.* ran the simulations were exactly the conditions for which You *et al.* experimentally demonstrated for the first time that also the harmonic yield would be enhanced by more than a factor of two with elliptical excitation (see Fig. 4.1**b** and **c**) [45] .

In this chapter, we aim at exploring the cutoff of solid HHG under elliptical excitation and to verify the prediction of Tancogne-Dejean *et al.* In order to do so, an appropriate vacuum beam line had to be set up, which will be presented in Sec. 4.1. The experimental results will be discussed in Sec. 4.2. This chapter contains, especially on experimental side, joint work with Dr. Haoyu Huang.

4.1 Experimental setup

The full experimental setup is sketched in Fig. 4.2. To summarize, a Ti:Sapphire system pumps a three-stage-OPA which converts the 800 nm, 4.5 mJ to tunable 1200 nm-1600 nm, 0.5 mJ. The downconverted light is transmitted through a WG-P/HWP/QWP combination as it has been described in detail in Sec. 2.1.5. The pulses are then focussed onto a sample in a vacuum chamber. The hereby generated XUV-radiation passes on a grating with 300 grooves/mm. Metal filters can be inserted at the entrance of the spectrometer with a filter wheel. A microchannel plate (MCP) and phosphor screen assembly converts the spectrally dispersed XUV-photons to green photons. Those are then captured by a *Basler acA3088* camera and processed afterwards on the computer. The experimental control and processing of the data is done in a MATLAB routine that is an adjusted version of the program presented in Sec. 2.1.3. Note that both the grating and the MCP have a strongly decreasing sensitivity for photon energies lower than 12 eV. With the two setups of this thesis combined, we are therefore not able to capture the photon energy region between 6 eV and 10 eV.

A lab-specific challenge of this setup lies in the fact that the pump laser is placed on another table, 6 m away from the optical table on which the OPA-source and the vacuum setup are placed on. The beam is kept with excellent beam quality by relay-imaging it through a 6 m long metallic tube that is kept under vacuum, with anti-reflection-coated entry and exit windows. The compressor of the Ti:Sapphire system can be tuned such that it compensates the additional chirp introduced by

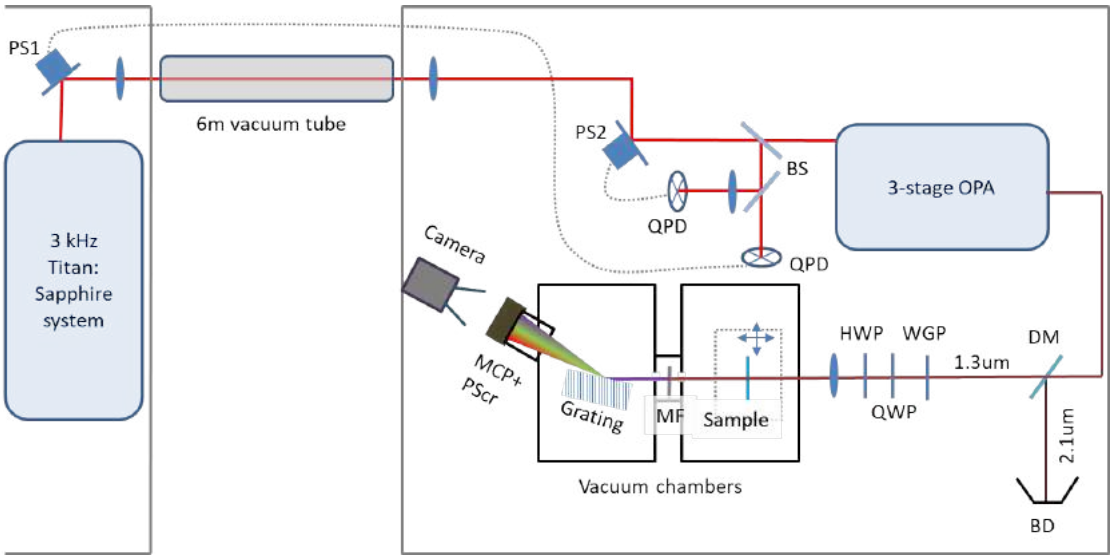

Figure 4.2: Schematic experimental setup of the solid HHG XUV beamline. PS: Pointing stabilizer, QPD: Quadrant photodiode, BS: Beam sampler, LP: Long-pass filter, DM: Dichroic mirror, BD: Beam dump, WGP: Wire-grid polarizer, HWP: Half-wave plate, QWP: Quarter-wave plate, MF: Metallic filter, MCP: Microchannel plate, PScr: Phosphor screen

the windows and the long-focal-length lenses for relay imaging. A beam-pointing stabilizing system with one motorized mirror placed on each optical table provides accurate pointing over long periods of time. Both optical tables are connected mechanically and floating.

4.1.1 OPA-source

The OPA has been set up by Dr. Liwei Song and Dr. Haoyu Huang and is sketched in Fig. 4.3. It is based on an OPA-design initially presented in Ref. [187] and is described in detail in Ref. [186]. For details, those references should be consulted. Let us only discuss the most important aspects here.

The 800 nm-pump pulses are divided into four parts with three beam splitters. The smallest portion of the pulses are focused onto a 2-mm-thick sapphire plate in which a white-light continuum (WLC) is generated. This continuum is amplified in three subsequent BBO-based OPA stages. Due to the birefringent phase-matching, the amplified wavelength can be tuned by rotation of the BBO's and at the same time controlling the pump-seed delay in each delay stage. At the output of the three stages, signal and idler pulses have tunable wavelengths of 1.2-1.6 μm and 1.6-2.4 μm respectively. The output energies are on the order of 0.5 mJ at 1.44 μm with idler pulses of 0.4 mJ at 1.8 μm. The pulse duration of the signal pulses is 34 fs at 1.32 μm wavelength, as it has been determined by FROG (see Fig. 4.4).

Note that the pulse energy is fifty times larger than what has been used in Chapter 2 and the pulses have less than half the pulse duration. This means, less

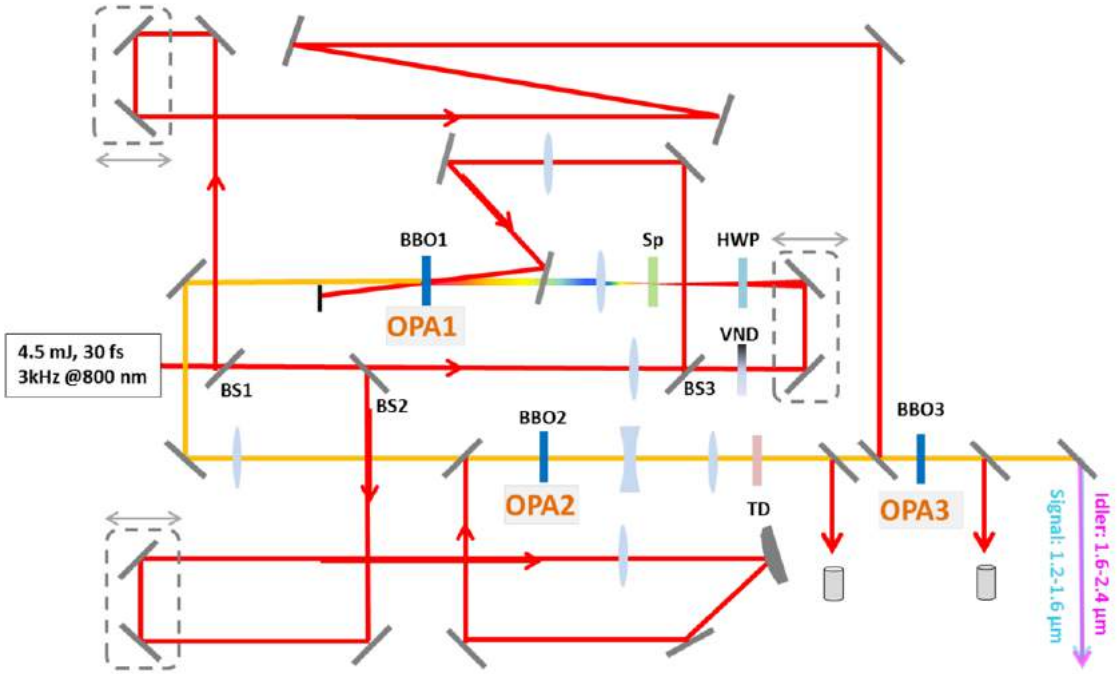

Figure 4.3: Schematic of the OPA. VND: Variable neutral density filter, SP: 2mm-Sapphire plate, TD: Time delay crystal. Figure from [186]

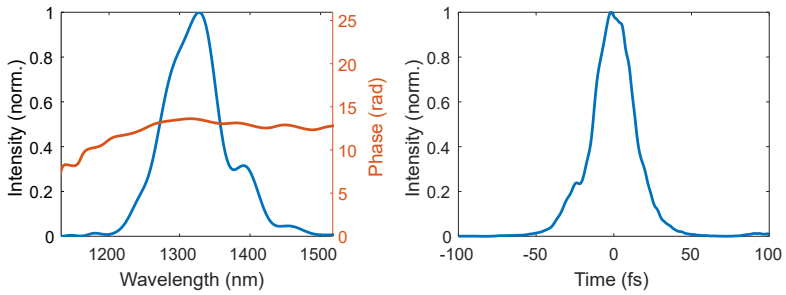

Figure 4.4: FROG reconstruction of the OPA.

focusing is necessary to reach the same peak intensities, making more emitters contribute to the HHG process which in turn should increase the HHG yield. The higher pulse energy at disposal combined with the shorter wavelength means also that higher band-gap materials can be used as samples for solid HHG. Because the laser damage threshold of a crystal with femtosecond pulses is usually determined by the amount of ionized electrons, materials with larger band gaps have higher damage thresholds. This allows then to drive electrons with higher peak intensities in the HHG process which in turn is the reason why higher band gap materials usually lead to higher cutoffs in solid HHG (compare Fig. 3 in Ref. [90]).

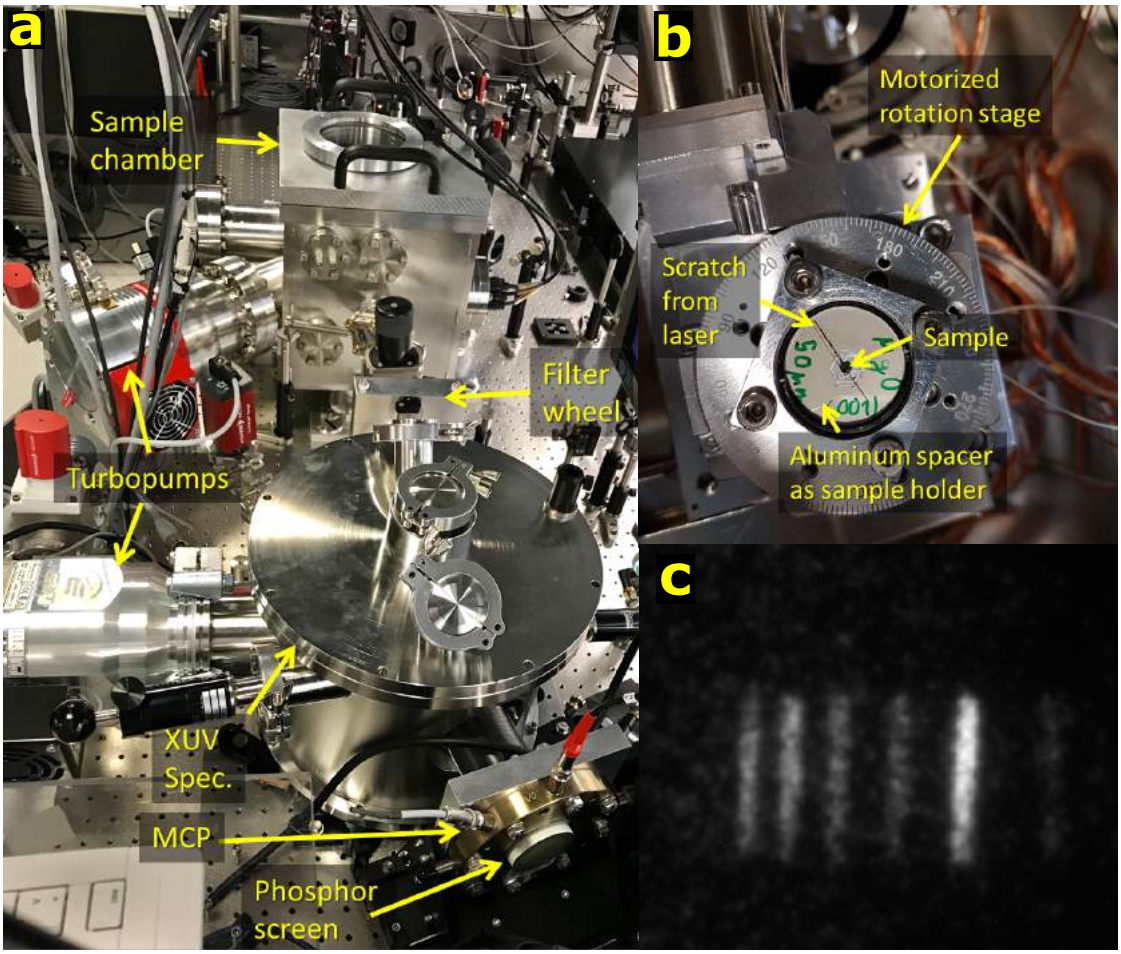

Figure 4.5: **a**: Annotated photo of the vacuum chambers and components. **b**: MgO sample glued to a holey Al-spacer. The spacer is mounted on a motorized rotation stage. One can also see a scratch on the Al-spacer that has accidentally been written on it by the laser. **c**: Photograph of the Phosphor screen at the output of the spectrometer, showing an HHG spectrum, in this case generated by 800 nm pulses from SiO_2.

4.1.2 Vacuum setup

Investigating EUV-harmonics requires a vacuum beam line since air, and any other gas, absorbs the photons of these energies. The vacuum setup is depicted in Fig. 4.5**a** and consists of two separate vacuum chambers. The first chamber houses the sample in which high harmonics are generated. The sample is mounted in a motorized rotational stage which itself is mounted on two motorized translation stages that allow to move the sample along the laser propagation direction and horizontally perpendicular to it (see Fig. 4.5**b**). The second chamber is the *251MX*-EUV spectrometer from *McPherson*. It houses a flat field, gold-coated, grating with 300 grooves/mm which diffracts the radiation onto a MgF_2-coated Chevron-type MCP from *Photonis*.

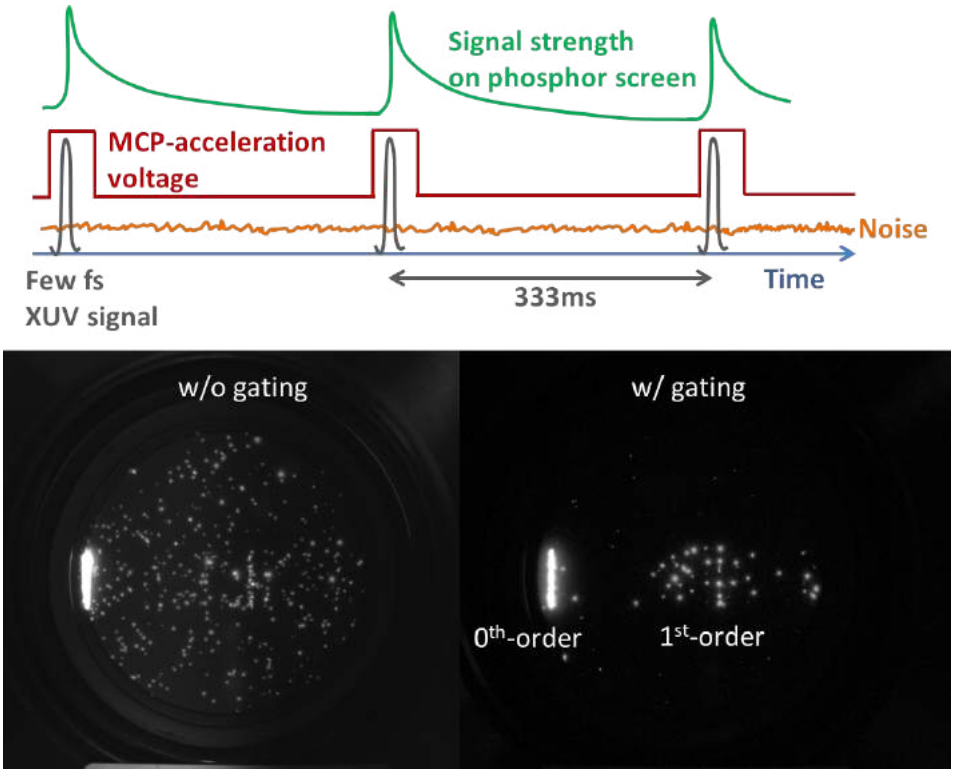

Figure 4.6: Top panel: Schematic working principle of the gating of MCP-acceleration voltage in relation to XUV-signal, noise and phosphor fluorescence screen. Bottom panel: The recorded signal on the MCP with and without gating. In this case the signal is XUV-emission from NiO with 1.3 μm.

Two turbomolecular pumps, one for each chamber, are connected to a roughing pump for each turbo. This way, the vacuum can be maintained in both chambers individually which is required due to the filter that can be inserted between the chambers. In practice, the pressure goes down to the 5×10^{-7}-mbar-level which is more than sufficient for absorption to be non-existent as well as to have the MCP run safely.

4.1.3 Gating

The Chevron-type MCP that is used in this setup is an extremely sensitive device, converting XUV photons to green photons with a gain of $> 10^7$ [188]. This means it is susceptible to noise and this noise does not only consists of photons but also of particles. We have observed the noise to increase strongly when the laser was switched on which means it is either from scattered photons or from ejected particles due to these scattered photons or from the sample directly. An elegant solution to decrease the noise lies in gating of the MCP. Gating can be done by using the electronic trigger pulses of the laser as inputs in a high voltage switch. This device can alter the acceleration voltage of the MCP to a value below and above what is required in order to reach significant signal gain. By setting the

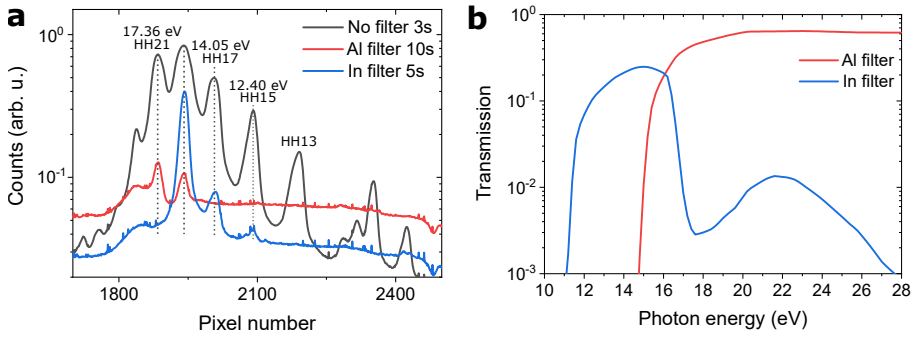

Figure 4.7: **a**: Recorded spectra of MgO with 1.5 μm driving wavelength (Photon energy 0.827 eV) without filter as well as with Al and In filters. Filters are 200 nm thin. In the legend, also the integration times are stated. **b**: Calculated transmission of 200 nm-thin Al and In sheets. Data from Ref. [189].

precise timing of the laser trigger pulses with a delay generator, the MCP can be 'switched on' for durations that are as short as few tens of nanoseconds. This inhibits the acquired noise-related photons and particles significantly, as can be seen in Fig. 4.6.

4.1.4 Calibration of the spectrometer

In order to convert a photo of the MCP's phosphor screen (Fig. 4.5**c**) into a spectrum, two things need to be done. First, the photo is a two-dimensional data set in which the horizontal axis x corresponds to the dispersed photon energies while the vertical axis y carries information, e.g. about the beam size and also possibly other parameters. We do not need the latter and therefore, we can integrate over y:

$$\mathrm{spec}(x) = \sum_{y_{\min}}^{y_{\max}} \mathrm{data}(x, y). \tag{4.1}$$

$y_{\min}$ and $y_{\max}$ are chosen to contain slightly more than the full vertical extend of the harmonic peaks. Since the noise is heavily reduced due to the gating, the data is not affected much by integrating over more than a harmonic peak vertically. However, it ensured that we have captured the full signal of the harmonic peaks.

The calibration of horizontal pixel number x to a representative energy value is done by recording spectra from MgO with and without metal filters. Fig. 4.7**a** depicts three spectra obtained from MgO with 1.5 μm-driving wavelength and 70 μJ pulse energy. Both filters transmit a harmonic peak around pixel number 1950. Comparing to the transmission curves in Fig. 4.7**b** and taking into account that our fundamental photon energy is 0.827 eV, we find that it can only be HH19 which is transmitted by both filters. HH19 lies at $19 \times 0.827\,\mathrm{eV} = 15.71\,\mathrm{eV}$. Knowing one harmonic order one can associate all other peaks by presuming them to be separated by two fundamental photon energies (for a centrosymmetric material

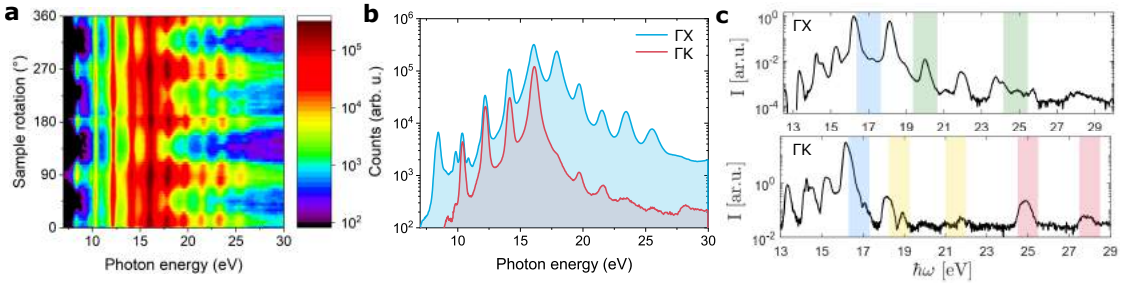

Figure 4.8: **a**: Rotation-dependent experimental spectra from MgO. **b**: Two experimental spectra from MgO along its major symmetry directions. These spectra are line-outs of the spectra in **a** along 90° (ΓX) and 135° (ΓK). **c**: Experimental spectra from MgO presented by Uzan *et al.* along ΓX and ΓK (**c** is adapted from [152]).

only odd harmonics exist). This way we can fit pixel number to photon energy and have the spectrometer calibrated.

4.2 Experimental results

Let us now turn to the experimental investigations. The results presented here revolve around MgO which, besides SiO_2, has been the material of choice for relatively many XUV HHG-experiments in the recent past [45, 128, 143, 152, 190]. We will first discuss linearly polarized driving and make some general remarks about the hereby observable HHG-response of MgO. Then we will direct our view towards the cutoff, its dependence on the field strength and, finally, also the ellipticity.

4.2.1 Anisotropy of HHG from MgO

In this section, a 10 μm-thin (100)-cut MgO sample from *SurfaceNet* is used. The FWHM beam diameter of the laser in the focus is 60 μm, as has been measured with a camera. This leads to a peak intensity in vacuum of 38 TW/cm^2. The camera collects 60 frames of 50μs each and the average over all frames is calculated in post processing. It might seem strange to integrate for shorter durations than the repetition rate of the laser but note that the MCP is a slow device with a ms-level decay time. Averaging in this way is in fact advantageous. It increases the dynamic range of the camera because the pixels with high counts do not saturate as fast while the signal-to-noise ratio (SNR) increases for pixels with relatively few counts. The total integration time is 3 s and hence, the signal is acquired over 9 shots.

Figure 4.8**a** depicts high-harmonic spectra acquired from MgO for a full rotation of the crystal. Here, the driving pulses are linearly polarized. It is clearly visible that the sample exhibits a 90°-periodicity which points to the cubic crystal structure of MgO. Furthermore, the periodicity is a signature that the samples'

surface quality is reasonable, as the laser typically hits different spots on the sample when the sample rotates. Clearly, both the yield of the harmonics and the cutoff are greatly enhanced along 90° and corresponding sample directions. In correspondence with earlier publications on MgO [45, 152] we identify the high-yield-direction 90° as ΓX and the low-yield-direction 135° as ΓK.

In Fig. 4.8**b** two line-outs of the previous sample-rotation scan show the high-harmonic spectra along the two major symmetry directions ΓX and ΓK. As was argued before, the yield along 90° is far higher. Also, above 20 eV there is a second plateau. The two small peaks in the measurement of ΓX around 10 eV are likely the second order of the grating. Note also that 10 eV lies at the lower edge of the detection range both from the grating as well from the MCP's sensitivity and that these spectra have not been calibrated for the spectral response of the spectrometer system.

One should appreciate the relatively high SNR and the high dynamic range of these spectra. The second plateau does not appear so clearly in the existing publications on MgO. Beneficial to the SNR are the relatively thin sample (note, for instance, Ref. [45] used a 20 times thicker sample) and the gating of the MCP. In Ref. [152], a weak second harmonic to the fundamental altered the spectra and they used this time-dependent alteration as a lock-in measurement for signal enhancement. The spectra they obtained with this method are shown Fig. 4.8**c**. The driving conditions are similar to those of the here performed experiments. In general, the spectra of Uzan *et al.* are similar to those presented by us in Fig. 4.8**b**. Along ΓX, they show a second plateau, although their spectrum shows some unique behavior of the relative harmonic peak strengths which was explained with singularities in the dynamical JDOS. In our experiment, we do not clearly observe those. Along ΓK some important differences can be seen. While our spectrum shows two distinct peaks around 19 eV and 21 eV, the spectra of Uzan *et al.* lack the clear peak structure. They present peaks at 25 eV and 28 eV and at least the peak around 28 eV seems to also weakly appear in our measured spectrum. This peak will play an important role later on.

Overall, the stated discrepancies between Fig. 4.8**b** and **c** are not significant, considering the strong non-linearities at play here. The main reason to compare these two spectra here is to relate the here acquired spectra to existing work on MgO, of which Uzan *et al.* showed the cleanest spectra. The spectra measured by us are by no means less rich in information.

4.2.2 The cutoff with linear polarization

Let us now turn towards the cutoff in more detail and first study its dependence on the pulse energy. Fig. 4.9**a** depicts the recorded high harmonic spectra from MgO versus the driving pulse energy. This data is acquired with linearly polarized driving pulses, polarized along ΓX. It was not possible to apply higher pulse energy than 80 μJ without irreversibly damaging the sample. The plot resembles the simulated data that is shown in Fig. 3.3 in the sense that the cutoff seems to increase linearly with the field strength (or square root of pulse energy). However,

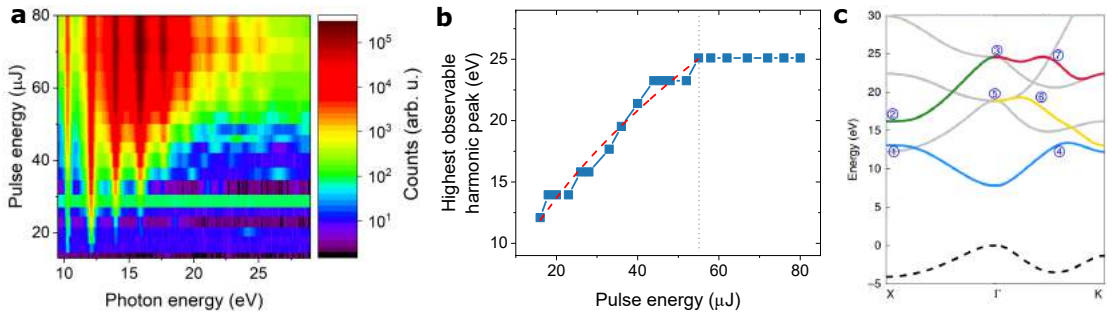

Figure 4.9: **a**: Measured high-harmonic spectra along ΓX in dependence of the driving pulse energy. **b**: Plot of the highest observable photon energy (cutoff) along ΓX versus the driving pulse energy. The red dashed curve is a square-root regression taking only into account energies below the vertical dotted line. **c**: Band structure from MgO along ΓX. The colored conduction bands are the ones that dipole couple to the dashed valence band. **c** is adapted from Ref. [152].

above 50 μJ, the second plateau appears and the cutoff does not increase visibly with increasing pulse energy anymore. Such behavior could not be seen in the intraband-only simulation.

In Fig. 4.9**b**, the highest observable harmonic peak energy is plotted versus the driving pulse energy. This enhances the visibility of the previous statement that the cutoff increases until a certain point above 50 μJ and no further increase is observed above that. The red dashed line is a square-root regression as this dependence has so far been reported from solids [38, 132] and this is also the dependence we have found with the intraband-only simulations in Sec. 3.2.1. Note that the red dashed line takes only values into account that are below the saturation threshold at 55 μJ pulse energy.

What happens to the cutoff when the 25 eV-photon energy threshold is reached can be best understood when considering the band structure, which is shown in Fig. 4.9**c**. The two conduction bands (1 and 2) that are dipole-coupled to the valence band (dashed curve) form the first (< 18 eV) and second (< 25 eV) plateau. There are no higher lying bands that dipole couple to the valence band in that energy region. Hence, the interband mechanism can not produce harmonics that are higher than the maximum band gap of the conduction band 2, which is 25 eV. This is the reason for the saturation behavior of the cutoff in Fig. 4.9**c**. It should be mentioned that this discussion ignores the contribution of intraband-dynamics. Those could in principle still produce higher photon energies than the maximum band gap. The fact that this is not observed indicates that intraband dynamics are not the dominant mechanism for these driving conditions in MgO. This analysis thus supports the corresponding statement made in Ref. [152].

4.2.3 Interlude: Induced birefringence

In the following experiments, the samples' thickness is of enormous importance and this section shall be used to demonstrate why. Due to reabsorption, the detected harmonics stem from the last tens of nanometers in the sample. Consequently, the driving pulse has propagated through most of the samples' thickness and thus suffered from propagation effects when generating harmonics. In the linearly polarized case, propagation effects affect mostly the chirp and thereby the pulse duration. However, with elliptical polarization, the polarization state can be altered. One effect to do this is nonlinearly-induced birefringence. When the refractive index is intensity dependent, induced birefringence naturally arises since one axis of the driving ellipse has a higher peak intensity than the axis perpendicular to it and thereby both axes experience different refractive indices. This effect shall be discussed here in detail. One should keep in mind that there are also other non-linear effects that can alter the polarization state, for instance cross-phase modulation. Even though they will not be discussed here, those will add to the nonlinear phase that is discussed in this chapter, increasing the effects elaborated on here even further.

Let us choose the coordinate system such that x refers to the major axis and y to the minor axis of the driving fields' polarization ellipse. The introduced phase shift $\Delta\phi$ of the x- to the y- component due to differing refractive indicees n'_x and n'_y can be calculated with

$$\Delta\phi = kL(n'_x - n'_y). \tag{4.2}$$

L denotes the samples' thickness. We can insert the equation for the nonlinear refractive index $n'_i = n_0 + n_2 I_i$ where n_0 is the linear refractive index, n_2 the nonlinear refractive index and I_i the peak intensity along axis i. We assume here that the indicees n_0 and n_2 are isotropic. Then

$$\Delta\phi = kL(n_2 I_x - n_2 I_y). \tag{4.3}$$

When going from vacuum into the sample, the peak intensity I is altered. This is because part of the energy gets reflected but also because the mode shrinks due to the higher refractive index in the sample. The latter effect increases the peak intensity according to $I = \frac{1}{2}\epsilon_0 c n_0 |E|^2$, where ϵ_0 is the vacuum dielectric constant, c the speed of light in vacuum and E the electric field strength. Furthermore, the magnitude of the x- and y-components differ due to the ellipticity ϵ:

$$I_x = \frac{I}{1+\epsilon^2} \quad \text{and} \quad I_y = \frac{\epsilon I}{1+\epsilon^2}. \tag{4.4}$$

Inserting all this in Eq. 4.3, we obtain

$$\Delta\phi = \frac{kLn_2 I_{\mathrm{MgO}}}{2(1+\epsilon^2)}(\epsilon - 1). \tag{4.5}$$

Here, I_{MgO} denotes the intensity in the MgO crystal, i.e. $I_{\mathrm{MgO}} = n_0 I_{\mathrm{vac}}(1-R)$, with R being the reflectance of MgO (7% at 1.3 μm [191]). The nonlinear refractive index

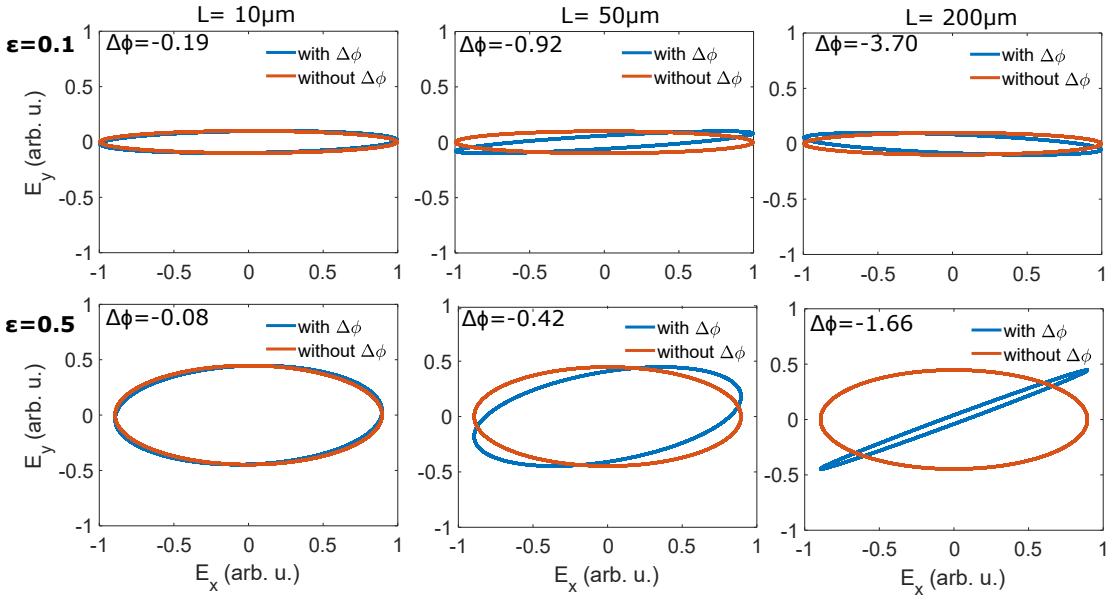

Figure 4.10: Calculated polarization ellipses after propagation through a MgO crystal of thickness L with the driving ellipticity ϵ for ellipses with (blue) and without (red) taking into account the induced birefringence due to the Kerr effect. First row: $\epsilon = 0.1$, second row: $\epsilon = 0.5$. Nonlinear phase shift $\Delta\phi$ in *rad* is given in the corresponding figures.

for MgO is $n_2 = 3.9{\cdot}10^{-20}\,\mathrm{W/m^2}$ at 1 μm wavelength [192] which is sufficiently close to our wavelength for the kind of estimation that we are attempting to perform here.

Figure 4.10 depicts different calculated cases of the polarization ellipse after propagating through a MgO-sample with thicknesses $L = 10, 50, 200\,\mu$m and with the ellipticities $\epsilon = 0.1$ (upper panel) and $\epsilon = 0.5$ (lower panel). The corresponding values of $\Delta\phi$ are given in the respective plots.

For the 10 μm-thin sample, $\Delta\phi$ is very small in magnitude and does almost not affect the corresponding polarization states. This changes with thicker samples. For $L = 50\,\mu$m, the nonlinear phase shift starts to play a role which can be seen in the depicted cases mostly by a rotation of the major axis. Note that $\Delta\phi$ reaches more than $\pi/4$ in the case of $\epsilon = 0.1$. With $\epsilon = 0.5$, the major axis rotates by 30° due to induced birefringence. Propagation effects get even more significant for the thickest case of $L = 200\,\mu$m. Here, $\Delta\phi$ gets so large that the resulting polarization state can be viewed as chaotic, as it sensitively depends on the exact driving conditions. $\epsilon = 0.1$ leads to $\Delta\phi \approx \pi$, which does not alter the polarization state at first glance but flips the helicity. With $\epsilon = 0.5$, the propagation effects convert the incident elliptical wave to an almost linearly polarized, 35°-rotated wave. It becomes clear from this discussion that great care should be taken when assuming a polarization state of the driving field without checking the influence of the sample. Ref. [45] uses a 200 μm thick sample and it is unclear if the authors corrected for the influence of propagation somehow. At least, this is not mentioned. In the

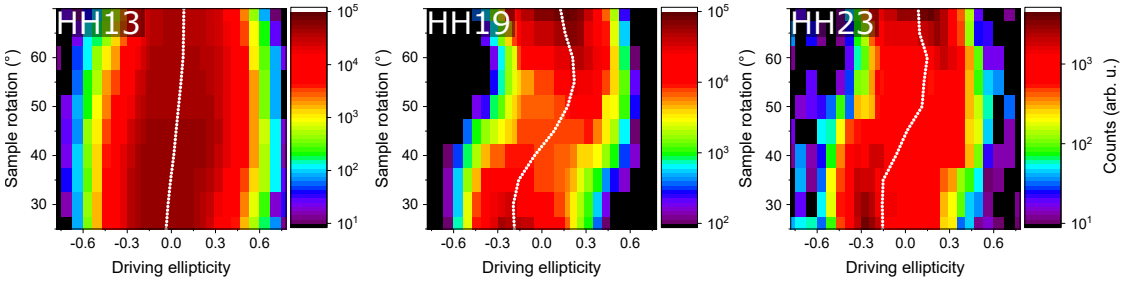

Figure 4.11: Ellipticity-response of HH13, HH19 and HH23 from 10 μm-thin MgO versus sample rotation. The white dotted lines are the centers of mass of the distributions.

next section, a 10 μm thin sample will be used and following from this discussion, propagation effects are negligible in this case.

4.2.4 Introducing elliptical polarization

Let us come back to experimental work. After having investigated MgO with linearly polarized driving pulses, we can now insert the QWP/HWP combination into the OPA's beam path and tune the driving ellipticity ϵ. For every ϵ, a spectrum is acquired, just as has been done extensively in Chap. 2. Here, the polarization states of the emitted harmonics can not be accessed as this would require an additional XUV-polarizer which is not a trivial instrument to obtain [193, 194].

Figure 4.11 shows the high-harmonic response of HH13, HH19 and HH23 from MgO in dependence of ϵ and the sample rotation θ. The samples' thickness is 10 μm and the vacuum peak intensity is again around 38 TW/cm^2. θ is given with respect to ΓX, i.e. $\theta = 45°$ refers to excitation along ΓK. For any θ, the response of HH13 is mostly atomic-like, i.e. the harmonic yield decreases monotonically with increasing ϵ. Consequently, the yield is mostly maximized with linearly polarized excitation and the COM-curve remains close to zero for all sample rotations. For the higher harmonics this is not the case. The yields of HH19 and HH23 both maximize with strongly elliptically polarized excitation. For $\theta = 30°$, for instance, HH19 peaks for $\epsilon \approx -0.21$ and HH23 for $\epsilon \approx -0.27$*.

Along the major symmetry axes, there should be no difference in the harmonic yield between negative and positive ϵ-values. This manifests itself in COM ≈ 0 for $\theta = 45°$ which is a sanity check for our experimental methodology. Also we see again that the yield along $\theta = 45°$ is generally decreased, which corresponds to what has been found before in MgO [45, 105, 152].

Measurements of the ϵ-dependent response of high harmonics from MgO have been performed already in Ref. [45]. A key result there was the asymmetry with respect to $\epsilon = 0$ for excitation off a major symmetry axis. A corresponding plot

*Note that the COM curves plotted here are the original calculated values, while the corresponding COM curves in the silicon work (Fig. 2.12) were multiplied by a factor of 5 to enhance visibility of the asymmetries. Hence, the asymmetric response of these high MgO-harmonics is much stronger than what has been observed from silicon.

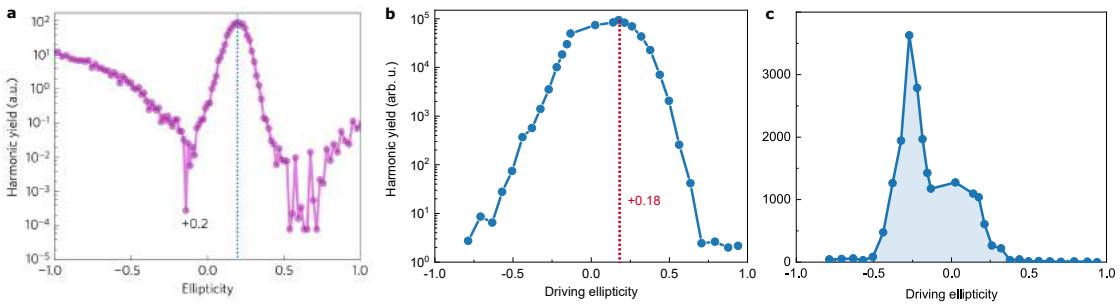

Figure 4.12: Asymmetric ellipticity response of HH19 from MgO. **a**: Plot from You *et al.* in Ref. [45] at $\theta = 15°$, which resembles $\theta = 75°$ in our case[‡]. **b**: Measured ϵ-scan of HH19 at $\theta = 70°$. **c**: Measured ϵ-scan of HH23 at $\theta = 25°$ (note the linear y-axis). **a** reprinted from Ref. [45].

of this is shown in Fig. 4.12**a**, where the response of HH19 is plotted for $\theta = 75°$ [‡]. The plotted ϵ-scan of our measurement at a slightly different sample rotation $\theta = 70°$ is shown in Fig. 4.12. The 5° difference of θ will have an influence, however, as can be seen from the changes in Fig. 4.11, 5° do not change the distribution all-too-much.

Although the similarities between these two plots are scarce, one key characteristic is very similar. That is, both distributions peak at $\epsilon \approx 0.2$. On the other hand, the width of these distribution is extremely different. While the FWHM of You *et al.* is approximately $\epsilon = 0.2$, in our measured data it is double that value. Also, we do not observe that the yield increases again for higher ϵ. This increase is questionable however, because the yield for $\epsilon = \pm 1$ should be the same by rules of symmetry for a cubic system. In the You *et al.* data, there is a difference of two orders of magnitude for left handed and right handed circular polarization. This could be an artifact of improper calibration of the waveplates, possibly amplified with propagation effects as discussed in Sec. 4.2.3, but of course this is only speculation. The discrepancy to fundamental symmetries complicates the interpretation of the corresponding semiclassical trajectory model of You *et al.* [45, 143] because the apparently predicted differences in harmonic yields between LHCP and RHCP (this has not been confirmed by the author of this thesis) contradict fundamental symmetry arguments. In our data, the yield for $|\epsilon| \approx 1$ is below the noise-floor and at least four orders of magnitude below the peak of the distribution. Note that both measurements have approximately the same dynamic range, so it is unlikely that our detection is less sensitive than in the measurements presented by You *et al.* Of course, keeping in mind the induced birefringence discussion for thick samples in Sec. 4.2.3, the ϵ-axis might be significantly off in the data of You *et al.* if they used a 200 μm-thin sample and did not correct for propagation effects

[‡]In the corresponding paper, You *et al.* define the angle in clockwise direction, as can be inferred from Fig. 3 in Ref. [45]. In our experimental work here, we define the angle in anti-clockwise direction because this is the direction the rotation stages rotates the sample. Hence, although the data from Fig. 4.12 is plotted for $\theta = 15°$, here, it becomes $-15°$, which equals $\theta = 75°$ due to cubic symmetry.

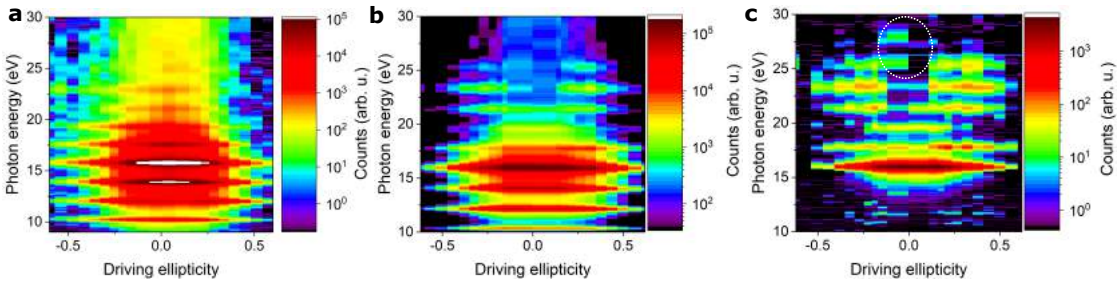

Figure 4.13: High harmonic spectra in dependence of ϵ with driving major axis along ΓX (**a**) and ΓK (**b**). **c**: Same as **b** but with Al filter inserted in front at the spectrometer entrance.

properly.

We should not forget to emphasize a remarkable characteristic that both You *et al.* and we observe - in our case from HH19 and HH23. That is, these harmonics can be increased significantly when going from linear to elliptical excitation. This is especially pronounced for HH23 in our case, as is shown in Fig. 4.12**c** along $\theta = 25°$. Here, the yield of HH23 can be enhanced more than threefold when increasing ϵ from 0 to 0.25. As stated before, HHG from MgO seems to be interband dominated [152]. However, the ϵ-response of these harmonics is hard to comprehend with an interband recollision-type picture. If the yield increases with elliptical excitation, does this mean that the hole left behind in the valence band just moves in the right way such that electron and hole recollide, somehow more efficiently than with linear polarization? Or could it be that some intraband dynamics become important in these cases? Perhaps the polarization of the harmonics carry traces of their origin and those characteristics need to be addressed in future work as they could lead to the discovery of some important microscopic, yet unrevealed dynamics.

So far we have looked at the behavior of individual harmonics under elliptical excitation. Let us now complement this discussion by studying the full harmonic spectra. We are doing this, keeping in mind that Tancogne-Dejean *et al.* predicted that the harmonic cutoff could be enhanced from MgO with elliptically polarized excitation along ΓK [105]. Let us first remark that ΓK is the least efficient direction to produce harmonics. As has been interpreted extensively in the intraband-only model with a square lattice (Sec. 3.2.2), when introducing elliptical excitation the nonlinearity of the band that the electrons experience can be enhanced. In the simulation chapter it has been shown that this can manifest itself in a strong increase of the perpendicular field-component. However it is also plausible that this can enhance the cutoff. The flipside experimentally of studying the least-efficient-direction to produce harmonics is that the experimental apparatus needs to be sensitive enough to detect the lowest-possible harmonic yield along ΓK to safely discriminate between an increase of the harmonic yield with ϵ and an increase of the cutoff.

Let us first look at the high-harmonic response to elliptical excitation along

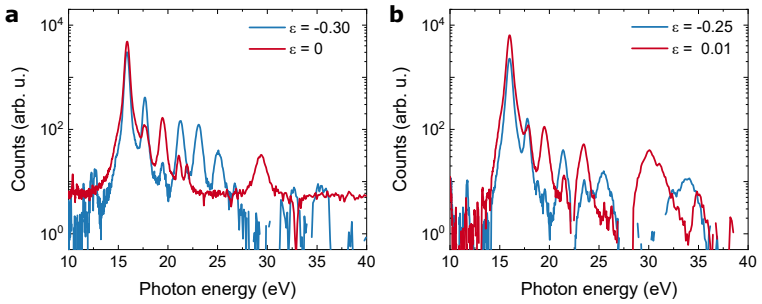

Figure 4.14: Two separate measurements to investigate possible cutoff extension with elliptically polarized pulses. In **a**, the $\epsilon = 0$-curve has been obtained without any HWP and QWP inserted. For **b**, the OPA-system has been realigned and broadband HWP/QWPs have been used. Major axis is polarized along ΓK. An Al-filter is inserted in front of the spectrometer in all four measurements.

the most efficient crystal direction to produce harmonics, ΓX (Fig. 4.13**a**). We can see a clear harmonic spectrum spanning from 10 eV to ∼25 eV, which is the maximum photon energy that we have already mentioned in the discussion of the cutoff under linearly polarized excitation. With increasing $|\epsilon|$, the yield of all harmonics decreases. You *et al.* reported an increase of the yield of HH19 for $|\epsilon| > 0.5$ [45], which is not observed in our data.

When the major axis is oriented along ΓK, the response of the harmonics to elliptical excitation changes (Fig. 4.13**b**). While the harmonics below 20 eV decrease monotonically with increasing $|\epsilon|$, the higher harmonics have a pronounced maximum yield around $|\epsilon| \approx 0.25$. The fact that individual harmonic orders respond differently to ϵ can be anticipated by acknowledging that harmonics below 20 eV are generated from electrons in the first conduction band (band 4 in Fig. 4.9**c**) while harmonics above 20 eV are generated in the second (band 6 in Fig. 4.9**c**). This will naturally alter their response. The particular ϵ-response has been described in Ref. [45] (compare Fig. 4.1**c**) although there, the harmonics peaks at $|\epsilon| = 0.65$. In these measurements, it is not entirely clear if the cutoff is enhanced with elliptical excitation since there is also some signal for low ϵ. Thus a higher SNR is required.

One way to increase the SNR further is to insert an Al-filter in front of the spectrometer because this reduces stray light and signal that is generated from laser-ablated particles. A measurement with Al-filter is shown Fig. 4.13**c**. Here, the same behavior as before can be found with better data quality, however the signal below 15 eV can not be detected. In this figure there seems to be no extension of the cutoff. In fact, quite to the contrary, the highest harmonic can be generated with the lowest ϵ-value, i.e. a harmonic around 28 eV. This measurement had one problem however, because the set of QWP and HWP that have been used did not allow setting precisely linear polarization.

Two more attempts have been made to reach as perfectly linearly polarized pulses as possible while still maintaining a good enough SNR to determine the cutoff energy. In the first approach the QWP and HWP are removed from the

beam line, while the WGP is still left in place. This way, it is guaranteed that the driving field is linearly polarized. In Fig. 4.14**a** this measurement ($\epsilon = 0$) is plotted against an HHG spectrum obtained with $\epsilon = 0.3$, which happens to be the ϵ with the clearest harmonic signal. Also in this measurement it can be seen that the harmonics between 20 and 25 eV can be greatly enhanced with elliptically polarized excitation. Even more so, HH25 and HH27 (23 and 25 eV) do not appear at all in the linearly polarized case. However, with $\epsilon = 0$ there is a clear peak around 29 eV which seems to be HH31. Something similar has been seen and discussed in Fig. 4.13**c**.

In Fig. 4.14**b**, a new set of QWP and HWP have been used that allowed to set linear polarization more precisely. In this case, it is still found that HH27 (25 eV) is greatly enhanced with elliptical excitation but HH25 appears even stronger with linear excitation. Again, there is a rather strong peak with $\epsilon \approx 0$ around 30 eV. More work would be needed to determine if the even higher signal in the elliptically polarized case is in fact a high-harmonic peak or some fluorescence signal.

At this point, the laser system required some maintenance, therefore the experiments needed to be interrupted and there was no time left to continue. With the measurements that have been made one cannot claim the cutoff to be extended with elliptical excitation. Quite to the contrary, the highest peak that consistently appeared, appeared with linearly polarized driving pulses. This peak actually has been discussed also in the work of Uzan *et al.* [152]. There, it has been interpreted as a Van-Hove singularity due to an extremum of the third conduction band (band 7 in Fig. 4.9**c**) around 28 eV. The here presented work seems to support this interpretation.

Chapter 5

Conclusion

This thesis explored the solid-state high-harmonic response to elliptically polarized excitation in three distinguished ways. Let us review the main findings of those before giving an outlook about the implications of this work. First, high harmonics were investigated in the wavelength range of 200 nm and 700 nm, produced with a 2100 nm OPA-source. After having confirmed that harmonics were generated non-perturbatively, two scans were conducted, one of which showed the harmonics' yield and one the harmonics' ellipticity in dependence of the driving ellipticity and the sample rotation. The yield revealed clear non-atomic signatures, i.e. non-monotonic dependence of the yield on ϵ, harmonics peaking for $\epsilon \neq 0$ and - perhaps most significantly - that harmonics were generated in different ways. The low JDOS for HH5 and HH9 indicated that those harmonics were generated mainly by intraband dynamics and this could be seen by a different evolution of the centers of mass of the individual harmonics over ϵ, when compared to HH7 which was generated by coupled intra- and interband dynamics. The full polarization-state-resolved map in dependence of ϵ and θ can count perhaps as one of the most important measurements of this work. Here it was found that circularly polarized harmonics appeared in two ways: With circularly polarized excitation independent on θ (CHCD) and with elliptical excitation with different driving conditions for each harmonic (CHED). While the CHCD were shown to depend on the symmetry class of the crystal and follow the respective selection rules, the behavior of CHED was shown to be sensitive to the precise strong-field dynamics. For instance, it was found that $|\epsilon_n|$ could be strongly altered by variation of the driving intensity. This proved that the polarization states are directly resulting from the microscopic strong-field dynamics. The results were quite well reproduced with *ab-initio* TDDFT simulations by N. Tancogne-Dejean (A. Rubio), indicating on the one hand that the detected phenomena were of microscopic origin and also that the prevailing theory was sufficient to describe the charge dynamics. Experimentally, the measurements were also extended to other crystals, i.e. a different silicon-cut, ZnO and ZnS. In ZnO it was found that all harmonics can be circularly polarized with elliptical excitation simultaneously while for ZnS the even harmonics behaved in an even more distinct way, by having large $|\epsilon_n|$ with linearly polarized excitation.

In order to understand which kind of dynamics might underlie the above described signatures, a single-particle intraband-only model has been developed and applied to a model-type tight-binding band structure as well as to the band structure of ZnS. This model is able to capture some very striking features of the observations, i.e. a rotation of the harmonics' major axis as well as the appearance of CHCD and CHED. It also showed that if the polarization state of a harmonic is dependent on the driving field strength, then a depolarization effect can happen over the course of the pulse due to the everlasting amplitude change. A comparison with the measurements from ZnS showed good qualitative agreement for a below-band-gap harmonic where intraband dynamics are known to dominate. For an above band-gap harmonic, the ellipticity map looked systematically different than predicted with the intraband-only model. This indicated that the origin of high-harmonic emission is imprinted on the ϵ-θ-maps, perhaps allowing to distinguish between different generation mechanisms in solid HHG. Also the depolarization effects predicted by the model were found in the experimental data which shows that one cannot simple assume high harmonics from solids to be fully polarized simply because electrons explore different regions of the Brillouin zone at different times over the course of the pulse.

A vacuum beam line has been set up in order to access harmonics in the EUV-spectral region. In experiments from MgO, the cutoff was shown to increase with the driving field strength until a certain value, above which the cutoff remained constant. This behavior could be explained with the band structure, the saturation arising from missing higher bands. It was pointed out that induced birefringence can become an important issue if samples thicker than 50 μm are used, which could be a serious problem of a previous study. Measurements were compared to this previous study and differences pointed out, especially about the precise shape of an ϵ-scan. A previous theoretical prediction that the high-harmonic cutoff could be extended along ΓK with elliptical excitation could not be confirmed. While it was true that the harmonics between 21 eV and 25 eV could be significantly enhanced with $\epsilon \neq 0$, two harmonics appeared above those, the highest around 28 eV, with linearly polarized excitation. This harmonic was found before by Uzan *et al.* and was explained with a Van-Hove singularity.

The implications of this work are manifold. While the precise dynamics underlying solid HHG are still subject to intense scientific debate, this work suggests that the generation mechanism directly influences the specific ϵ-response. In future work, this could help to bring out the differences between the different generation mechanisms. Since the polarization states of the harmonics are a direct consequence of the microscopic dynamics, measuring those could allow for **k**-resolved tracking of the fastest oscillating currents that ultrafast pulses can generate in solids to date. This becomes particularly interesting in cases where the harmonics lose their well-defined polarization state, i.e. with dynamically changing polarization states over the course of a pulse. More work should be done in this direction as a rigorous comparison to theory could allow to determine parameters like the dephasing time as well as the relative magnitude of hole dynamics of which the influences are still unclear.

From a source point of view, solid HHG could turn out useful in two situations. First, solid HHG can be driven with far lower intensities compared to gas HHG. This allows the usage of different laser sources than in gas HHG. For instance, one could use systems with high repetition rate but relatively low pulse energies, providing a relatively high average power solid HHG source. Also, systems could be cheaper since solid HHG can be driven with laser oscillators directly.

Second, with solid HHG in reflection gaining interest, one could also imagine driving HHG with extremely high pulse energy on a large spot size in reflection, where the thickness of the sample does not play a role. Since the high-harmonic yield should scale quadratically with the beam radius, it should be possible to generate harmonics with high pulse energies from a solid as well, possibly enabling to drive nonlinear dynamics themselves. Combined with the findings of this work, high-harmonic pulses with arbitrary polarization states could be generated that would then enable unique time-resolved studies on chiral systems, magnetic materials or topological insulators with relatively simple and compact setups.

Bibliography

[1] P. A. Franken, A. E. Hill, C. W. Peters, and G. Weinreich. Generation of optical harmonics. *Phys. Rev. Lett.*, 7:118–119, Aug 1961.

[2] W Kaiser and CGB Garrett. Two-photon excitation in ca f 2: Eu 2+. *Physical review letters*, 7(6):229, 1961.

[3] JA Armstrong, N Bloembergen, J Ducuing, and PS Pershan. Interactions between light waves in a nonlinear dielectric. *Physical review*, 127(6):1918, 1962.

[4] Nicolaas Bloembergen and PS Pershan. Light waves at the boundary of nonlinear media. *Physical review*, 128(2):606, 1962.

[5] Elsa Garmire. Nonlinear optics in daily life. *Optics express*, 21(25):30532–30544, 2013.

[6] Nicolaas Bloembergen. Nonlinear optics and spectroscopy. *Rev. Mod. Phys.*, 54:685–695, Jul 1982.

[7] Warren R Zipfel, Rebecca M Williams, and Watt W Webb. Nonlinear magic: multiphoton microscopy in the biosciences. *Nature biotechnology*, 21(11):1369–1377, 2003.

[8] Fritjof Helmchen and Winfried Denk. Deep tissue two-photon microscopy. *Nature methods*, 2(12):932–940, 2005.

[9] Donna Strickland and Gerard Mourou. Compression of amplified chirped optical pulses. *Optics communications*, 56(3):219–221, 1985.

[10] Todd Ditmire, J Zweiback, VP Yanovsky, TE Cowan, G Hays, and KB Wharton. Nuclear fusion from explosions of femtosecond laser-heated deuterium clusters. *Nature*, 398(6727):489–492, 1999.

[11] SS Bulanov, VD Mur, NB Narozhny, J Nees, and VS Popov. Multiple colliding electromagnetic pulses: a way to lower the threshold of e+ e- pair production from vacuum. *Physical review letters*, 104(22):220404, 2010.

[12] A McPherson, G Gibson, H Jara, U Johann, Ting S Luk, IA McIntyre, Keith Boyer, and Charles K Rhodes. Studies of multiphoton production of vacuum-ultraviolet radiation in the rare gases. *JOSA B*, 4(4):595–601, 1987.

[13] M Ferray, Anne L'Huillier, XF Li, LA Lompre, G Mainfray, and C Manus. Multiple-harmonic conversion of 1064 nm radiation in rare gases. *Journal of Physics B: Atomic, Molecular and Optical Physics*, 21(3):L31, 1988.

[14] XF Li, A L'Huillier, M Ferray, LA Lompré, and G Mainfray. Multiple-harmonic generation in rare gases at high laser intensity. *Physical Review A*, 39(11):5751, 1989.

[15] LV Keldysh et al. Ionization in the field of a strong electromagnetic wave. *Sov. Phys. JETP*, 20(5):1307–1314, 1965.

[16] Paul B Corkum. Plasma perspective on strong field multiphoton ionization. *Physical review letters*, 71(13):1994, 1993.

[17] Maciej Lewenstein, Ph Balcou, M Yu Ivanov, Anne L'huillier, and Paul B Corkum. Theory of high-harmonic generation by low-frequency laser fields. *Physical Review A*, 49(3):2117, 1994.

[18] Thomas Gaumnitz, Arohi Jain, Yoann Pertot, Martin Huppert, Inga Jordan, Fernando Ardana-Lamas, and Hans Jakob Wörner. Streaking of 43-attosecond soft-x-ray pulses generated by a passively cep-stable mid-infrared driver. *Optics express*, 25(22):27506–27518, 2017.

[19] Tenio Popmintchev, Ming-Chang Chen, Dimitar Popmintchev, Paul Arpin, Susannah Brown, Skirmantas Ališauskas, Giedrius Andriukaitis, Tadas Balčiunas, Oliver D Mücke, Audrius Pugzlys, et al. Bright coherent ultrahigh harmonics in the kev x-ray regime from mid-infrared femtosecond lasers. *science*, 336(6086):1287–1291, 2012.

[20] Olga Smirnova, Yann Mairesse, Serguei Patchkovskii, Nirit Dudovich, David Villeneuve, Paul Corkum, and Misha Yu Ivanov. High harmonic interferometry of multi-electron dynamics in molecules. *Nature*, 460(7258):972–977, 2009.

[21] Adrian L Cavalieri, Norbert Müller, Th Uphues, Vladislav S Yakovlev, Andrius Baltuška, Balint Horvath, B Schmidt, L Blümel, R Holzwarth, Stefan Hendel, et al. Attosecond spectroscopy in condensed matter. *Nature*, 449(7165):1029–1032, 2007.

[22] Francesca Calegari, D Ayuso, Andrea Trabattoni, Louise Belshaw, Simone De Camillis, S Anumula, F Frassetto, L Poletto, A Palacios, P Decleva, et al. Ultrafast electron dynamics in phenylalanine initiated by attosecond pulses. *Science*, 346(6207):336–339, 2014.

[23] Martin Schultze, Krupa Ramasesha, CD Pemmaraju, SA Sato, D Whitmore, A Gandman, James S Prell, LJ Borja, D Prendergast, K Yabana, et al. Attosecond band-gap dynamics in silicon. *Science*, 346(6215):1348–1352, 2014.

[24] Matteo Lucchini, Shunsuke A Sato, André Ludwig, Jens Herrmann, Mikhail Volkov, Lamia Kasmi, Yasushi Shinohara, Kazuhiro Yabana, Lukas Gallmann, and Ursula Keller. Attosecond dynamical franz-keldysh effect in polycrystalline diamond. *Science*, 353(6302):916–919, 2016.

[25] KS Budil, P Salières, Anne L'Huillier, T Ditmire, and MD Perry. Influence of ellipticity on harmonic generation. *Physical Review A*, 48(5):R3437, 1993.

[26] NH Burnett, C Kan, and PB Corkum. Ellipticity and polarization effects in harmonic generation in ionizing neon. *Physical Review A*, 51(5):R3418, 1995.

[27] W Becker, A Lohr, M Kleber, and M Lewenstein. A unified theory of high-harmonic generation: Application to polarization properties of the harmonics. *Physical Review A*, 56(1):645, 1997.

[28] Philippe Antoine, Bertrand Carré, Anne L'Huillier, and Maciej Lewenstein. Polarization of high-order harmonics. *Physical Review A*, 55(2):1314, 1997.

[29] H Eichmann, A Egbert, S Nolte, C Momma, B Wellegehausen, W Becker, S Long, and JK McIver. Polarization-dependent high-order two-color mixing. *Physical Review A*, 51(5):R3414, 1995.

[30] Avner Fleischer, Ofer Kfir, Tzvi Diskin, Pavel Sidorenko, and Oren Cohen. Spin angular momentum and tunable polarization in high-harmonic generation. *Nature Photonics*, 8(7):543–549, 2014.

[31] Ofer Kfir, Patrik Grychtol, Emrah Turgut, Ronny Knut, Dmitriy Zusin, Dimitar Popmintchev, Tenio Popmintchev, Hans Nembach, Justin M Shaw, Avner Fleischer, et al. Generation of bright phase-matched circularly-polarized extreme ultraviolet high harmonics. *Nature Photonics*, 9(2):99–105, 2015.

[32] Daniel D. Hickstein, Franklin J. Dollar, Patrik Grychtol, Jennifer L. Ellis, Ronny Knut, Carlos Hernández-García, Dmitriy Zusin, Christian Gentry, Justin M. Shaw, Tingting Fan, Kevin M. Dorney, Andreas Becker, Agnieszka Jaroń-Becker, Henry C. Kapteyn, Margaret M. Murnane, and Charles G. Durfee. Non-collinear generation of angularly isolated circularly polarized high harmonics. *Nature Photonics*, 9(11):743–750, 2015.

[33] Doron Azoury, Omer Kneller, Michael Krüger, Barry D. Bruner, Oren Cohen, Yann Mairesse, and Nirit Dudovich. Interferometric attosecond lock-in measurement of extreme-ultraviolet circular dichroism. *Nature Photonics*, 13(3):198–204, mar 2019.

[34] A Ferré, C Handschin, M Dumergue, F Burgy, A Comby, D Descamps, B Fabre, GA Garcia, R Géneaux, L Merceron, et al. A table-top ultrashort light source in the extreme ultraviolet for circular dichroism experiments. *Nature Photonics*, 9(2):93–98, 2015.

[35] Xiaosong Zhu, Xi Liu, Pengfei Lan, Dian Wang, Qingbin Zhang, Wei Li, and Peixiang Lu. Anomalous circular dichroism in high harmonic generation of stereoisomers with two chiral centers. *Optics express*, 24(22):24824–24835, 2016.

[36] Ofer Kfir, Sergey Zayko, Christina Nolte, Murat Sivis, Marcel Möller, Birgit Hebler, Sri Sai Phani Kanth Arekapudi, Daniel Steil, Sascha Schäfer, Manfred Albrecht, et al. Nanoscale magnetic imaging using circularly polarized high-harmonic radiation. *Science advances*, 3(12):eaao4641, 2017.

[37] Tingting Fan, Patrik Grychtol, Ronny Knut, Carlos Hernández-García, Daniel D Hickstein, Dmitriy Zusin, Christian Gentry, Franklin J Dollar, Christopher A Mancuso, Craig W Hogle, et al. Bright circularly polarized soft x-ray high harmonics for x-ray magnetic circular dichroism. *Proceedings of the National Academy of Sciences*, 112(46):14206–14211, 2015.

[38] Shambhu Ghimire, Anthony D DiChiara, Emily Sistrunk, Pierre Agostini, Louis F DiMauro, and David A Reis. Observation of high-order harmonic generation in a bulk crystal. *Nature physics*, 7(2):138–141, 2011.

[39] Giulio Vampa, TJ Hammond, Nicolas Thiré, BE Schmidt, François Légaré, CR McDonald, Thomas Brabec, DD Klug, and PB Corkum. All-optical reconstruction of crystal band structure. *Physical review letters*, 115(19):193603, 2015.

[40] AA Lanin, EA Stepanov, AB Fedotov, and AM Zheltikov. Mapping the electron band structure by intraband high-harmonic generation in solids. *Optica*, 4(5):516–519, 2017.

[41] REF Silva, Á Jiménez-Galán, B Amorim, O Smirnova, and M Ivanov. Topological strong-field physics on sub-laser-cycle timescale. *Nature Photonics*, 13(12):849–854, 2019.

[42] Nicolas Tancogne-Dejean, Michael A Sentef, and Angel Rubio. Ultrafast modification of hubbard u in a strongly correlated material: ab initio high-harmonic generation in nio. *Physical review letters*, 121(9):097402, 2018.

[43] REF Silva, Igor V Blinov, Alexey N Rubtsov, O Smirnova, and M Ivanov. High-harmonic spectroscopy of ultrafast many-body dynamics in strongly correlated systems. *Nature Photonics*, 12(5):266–270, 2018.

[44] Yuanmu Yang, Jian Lu, Alejandro Manjavacas, Ting S Luk, Hanzhe Liu, Kyle Kelley, Jon-Paul Maria, Evan L Runnerstrom, Michael B Sinclair, Shambhu Ghimire, et al. High-harmonic generation from an epsilon-near-zero material. *Nature Physics*, 15(10):1022–1026, 2019.

[45] Y. S. You, D. A. Reis, and S. Ghimire. Anisotropic high-harmonic generation in bulk crystals. *Nature Physics*, 13(4):345–349, apr 2017.

[46] Naotaka Yoshikawa, Tomohiro Tamaya, and Koichiro Tanaka. High-harmonic generation in graphene enhanced by elliptically polarized light excitation. *Science*, 356(6339):736–738, 2017.

[47] Robert W Boyd. *Nonlinear optics*. Academic press, 2019.

[48] Bahaa EA Saleh and Malvin Carl Teich. *Fundamentals of photonics*. john Wiley & sons, 2019.

[49] Andrew Weiner. *Ultrafast optics*, volume 72. John Wiley & Sons, 2011.

[50] Franz X Kärtner. *Few-cycle laser pulse generation and its applications*, volume 95. Springer Science & Business Media, 2004.

[51] Carsten Winterfeldt, Christian Spielmann, and Gustav Gerber. Colloquium: Optimal control of high-harmonic generation. *Reviews of Modern Physics*, 80(1):117, 2008.

[52] Mazyar Sabbar, Henry Timmers, Yi-Jen Chen, Allison K Pymer, Zhi-Heng Loh, Scott G Sayres, Stefan Pabst, Robin Santra, and Stephen R Leone. State-resolved attosecond reversible and irreversible dynamics in strong optical fields. *Nature physics*, 13(5):472–478, 2017.

[53] Antoine Moulet, Julien B Bertrand, Till Klostermann, Alexander Guggenmos, Nicholas Karpowicz, and Eleftherios Goulielmakis. Soft x-ray excitonics. *Science*, 357(6356):1134–1138, 2017.

[54] Gregory J Stein, Phillip D Keathley, Peter Krogen, Houkun Liang, Jonathas P Siqueira, Chun-Lin Chang, Chien-Jen Lai, Kyung-Han Hong, Guillaume M Laurent, and Franz X Kärtner. Water-window soft x-ray high-harmonic generation up to the nitrogen k-edge driven by a khz, 2.1 μm opcpa source. *Journal of Physics B: Atomic, Molecular and Optical Physics*, 49(15):155601, 2016.

[55] Seth L Cousin, Nicola Di Palo, Bárbara Buades, Stephan M Teichmann, M Reduzzi, M Devetta, Anatoli Kheifets, G Sansone, and Jens Biegert. Attosecond streaking in the water window: A new regime of attosecond pulse characterization. *Physical Review X*, 7(4):041030, 2017.

[56] J Tate, T Auguste, HG Muller, P Salières, P Agostini, and LF DiMauro. Scaling of wave-packet dynamics in an intense midinfrared field. *Physical Review Letters*, 98(1):013901, 2007.

[57] AD Shiner, C Trallero-Herrero, N Kajumba, H-C Bandulet, D Comtois, François Légaré, M Giguère, JC Kieffer, PB Corkum, and DM Villeneuve. Wavelength scaling of high harmonic generation efficiency. *Physical Review Letters*, 103(7):073902, 2009.

[58] Giulio Maria Rossi, Roland E Mainz, Yudong Yang, Fabian Scheiba, Miguel A Silva-Toledo, Shih-Hsuan Chia, Phillip D Keathley, Shaobo Fang, Oliver D Mücke, Cristian Manzoni, et al. Sub-cycle millijoule-level parametric waveform synthesizer for attosecond science. *Nature Photonics*, pages 1–7, 2020.

[59] Jiro Itatani, Jérôme Levesque, Dirk Zeidler, Hiromichi Niikura, Henri Pépin, Jean-Claude Kieffer, Paul B Corkum, and David M Villeneuve. Tomographic imaging of molecular orbitals. *Nature*, 432(7019):867–871, 2004.

[60] Philippe Antoine, Anne L'Huillier, Maciej Lewenstein, Pascal Salières, and Bertrand Carré. Theory of high-order harmonic generation by an elliptically polarized laser field. *Physical Review A*, 53(3):1725, 1996.

[61] IJ Sola, E Mével, L Elouga, E Constant, V Strelkov, L Poletto, P Villoresi, Enrico Benedetti, J-P Caumes, Salvatore Stagira, et al. Controlling attosecond electron dynamics by phase-stabilized polarization gating. *Nature Physics*, 2(5):319–322, 2006.

[62] K Rabinovitch, LR Canfield, and RP Madden. A method for measuring polarization in the vacuum ultraviolet. *Applied Optics*, 4(8):1005–1010, 1965.

[63] VG Horton, ET Arakawa, RN Hamm, and MW Williams. A triple reflection polarizer for use in the vacuum ultraviolet. *Applied optics*, 8(3):667–670, 1969.

[64] FA Weihe, SK Dutta, G Korn, D Du, PH Bucksbaum, and PL Shkolnikov. Polarization of high-intensity high-harmonic generation. *Physical Review A*, 51(5):R3433, 1995.

[65] T Koide, T Shidara, M Yuri, N Kandaka, K Yamaguchi, and H Fukutani. Elliptical-polarization analyses of synchrotron radiation in the 5–80-ev region with a reflection polarimeter. *Nuclear Instruments and Methods in Physics Research Section A: Accelerators, Spectrometers, Detectors and Associated Equipment*, 308(3):635–644, 1991.

[66] VV Strelkov, AA Gonoskov, IA Gonoskov, and M Yu Ryabikin. Origin for ellipticity of high-order harmonics generated in atomic gases and the sublaser-cycle evolution of harmonic polarization. *Physical review letters*, 107(4):043902, 2011.

[67] VV Strelkov, MA Khokhlova, AA Gonoskov, IA Gonoskov, and M Yu Ryabikin. High-order harmonic generation by atoms in an elliptically polarized laser field: Harmonic polarization properties and laser threshold ellipticity. *Physical Review A*, 86(1):013404, 2012.

[68] Jérôme Levesque, Yann Mairesse, Nirit Dudovich, Henri Pépin, Jean-Claude Kieffer, PB Corkum, and DM Villeneuve. Polarization state of high-order harmonic emission from aligned molecules. *Physical review letters*, 99(24):243001, 2007.

[69] Xibin Zhou, Robynne Lock, Nick Wagner, Wen Li, Henry C Kapteyn, and Margaret M Murnane. Elliptically polarized high-order harmonic emission from molecules in linearly polarized laser fields. *Physical review letters*, 102(7):073902, 2009.

[70] Yann Mairesse, N Dudovich, J Levesque, M Yu Ivanov, Paul B Corkum, and DM Villeneuve. Electron wavepacket control with elliptically polarized laser light in high harmonic generation from aligned molecules. *New Journal of physics*, 10(2):025015, 2008.

[71] Raluca Cireasa, AE Boguslavskiy, B Pons, MCH Wong, D Descamps, S Petit, H Ruf, Nicolas Thiré, A Ferré, J Suarez, et al. Probing molecular chirality on a sub-femtosecond timescale. *Nature Physics*, 11(8):654–658, 2015.

[72] Evgeny Savelyev, Rebecca Boll, Cédric Bomme, Nora Schirmel, Harald Redlin, Benjamin Erk, Stefan Düsterer, Erland Müller, Hauke Höppner, Sven Toleikis, et al. Jitter-correction for ir/uv-xuv pump-probe experiments at the flash free-electron laser. *New Journal of Physics*, 19(4):043009, 2017.

[73] Heung-Sik Kang, Chang-Ki Min, Hoon Heo, Changbum Kim, Haeryong Yang, Gyujin Kim, Inhyuk Nam, Soung Youl Baek, Hyo-Jin Choi, Geonyeong Mun, et al. Hard x-ray free-electron laser with femtosecond-scale timing jitter. *Nature Photonics*, 11(11):708–713, 2017.

[74] Miltcho B Danailov, Filippo Bencivenga, Flavio Capotondi, Francesco Casolari, Paolo Cinquegrana, Alexander Demidovich, Erika Giangrisostomi, Maya P Kiskinova, Gabor Kurdi, Michele Manfredda, et al. Towards jitter-free pump-probe measurements at seeded free electron laser facilities. *Optics express*, 22(11):12869–12879, 2014.

[75] Praveen Kumar Maroju, Cesare Grazioli, Michele Di Fraia, Matteo Moioli, Dominik Ertel, Hamed Ahmadi, Oksana Plekan, Paola Finetti, Enrico Allaria, Luca Giannessi, et al. Attosecond pulse shaping using a seeded free-electron laser. *Nature*, pages 1–6, 2020.

[76] Fabrice Wilhelm. Magnetic materials probed with polarized x-ray spectroscopies, 2013.

[77] Andrei Kirilyuk, Alexey V Kimel, and Theo Rasing. Ultrafast optical manipulation of magnetic order. *Reviews of Modern Physics*, 82(3):2731, 2010.

[78] Boris Vodungbo, Anna Barszczak Sardinha, Julien Gautier, Guillaume Lambert, Constance Valentin, Magali Lozano, Grégory Iaquaniello, Franck Delmotte, Stéphane Sebban, Jan Lüning, et al. Polarization control of high order harmonics in the euv photon energy range. *Optics express*, 19(5):4346–4356, 2011.

[79] Dejan B Milošević, Wilhelm Becker, and Richard Kopold. Generation of circularly polarized high-order harmonics by two-color coplanar field mixing. *Physical Review A*, 61(6):063403, 2000.

[80] Lou Barreau, Kévin Veyrinas, Vincent Gruson, Sébastien J Weber, Thierry Auguste, Jean-François Hergott, Fabien Lepetit, Bertrand Carre, Jean-Christophe Houver, Danielle Dowek, et al. Evidence of depolarization and ellipticity of high harmonics driven by ultrashort bichromatic circularly polarized fields. *Nature communications*, 9(1):1–10, 2018.

[81] Pei-Chi Huang, Carlos Hernández-García, Jen-Ting Huang, Po-Yao Huang, Chih-Hsuan Lu, Laura Rego, Daniel D Hickstein, Jennifer L Ellis, Agnieszka Jaron-Becker, Andreas Becker, et al. Polarization control of isolated high-harmonic pulses. *Nature Photonics*, 12(6):349–354, 2018.

[82] FHM Faisal and JZ Kamiński. Floquet-bloch theory of high-harmonic generation in periodic structures. *Physical Review A*, 56(1):748, 1997.

[83] Ashish Kumar Gupta, Ofir E Alon, and Nimrod Moiseyev. Generation and control of high-order harmonics by the interaction of an infrared laser with a thin graphite layer. *Physical Review B*, 68(20):205101, 2003.

[84] D Golde, T Meier, and Stephan W Koch. High harmonics generated in semiconductor nanostructures by the coupled dynamics of optical inter-and intraband excitations. *Physical Review B*, 77(7):075330, 2008.

[85] Hanzhe Liu, Yilei Li, Yong Sing You, Shambhu Ghimire, Tony F Heinz, and David A Reis. High-harmonic generation from an atomically thin semiconductor. *Nature Physics*, 13(3):262–265, 2017.

[86] Georges Ndabashimiye, Shambhu Ghimire, Mengxi Wu, Dana A Browne, Kenneth J Schafer, Mette B Gaarde, and David A Reis. Solid-state harmonics beyond the atomic limit. *Nature*, 534(7608):520–523, 2016.

[87] Yong Sing You, Yanchun Yin, Yi Wu, Andrew Chew, Xiaoming Ren, Fengjiang Zhuang, Shima Gholam-Mirzaei, Michael Chini, Zenghu Chang, and Shambhu Ghimire. High-harmonic generation in amorphous solids. *Nature communications*, 8(1):1–5, 2017.

[88] Olaf Schubert, Matthias Hohenleutner, Fabian Langer, Benedikt Urbanek, C Lange, U Huttner, D Golde, T Meier, M Kira, Stephan W Koch, et al. Sub-cycle control of terahertz high-harmonic generation by dynamical bloch oscillations. *Nature Photonics*, 8(2):119–123, 2014.

[89] T. T. Luu, M. Garg, S. Yu. Kruchinin, A. Moulet, M. Th Hassan, and E. Goulielmakis. Extreme ultraviolet high-harmonic spectroscopy of solids. *Nature*, 521(7553):498–502, may 2015.

[90] Shambhu Ghimire and David A Reis. High-harmonic generation from solids. *Nature Physics*, 15(1):10–16, 2019.

[91] G Vampa, TJ Hammond, N Thiré, BE Schmidt, F Légaré, CR McDonald, T Brabec, and PB Corkum. Linking high harmonics from gases and solids. *Nature*, 522(7557):462–464, 2015.

[92] G Vampa, CR McDonald, G Orlando, DD Klug, PB Corkum, and T Brabec. Theoretical analysis of high-harmonic generation in solids. *Physical review letters*, 113(7):073901, 2014.

[93] Aleksandr A Lanin, Eugeny A Stepanov, Aleksandr V Mitrofanov, Dmitry A Sidorov-Biryukov, Andrei B Fedotov, and Aleksei M Zheltikov. High-order harmonic analysis of anisotropic petahertz photocurrents in solids. *Optics letters*, 44(8):1888–1891, 2019.

[94] HD Barber. Effective mass and intrinsic concentration in silicon. *Solid-State Electronics*, 10(11):1039–1051, 1967.

[95] Martin A Green. Intrinsic concentration, effective densities of states, and effective mass in silicon. *Journal of Applied Physics*, 67(6):2944–2954, 1990.

[96] G Vampa and T Brabec. Merge of high harmonic generation from gases and solids and its implications for attosecond science. *Journal of Physics B: Atomic, Molecular and Optical Physics*, 50(8):083001, 2017.

[97] Kenichi L. Ishikawa, Yasushi Shinohara, Takeshi Sato, and Tomohito Otobe. Strong-field electron dynamics in solids, 2020.

[98] Michael Korbman, S Yu Kruchinin, and Vladislav S Yakovlev. Quantum beats in the polarization response of a dielectric to intense few-cycle laser pulses. *New Journal of Physics*, 15(1):013006, 2013.

[99] Mengxi Wu, Dana A Browne, Kenneth J Schafer, and Mette B Gaarde. Multilevel perspective on high-order harmonic generation in solids. *Physical Review A*, 94(6):063403, 2016.

[100] Peter G Hawkins, Misha Yu Ivanov, and Vladislav S Yakovlev. Effect of multiple conduction bands on high-harmonic emission from dielectrics. *Physical Review A*, 91(1):013405, 2015.

[101] M Lindberg and Stephan W Koch. Effective bloch equations for semiconductors. *Physical Review B*, 38(5):3342, 1988.

[102] Mackillo Kira and Stephan W Koch. *Semiconductor quantum optics*. Cambridge University Press, 2011.

[103] T Otobe. First-principle description for the high-harmonic generation in a diamond by intense short laser pulse. *Journal of Applied Physics*, 111(9):093112, 2012.

[104] Nicolas Tancogne-Dejean, Oliver D Mücke, Franz X Kärtner, and Angel Rubio. Impact of the electronic band structure in high-harmonic generation spectra of solids. *Physical review letters*, 118(8):087403, 2017.

[105] Nicolas Tancogne-Dejean, Oliver D Mücke, Franz X Kärtner, and Angel Rubio. Ellipticity dependence of high-harmonic generation in solids originating from coupled intraband and interband dynamics. *Nature communications*, 8(1):1–10, 2017.

[106] Isabella Floss, Christoph Lemell, Georg Wachter, Valerie Smejkal, Shunsuke A Sato, Xiao-Min Tong, Kazuhiro Yabana, and Joachim Burgdörfer. Ab initio multiscale simulation of high-order harmonic generation in solids. *Physical Review A*, 97(1):011401, 2018.

[107] N.W. Ashcroft and N.D. Mermin. *Solid State Physics*. Cengage Learning, 2011.

[108] Felix Bloch. Über die quantenmechanik der elektronen in kristallgittern. *Zeitschrift für Physik*, 52(7-8):555–600, 1929.

[109] Clarence Zener. A theory of the electrical breakdown of solid dielectrics. *Proceedings of the Royal Society of London. Series A, Containing Papers of a Mathematical and Physical Character*, 145(855):523–529, 1934.

[110] A Leitenstorfer, S Hunsche, J Shah, MC Nuss, and WH Knox. Femtosecond charge transport in polar semiconductors. *Physical review letters*, 82(25):5140, 1999.

[111] Leo Esaki and Ray Tsu. Superlattice and negative differential conductivity in semiconductors. *IBM Journal of Research and Development*, 14(1):61–65, 1970.

[112] Karl Leo, Peter Haring Bolivar, Frank Brüggemann, Ralf Schwedler, and Klaus Köhler. Observation of bloch oscillations in a semiconductor superlattice. *Solid State Communications*, 84(10):943–946, 1992.

[113] Christian Waschke, Hartmut G Roskos, Ralf Schwedler, Karl Leo, Heinrich Kurz, and Klaus Köhler. Coherent submillimeter-wave emission from bloch oscillations in a semiconductor superlattice. *Physical review letters*, 70(21):3319, 1993.

[114] J Itatani, F Quéré, Gennady L Yudin, M Yu Ivanov, Ferenc Krausz, and Paul B Corkum. Attosecond streak camera. *Physical review letters*, 88(17):173903, 2002.

[115] Phillip Donald Keathley, Siddharth Bhardwaj, J Moses, G Laurent, and Franz X Kaertner. Volkov transform generalized projection algorithm for attosecond pulse characterization. *New Journal of Physics*, 18(7):073009, 2016.

[116] Manish Garg, Minjie Zhan, Tran Trung Luu, H Lakhotia, Till Klostermann, Alexander Guggenmos, and Eleftherios Goulielmakis. Multi-petahertz electronic metrology. *Nature*, 538(7625):359–363, 2016.

[117] M. S. Dresselhaus. Solid state physics lecture, `http://web.mit.edu/course/6/6.732/www/6.732-pt2.pdf`.

[118] B. C. Stuart, M. D. Feit, S. Herman, A. M. Rubenchik, B. W. Shore, and M. D. Perry. Nanosecond-to-femtosecond laser-induced breakdown in dielectrics. *Phys. Rev. B*, 53:1749–1761, Jan 1996.

[119] Lionel Sudrie, Arnaud Couairon, Michel Franco, Brigitte Lamouroux, Bernard Prade, Stellios Tzortzakis, and André Mysyrowicz. Femtosecond laser-induced damage and filamentary propagation in fused silica. *Physical Review Letters*, 89(18):186601, 2002.

[120] Arlee V Smith and Binh T Do. Bulk and surface laser damage of silica by picosecond and nanosecond pulses at 1064 nm. *Applied optics*, 47(26):4812–4832, 2008.

[121] A Rämer, O Osmani, and B Rethfeld. Laser damage in silicon: Energy absorption, relaxation, and transport. *Journal of Applied Physics*, 116(5):053508, 2014.

[122] Uwe Morgner, Franz X Kärtner, Seong-Ho Cho, Yanbei Chen, Hermann A Haus, James G Fujimoto, Erich P Ippen, V Scheuer, Gregor Angelow, and Theo Tschudi. Sub-two-cycle pulses from a kerr-lens mode-locked ti: sapphire laser. *Optics letters*, 24(6):411–413, 1999.

[123] Stefan Rausch, Thomas Binhammer, Anne Harth, Jungwon Kim, Richard Ell, Franz X Kärtner, and Uwe Morgner. Controlled waveforms on the single-cycle scale from a femtosecond oscillator. *Optics express*, 16(13):9739–9745, 2008.

[124] Seunghwoi Han, Hyunwoong Kim, Yong Woo Kim, Young-Jin Kim, Seungchul Kim, In-Yong Park, and Seung-Woo Kim. High-harmonic generation by field enhanced femtosecond pulses in metal-sapphire nanostructure. *Nature communications*, 7(1):1–7, 2016.

[125] Kevin F Lee, Xiaoyan Ding, TJ Hammond, ME Fermann, G Vampa, and PB Corkum. Harmonic generation in solids with direct fiber laser pumping. *Optics letters*, 42(6):1113–1116, 2017.

[126] G Vampa, BG Ghamsari, S Siadat Mousavi, TJ Hammond, A Olivieri, E Lisicka-Skrek, A Yu Naumov, DM Villeneuve, A Staudte, P Berini, et al. Plasmon-enhanced high-harmonic generation from silicon. *Nature Physics*, 13(7):659–662, 2017.

[127] Murat Sivis, Marco Taucer, Giulio Vampa, Kyle Johnston, André Staudte, Andrei Yu Naumov, DM Villeneuve, Claus Ropers, and PB Corkum. Tailored semiconductors for high-harmonic optoelectronics. *Science*, 357(6348):303–306, 2017.

[128] Jian Lu, Eric F Cunningham, Yong Sing You, David A Reis, and Shambhu Ghimire. Interferometry of dipole phase in high harmonics from solids. *Nature Photonics*, 13(2):96–100, 2019.

[129] P. Xia, C. Kim, F. Lu, T. Kanai, H. Akiyama, J. Itatani, and N. Ishii. Nonlinear propagation effects in high harmonic generation in reflection and transmission from gallium arsenide. *Optics Express*, 26(22):29393, oct 2018.

[130] G Vampa, YS You, H Liu, S Ghimire, and DA Reis. Observation of backward high-harmonic emission from solids. *Optics express*, 26(9):12210–12218, 2018.

[131] Adrian Wirth, M Th Hassan, Ivanka Grguraš, Justin Gagnon, Antoine Moulet, Tran Trung Luu, S Pabst, R Santra, ZA Alahmed, AM Azzeer, et al. Synthesized light transients. *Science*, 334(6053):195–200, 2011.

[132] Mengxi Wu, Shambhu Ghimire, David A Reis, Kenneth J Schafer, and Mette B Gaarde. High-harmonic generation from bloch electrons in solids. *Physical Review A*, 91(4):043839, 2015.

[133] Zhou Wang, Hyunwook Park, Yu Hang Lai, Junliang Xu, Cosmin I Blaga, Fengyuan Yang, Pierre Agostini, and Louis F DiMauro. The roles of photo-carrier doping and driving wavelength in high harmonic generation from a semiconductor. *Nature communications*, 8(1):1–7, 2017.

[134] Ayelet J Uzan, Hadas Soifer, Oren Pedatzur, Alex Clergerie, Sylvain Larroque, Barry D Bruner, Bernard Pons, Misha Ivanov, Olga Smirnova, and Nirit Dudovich. Spatial molecular interferometry via multidimensional high-harmonic spectroscopy. *Nature Photonics*, 14(3):188–194, 2020.

[135] Tran Trung Luu and Hans Jakob Wörner. Measurement of the berry curvature of solids using high-harmonic spectroscopy. *Nature communications*, 9(1):1–6, 2018.

[136] Dieter Bauer and Kenneth K Hansen. High-harmonic generation in solids with and without topological edge states. *Physical review letters*, 120(17):177401, 2018.

[137] Hiroki Mashiko, Katsuya Oguri, Tomohiko Yamaguchi, Akira Suda, and Hideki Gotoh. Petahertz optical drive with wide-bandgap semiconductor. *Nature physics*, 12(8):741–745, 2016.

[138] Martin Schultze, Elisabeth M Bothschafter, Annkatrin Sommer, Simon Holzner, Wolfgang Schweinberger, Markus Fiess, Michael Hofstetter, Reinhard Kienberger, Vadym Apalkov, Vladislav S Yakovlev, et al. Controlling dielectrics with the electric field of light. *Nature*, 493(7430):75–78, 2013.

[139] Annkatrin Sommer, EM Bothschafter, SA Sato, Clemens Jakubeit, Tobias Latka, Olga Razskazovskaya, Hanieh Fattahi, Michael Jobst, W Schweinberger, Vage Shirvanyan, et al. Attosecond nonlinear polarization and light–matter energy transfer in solids. *Nature*, 534(7605):86–90, 2016.

[140] Kyung Taec Kim, Chunmei Zhang, Andrew D Shiner, Bruno E Schmidt, François Légaré, DM Villeneuve, and PB Corkum. Petahertz optical oscilloscope. *Nature Photonics*, 7(12):958, 2013.

[141] H. J. Simon and N. Bloembergen. Second-harmonic light generation in crystals with natural optical activity. *Phys. Rev.*, 171:1104–1114, Jul 1968.

[142] W. K. Burns and N. Bloembergen. Third-harmonic generation in absorbing media of cubic or isotropic symmetry. *Phys. Rev. B*, 4:3437–3450, Nov 1971.

[143] Yong Sing You, Jian Lu, Eric F Cunningham, Christian Roedel, and Shambhu Ghimire. Crystal orientation-dependent polarization state of high-order harmonics. *Optics letters*, 44(3):530–533, 2019.

[144] T Tamaya, A Ishikawa, T Ogawa, and K Tanaka. Diabatic mechanisms of higher-order harmonic generation in solid-state materials under high-intensity electric fields. *Physical review letters*, 116(1):016601, 2016.

[145] Matthew J Allen, Vincent C Tung, and Richard B Kaner. Honeycomb carbon: a review of graphene. *Chemical reviews*, 110(1):132–145, 2010.

[146] Nicolai Klemke, G Di Sciacca, Y Yang, Giulio Maria Rossi, RE Mainz, N Tancogne-Dejean, A Rubio, FX Kärtner, and OD Mücke. Circularly polarized high-order harmonics from solids driven by single-color infrared pulses. *Talk presented at ATTO*, pages 2–7, 2017.

[147] Nariyuki Saito, Peiyu Xia, Faming Lu, Teruto Kanai, Jiro Itatani, and Nobuhisa Ishii. Observation of selection rules for circularly polarized fields in high-harmonic generation from a crystalline solid. *Optica*, 4(11):1333–1336, 2017.

[148] CL Tang and Herbert Rabin. Selection rules for circularly polarized waves in nonlinear optics. *Physical Review B*, 3(12):4025, 1971.

[149] Ofir E. Alon, Vitali Averbukh, and Nimrod Moiseyev. Selection rules for the high harmonic generation spectra. *Phys. Rev. Lett.*, 80:3743–3746, Apr 1998.

[150] Michael Victor Berry. Quantal phase factors accompanying adiabatic changes. *Proceedings of the Royal Society of London. A. Mathematical and Physical Sciences*, 392(1802):45–57, 1984.

[151] F Duncan M Haldane. Nobel lecture: Topological quantum matter. *Reviews of Modern Physics*, 89(4):040502, 2017.

[152] Ayelet Julie Uzan, Gal Orenstein, Álvaro Jiménez-Galán, Chris McDonald, Rui E.F. Silva, Barry D. Bruner, Nikolai D. Klimkin, Valerie Blanchet, Talya Arusi-Parpar, Michael Krüger, Alexey N. Rubtsov, Olga Smirnova, Misha Ivanov, Binghai Yan, Thomas Brabec, and Nirit Dudovich. Attosecond spectral singularities in solid-state high-harmonic generation. *Nature Photonics*, pages 1–5, 2020.

[153] G. M. Rossi. *Parametric Waveform Synthesis*. PhD thesis, University of Hamburg, 2019.

[154] R. E. Mainz. *Sub-Cycle Light Field Synthesizer for Attosecond Science*. PhD thesis, University of Hamburg, 2019.

[155] Giulio Maria Rossi, Lu Wang, Roland E Mainz, Hüseyin Çankaya, Franz X Kärtner, and Giovanni Cirmi. Cep dependence of signal and idler upon pump-seed synchronization in optical parametric amplifiers. *Optics letters*, 43(2):178–181, 2018.

[156] D. E. Aspnes and A. A. Studna. Dielectric functions and optical parameters of Si, Ge, GaP, GaAs, GaSb, InP, InAs, and InSb from 1.5 to 6.0 eV. *Physical Review B*, 27(2):985–1009, jan 1983.

[157] G. Vampa, Y. S. You, H. Liu, S. Ghimire, and D. A. Reis. Observation of backward high-harmonic emission from solids. *Optics Express*, 26(9):12210, apr 2018.

[158] J. Lu, E. F. Cunningham, Y. S. You, D. A. Reis, and S. Ghimire. Interferometry of dipole phase in high harmonics from solids. *Nature Photonics*, 13(2):96–100, feb 2019.

[159] Dennis H Goldstein. *Polarized light*. CRC press, 2017.

[160] Edward Collett. *Field Guide to Polarization*. SPIE, sep 2005.

[161] N. Klemke, N. Tancogne-Dejean, G. M. Rossi, Y. Yang, F. Scheiba, R. E. Mainz, G. Di Sciacca, A. Rubio, F. X. Kärtner, and O. D. Mücke. Polarization-state-resolved high-harmonic spectroscopy of solids. *Nature Communications*, 10(1):1319, 2019.

[162] Shicheng Jiang, Jigen Chen, Hui Wei, Chao Yu, Ruifeng Lu, and CD Lin. Role of the transition dipole amplitude and phase on the generation of odd and even high-order harmonics in crystals. *Physical review letters*, 120(25):253201, 2018.

[163] Yuanmu Yang, Jian Lu, Alejandro Manjavacas, Ting S Luk, Hanzhe Liu, Kyle Kelley, Jon-Paul Maria, Evan L Runnerstrom, Michael B Sinclair, Shambhu Ghimire, et al. High-harmonic generation from an epsilon-near-zero material. *Nature Physics*, 15(10):1022–1026, 2019.

[164] Song-Feng Zhao, Lu Liu, and Xiao-Xin Zhou. Multiphoton and tunneling ionization probability of atoms and molecules in an intense laser field. *Optics Communications*, 313:74–79, 2014.

[165] George Gabriel Stokes. On the composition and resolution of streams of polarized light from different sources. *Transactions of the Cambridge Philosophical Society*, 9:399, 1852.

[166] K Veyrinas, V Gruson, Sébastien J Weber, L Barreau, T Ruchon, J-F Hergott, J-C Houver, RR Lucchese, P Salières, and D Dowek. Molecular frame photoemission by a comb of elliptical high-order harmonics: a sensitive probe of both photodynamics and harmonic complete polarization state. *Faraday discussions*, 194:161–183, 2016.

[167] Beth Schaefer, Edward Collett, Robert Smyth, Daniel Barrett, and Beth Fraher. Measuring the stokes polarization parameters. *American Journal of Physics*, 75(2):163–168, 2007.

[168] Fabian Scheiba, Nicolai Klemke, Nicolas Tancogne-Dejean, Giulio M Rossi, Angel Rubio, Oliver D Mücke, and Franz X Kärtner. Time-domain vectorial field reconstruction of a circularly polarized harmonic from silicon using 2d spectral shearing interferometry. In *2019 Conference on Lasers and Electro-Optics (CLEO)*, pages 1–2. IEEE, 2019.

[169] Jonathan R Birge, Richard Ell, and Franz X Kärtner. Two-dimensional spectral shearing interferometry for few-cycle pulse characterization. *Optics letters*, 31(13):2063–2065, 2006.

[170] Jonathan R Birge, Helder M Crespo, and Franz X Kärtner. Theory and design of two-dimensional spectral shearing interferometry for few-cycle pulse measurement. *JOSA B*, 27(6):1165–1173, 2010.

[171] F. Scheiba. Ultrabroadband spectral phase measurements by two-dimensional spectral shearing interferometry (2dsi). Master's thesis, University of Hamburg, 2017.

[172] Óscar Zurrón-Cifuentes, Roberto Boyero-García, Carlos Hernández-García, Antonio Picón, and Luis Plaja. Optical anisotropy of non-perturbative high-order harmonic generation in gapless graphene. *Optics express*, 27(5):7776–7786, 2019.

[173] Shima Gholam-Mirzaei, John E Beetar, Alexis Chacón, and Michael Chini. High-harmonic generation in zno driven by self-compressed mid-infrared pulses. *JOSA B*, 35(4):A27–A31, 2018.

[174] Shima Gholam-Mirzaei, John Beetar, and Michael Chini. High harmonic generation in zno with a high-power mid-ir opa. *Applied Physics Letters*, 110(6):061101, 2017.

[175] Hadis Morkoç and Ümit Özgür. *Zinc oxide: fundamentals, materials and device technology*. John Wiley & Sons, 2008.

[176] Fabian Langer, Matthias Hohenleutner, U Huttner, Stephan W Koch, M Kira, and Rupert Huber. Symmetry-controlled temporal structure of high-harmonic carrier fields from a bulk crystal. *Nature photonics*, 11(4):227, 2017.

[177] Keisuke Kaneshima, Yasushi Shinohara, Kengo Takeuchi, Nobuhisa Ishii, Kotaro Imasaka, Tomohiro Kaji, Satoshi Ashihara, Kenichi L Ishikawa, and Jiro Itatani. Polarization-resolved study of high harmonics from bulk semiconductors. *Physical review letters*, 120(24):243903, 2018.

[178] Michael Glazer, Gerald Burns, and Alexander N Glazer. *Space groups for solid state scientists*. Elsevier, 2012.

[179] MW Feise and DS Citrin. Semiclassical theory of terahertz multiple-harmonic generation in semiconductor superlattices. *Applied physics letters*, 75(22):3536–3538, 1999.

[180] Peter G Hawkins and Misha Yu Ivanov. Role of subcycle transition dynamics in high-order-harmonic generation in periodic structures. *Physical Review A*, 87(6):063842, 2013.

[181] N. Klemke, O. D. Mücke, A. Rubio, F. X. Kärtner, and N. Tancogne-Dejean. Role of intraband dynamics in the generation of circularly polarized high harmonics from solids. *Phys. Rev. B*, 102:104308, Sep 2020.

[182] Di Xiao, Ming-Che Chang, and Qian Niu. Berry phase effects on electronic properties. *Reviews of Modern Physics*, 82(3):1959–2007, 2010.

[183] Oliver D. Mücke. Isolated high-order harmonics pulse from two-color-driven Bloch oscillations in bulk semiconductors. *Physical Review B*, 84(8):081202, 2011.

[184] Q. T. Vu, H. Haug, O. D. Mücke, T. Tritschler, M. Wegener, G. Khitrova, and H. M. Gibbs. Light-Induced Gaps in Semiconductor Band-to-Band Transitions. *Physical Review Letters*, 92(21):217403, may 2004.

[185] Todd D Krauss and Frank W Wise. Femtosecond measurement of nonlinear absorption and refraction in cds, znse, and zns. *Applied physics letters*, 65(14):1739–1741, 1994.

[186] Haoyu Huang. *Terahertz-induced ultrafast symmetry control in condensed matter*. PhD thesis, University of Hamburg, 2020.

[187] Chuang Li, Ding Wang, Liwei Song, Jun Liu, Peng Liu, Canhua Xu, Yuxin Leng, Ruxin Li, and Zhizhan Xu. Generation of carrier-envelope phase stabilized intense 1.5 cycle pulses at 1.75 μm. *Optics express*, 19(7):6783–6789, 2011.

[188] Joseph Ladislas Wiza. Microchannel plate detectors. *Nucl. Instrum. Methods*, 162(1-3):587–601, 1979.

[189] The center for x-ray optics. X-ray transmission data, `https://henke.lbl.gov/optical_constants/filter2.html`.

[190] Yong Sing You, Mengxi Wu, Yanchun Yin, Andrew Chew, Xiaoming Ren, Shima Gholam-Mirzaei, Dana A Browne, Michael Chini, Zenghu Chang, Kenneth J Schafer, et al. Laser waveform control of extreme ultraviolet high harmonics from solids. *Optics letters*, 42(9):1816–1819, 2017.

[191] AM Hofmeister, E Keppel, and AK Speck. Absorption and reflection infrared spectra of mgo and other diatomic compounds. *Monthly Notices of the Royal Astronomical Society*, 345(1):16–38, 2003.

[192] Robert Adair, LL Chase, and Stephen A Payne. Nonlinear refractive index of optical crystals. *Physical Review B*, 39(5):3337, 1989.

[193] RN Hamm, RA MacRae, and ET Arakawa. Polarization studies in the vacuum ultraviolet. *JOSA*, 55(11):1460–1463, 1965.

[194] G Rosenbaum, B Feuerbacher, R Pl Godwin, and M Skibowski. Measurement of the polarization of extreme ultraviolet synchrotron radiation with a reflecting polarimeter. *Applied Optics*, 7(10):1917–1919, 1968.

Eidesstattliche Erklärung / Declaration on oath

Hiermit versichere ich an Eides statt, die vorliegende Dissertationsschrift selbst verfasst und keine anderen als die angegebenen Hilfsmittel und Quellen benutzt zu haben. Die eingereichte schriftliche Fassung entspricht der auf dem elektronischen Speichermedium. Die Dissertation wurde in der vorgelegten oder einer ähnlichen Form nicht schon einmal in einem früheren Promotionsverfahren angenommen oder als ungenügend beurteilt.

Ort, Datum Unterschrift

Erklärung zur Veröffentlichung / Declaration on publication

Ich erkläre mein Einverständnis mit der Einstellung dieser Dissertation in den Bestand der Bibliothek.

Ort, Datum Unterschrift